Winter 12-30-2012

ONLINE NONINTRUSIVE CONDITION MONITORING AND FAULT DETECTION FOR WIND TURBINES

Xiang Gong
University of Nebraska-Lincoln, soargong@gmail.com

ONLINE NONINTRUSIVE CONDITION MONITORING AND FAULT DETECTION FOR WIND TURBINES

By

Xiang Gong

A DISSERTATION

Presented to the Faculty of

The Graduate College at the University of Nebraska

In Partial Fulfillment of Requirements

For the Degree of Doctor of Philosophy

Major: Interdepartmental Area of Engineering

(Electrical Engineering)

Under the Supervision of Professor Wei Qiao

Lincoln, Nebraska

August, 2012

ONLINE NONINTRUSIVE CONDITION MONITORING AND FAULT DETECTION FOR WIND TURBINES

Xiang Gong, Ph.D.

University of Nebraska, 2012

Advisor: Wei Qiao

The goal of this dissertation research is to develop online nonintrusive condition monitoring and fault detection methods for wind turbine generators (WTGs). The proposed methods use only the current measurements that have already been used by the control and protection systems of WTGs; no additional sensors or data acquisition devices are needed. Current-based condition monitoring and fault detection techniques have great economic benefits and the potential to be adopted by the wind energy industry. However, there are challenges in using current measurements for wind turbine condition monitoring and fault detection. First, it is a challenge to extract WTG fault signatures from nonstationary current measurements, due to variable-speed operating conditions of WTGs. Moreover, the useful information in current measurements for wind turbine condition monitoring and fault detection usually has a low signal to noise ratio, which makes the condition monitoring and fault detection difficult.

WTG faults can be classified into two categories: the faults with characteristic frequencies (i.e., Type 1 faults) and the faults without characteristic frequencies (i.e., type 2 faults). For type 1 faults, appropriate demodulation methods have been proposed to calculate the frequency and the amplitude of the current measurements. Two 1P-invariant power spectrum density (PSD) method have then been proposed to use appropriate

resampling algorithms to convert the variable characteristic frequencies of WTG faults in the frequency domain of the current demodulated signals to constant values, where 1P stands for the shaft rotating frequency of the WTG. An impulse detection method has then been designed to find out the excitations in the 1P-invariant PSD of the current demodulated signals, where the excitations at the characteristic frequencies of WTG faults are extracted as the fault signatures. Finally, a fault signature evaluator has been designed to evaluate the WTG condition for fault detection. For Type 2 faults, a wavelet filter-based method has been developed to generate the fault index, which is then evaluated by a statistical control method-based fault index evaluator for fault detection. The proposed methods have been validated by extensive computer simulations and experiments for small direct-drive WTGs.

Acknowledgement

First and foremost, I would like to express my gratitude and sincere thanks to my advisor, Professor Wei Qiao, for his guidance in all the technical and personal aspects of my doctoral study. Not only knowledge, I have also learned the way of doing research with his guidance and enlightenment.

I would also like to thank other members of my supervisory committee, Professors Jerry Hudgins, Cho W. S. To, and Michael Hoffman, for their valuable suggestions and comments on my dissertation research as well as their assistance throughout the process of my Ph.D. work.

In addition, I would like to express my gratefulness to my classmates and my friends in Lincoln. Their sincerity and generosity have support my doctoral work and made my life rich and colorful.

Finally, I am indebted to my parents Chengshun Gong and Shibao Li, my girlfriend and my family members. They give me additional motivation and determination on my doctoral study.

Contents

List of Acronyms

a	scaling parameter
A_a	amplitude of artificial data
a_e	power law exponent
A_f	amplitude of impulse
A_i	sub-signal
A_m	amplitude of fault-irrelevant component of artificial data
b	time shifting parameter
C	generator current signal
C_f	modulated current signal
C^n	high-order harmonics in current signal
C_r	rotor current signal of doubly-fed induction generator
C_s	stator current signal
C_t	criteria to stop the iteration in high-performance 1P-invariant power spectrum density method
C_w	wavelet decomposed current signal
CWT	continuous wavelet transform
D	damping coefficient
D_b	ball diameter
D_c	pitch diameter
DFIG	doubly-fed induction generator
D_i	fluctuation in wavelet transform
DWT	discrete wavelet transform
E_r	amplitude of voltage induced in rotor of DFIG
E_{r0}	amplitude of induced DFIG rotor voltage at locked-rotor conditions
E_s	amplitude of stator voltage induced in permanent-magnet synchronous generator
E_w	energy of C_w
f	general frequency

f_1	current fundamental frequency
F_a	sinusoidal artificial data
f_a	frequency of artificial data
F_b	force of wind flow affected on the bottom of wind turbine rotating plane
f_b	characteristic frequency of a bearing ball fault in vibration measurements
f_c	characteristic frequency of a bearing cage fault in vibration measurements
$f_{c.b}$	characteristic frequencies of a bearing ball fault in current measurements
$f_{c.c}$	characteristic frequencies of a bearing cage fault in current measurements
$f_{c,fault}$	characteristic frequency of a wind turbine fault in modulated current
$f_{c.i}$	characteristic frequencies of a bearing inner-race fault in current measurements
$f_{c.o}$	characteristic frequencies of a bearing outer-race fault in current measurements
f_f	current components due to frequency modulation
f_{fault}	shaft torque variation frequency due to fault
FFT	fast Fourier transform
f_i	characteristic frequency of a bearing inner-race fault in vibration measurements
f_o	characteristic frequency of a bearing outer-race fault in vibration measurements
f_r	wind turbine shaft rotating frequency
F_r	constant shaft rotating frequency
$f_{r,i}$	interpolation of f_r
$f_{r,up}$	up sampled shaft rotating frequency
$f_{r.v}$	amplitude of excitation in shaft rotating frequency due to fault

$f_{r.w}$	shaft rotating frequency component generated by variable wind power
f_{rotor}	frequency of DFIG rotor current
f_s	sampling frequency
f_{syn}	frequency of DFIG stator current
F_t	force of wind flow affected on the top of wind turbine rotating plane
F_{wind}	force of wind flow affected on wind turbine blades
g	narrow-band dominant noise components in current signal
H_f	harmonics and excitations of current signal due to fault
i	iteration number of interpolation process in high-performance 1P-invariant power spectrum density method
I_1	amplitude of current signal
I_{DC}	constant component of C_s^2
I_f	current components due to amplitude modulation
I^n	high-frequency components of C_s^2
I_r	amplitude of DFIG rotor current
$I_{r.v}$	amplitude of excitation in amplitude of current due to fault
$I_{r.w}$	amplitude of current generated by variable wind power
I_s	amplitude of PMSG stator current signal
I_w	index of incipient fault
J	total inertia constant of wind turbine
K	constant representing the structure of PMSG
L	base value of the down-sampling step size
L_w	order of the Coiflet wavelet
M	up-sampling ratio
m_R	equivalent imbalance mass
n	sample index
N	data length
N_B	number of bearing balls

$N_{Gaussian}$	Gaussian noise
N_s	support length of the Coiflet wavelet
p	number of pole pairs of generator
PLL	phase lock loop
PMSG	permanent-magnet synchronous generator
PSD	power spectrum density
P_W	energy of current demodulated signal in a moving window
P_x	energy of current demodulated signal at a point
R	locally normalized 1P-invariant PSD
R_f	median filtered locally normalized 1P-invariant PSD
r_R	distance between equivalent imbalance mass and center of shaft
s	slip of DFIG
s_a	current amplitude demodulated signal
$s_{a,down}$	down sampled current amplitude demodulated signal
$s_{a,i}$	interpolation of s_a
$s_{a,up}$	up sampled current amplitude demodulated signal
s_{down}	$s_{f,down}$ or $s_{a,down}$
s_f	current frequency demodulated signal
$s_{f,down}$	down sampled current frequency demodulated signal
$s_{f,i}$	interpolation of s_f
$s_{f,up}$	up sampled current frequency demodulated signal
s_{up}	$s_{f,up}$ or $s_{a,up}$
s_w	emulated current signal with Gaussian noise
t	time index
T	torque on wind turbine shaft
T_0	torque due to variable wind power
T_e	electric torque of a wind generator
$T_{e.0}$	electric torque induced by wind power
$T_{e.v}$	amplitude of electric torque induced by fault
T_i	threshold

$T_{s,i}$	sample interval
T_v	amplitude of shaft torque variation created by fault
$U(z)$	wind velocities at height z
$V_{i,m}$	scaling signal function
W_{CWT}	decomposed signal by using continuous wavelet transform
W_{DWT}	decomposed signal by using discrete wavelet transform
$W_{i,m}$	wavelet function
WTG	wind turbine generator
W_w	moving window
X_i	sample location
x_p	artificial PSD with impulse
$x_{p,h}$	artificial PSD
X_{PSD}	sampled 1P-invariant PSD
z/z_r	reference height
$\boldsymbol{Z_s}$	equivalent complex impedance
δ	impulse
θ	ball contact angle
θ_m	phase angle of fault-irrelevant component of artificial data
μ	mean
σ	standard deviation
ϕ	total flux in PMSG
φ_1	initial phase of current signal
φ_e	phase shift between torque variations in shaft and generator
φ_f	current components due to phase modulation
ψ	wavelet function
Ω_{down}	normalized frequency of s_{down}
ω_m	angular frequency of fault-irrelevant component of artificial data
ω_r	wind turbine angular shaft rotating speed
Ω_r	normalized frequency of shaft rotating frequency
$\omega_{r.0}$	constant component of angular shaft rotating speed

$\omega_{r.v}$	amplitude of excitation in angular shaft rotating speed due to fault
$\omega_{r.w}$	angular shaft rotating speed generated by variable wind power

List of Figures

List of Tables

Chapter 1 Introduction

The penetration of wind power has increased greatly over the last decade in the United States and across the world. During the first quarter of 2012, the U.S. wind industry installed 1,695 megawatts (MW) across 17 states. This brings cumulative U.S. wind power capacity installations to 48,611 MW by the end of March 2012. Moreover, there are currently over 8,900 MW under construction across 31 states plus Puerto Rico [1]. The U.S. Department of Energy has envisioned that wind energy will provide 20% of U.S. electricity need by 2030 [2]. The European Wind Energy Association's scenarios show that wind energy will meet 15.7% (230 GW) and 28.5% (400 GW) of European electricity demand by 2020 and 2030, respectively [3]. The report of National Development and Reform Commission of P. R. China foresees wind power capacity reaching 200 GW by 2020, 400 GW by 2030, and 1000 GW by 2050 [4].

As the number of wind turbine generators (WTGs) continues to grow, it becomes more and more challenging for engineers to do inspection and maintenance for WTGs. As many WTGs are situated on high towers, installed in remote rural areas, distributed over large geographic regions, exposed to harsh environment, and subject to relatively high failure rates [5], inspection and maintenance for the WTGs requires significant effort and cost. It was reported [6]-[8] that the maintenance costs for onshore and offshore wind turbines are in the order of 10-15% and 20-35%, respectively, of the total cost of the electricity generated. On average, each WTG was shut down for 52-237 hours per year due to failures [9] caused by manufacturing or installation errors, aging effects, harsh environment, variable loading conditions experienced by wind turbine components, etc.

Furthermore, additional cost and significant downtime may be caused, if WTGs are not maintained timely. For instance, the failure of a $1,500 bearing, if not repaired or replaced timely, could result in a $100,000 gearbox replacement, a $50,000 generator rewind, and $70,000 in expenses to replace other failed components [10]. For offshore WTGs, bad weather conditions, e.g., storms, high tides, etc., can prevent any repair actions for several weeks [11]. The downtime of WTGs in turn results in significant losses of electric energy production. To make wind energy competitive with traditional forms of energy resources for electricity generation, it is necessary to minimize the maintenance costs and improve the reliability of WTGs.

The maintenance methods for WTGs can be divided into three categories: corrective maintenance, preventive maintenance, and condition-based maintenance [12]. A comparison of the maintenance methods for WTGs is summarized in Table 1.1 [13]. To achieve condition-based maintenance, online condition monitoring and fault detection is required for WTGs using condition monitoring data. Maintenance service is expected to be applied right before a pending failure [14]. Online condition monitoring and fault detection is an effective means to not only increase the reliability, but also reduce the costs associated with operation and maintenance of WTGs.

Table 1.1: A Comparison of Maintenance Methods.

Method	Advantage	Disadvantage
Corrective maintenance	• Low maintenance costs during operation. • Components will be used for a maximum lifetime.	• High risk in consequential damages resulting in extensive downtime. • Maintenance scheduling is not possible. • Spare part logistics is complicated. • It is likely to have long delivery periods for parts. • High one-time maintenance cost.
Preventive maintenance	• Expected downtime is low. • Maintenance can be scheduled. • Spare part logistics is easy.	• Components will not be used for the maximum lifetime. • Maintenance costs are higher compared to corrective maintenance.
Condition-based maintenance	• Components will be used close to their full lifetime. • Expected downtime is low. • Maintenance activities can be scheduled. • Spare part logistics is easy given that a failure can be detected in an early stage.	• Reliable information about the remaining lifetime of the components is required. • Additional condition monitoring hardware and software are required. • The market for condition monitoring systems within wind power industry is not mature.

The goal of this dissertation research is to develop novel current-based methods for online nonintrusive condition monitoring and fault detection for WTGs. The proposed methods are based on advanced signal processing and statistical analysis techniques. The proposed methods use only the generator current measurements that have been used by

the control and protection systems of the WTGs; no additional sensors or data acquisition devices are needed. Current signals are reliable and easily accessible from the ground without intruding the WTGs that are situated on high towers and installed in remote areas. The proposed methods are anticipated to be able to detect major failures in WTG components, including bearings, blades, generators, and shaft systems. The proposed methods can be easily integrated into existing WTG control, protection and monitoring systems and can be implemented remotely from the WTGs being monitored. The proposed methods provide an alternative to vibration measurement-based condition monitoring and fault detection. This will reduce the cost and hardware complexity of wind turbine condition monitoring and fault detection systems. The proposed methods can also be combined with vibration measurement-based methods to improve the accuracy and reliability of wind turbine condition monitoring and fault detection systems. When there are problems with vibration measurements, the proposed methods will ensure proper condition monitoring and fault detection for the WTGs, including their sensing systems. In conclusion, the proposed methods offer an effective means to achieve condition-based smart maintenance for WTGs and have a great potential to be adopted by the wind energy industry due to their almost no-cost, nonintrusive features.

This chapter will review common WTG faults and condition monitoring and fault detection methods in terms of sensor measurements and signal processing technologies used.

1.1 WTG Faults

The main components of a WTG that need to be monitored are shown in Figure 1.1, including blades, rotor and shaft, gearbox, yaw system, and the electric generator. All

of these components are inevitably subject to failure during operation of the WTG. This section briefly reviews the faults in these main components of the WTG.

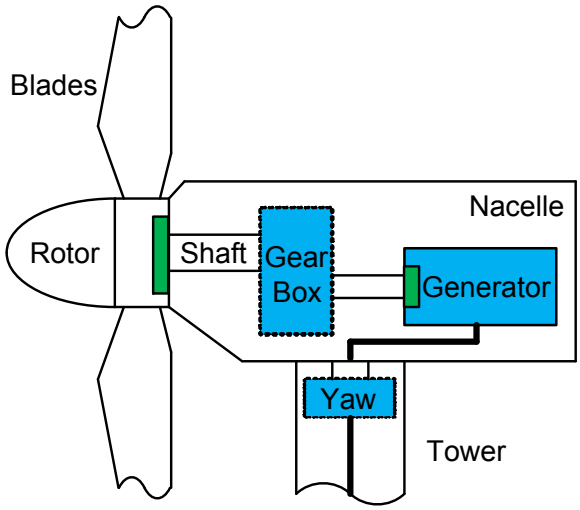

Figure 1.1: Main components of a WTG to be monitored.

1.1.1 Typical faults in wind turbine components

Blade imbalance and aerodynamic asymmetry are two major faults in WTG blades. Blade imbalance can be caused by errors in manufacturing and construction, icing, deformation due to aging, or wear and fatigue during the operation of WTGs [15]-[18]. Components tend to shift and wear in varying degrees over time, causing imbalance on the rotating blades. Aerodynamic asymmetry can be caused by several factors, including high wind shear and errors in the control mechanism [19]-[21]. If the pitch of one blade is slightly different from the other two blades due to errors in the control mechanism, the torque on the rotating shaft will not be balanced, leading to aerodynamic asymmetry.

Faults in the rotor and shaft of a WTG include shaft imbalance, impending cracks, shaft bearing faults, etc. The rotor and shaft of a WTG transmit variable mechanical energy generated from kinetic energy of wind to the electric generator and is always considered an important component for condition monitoring and fault detection of WTGs [17], [22], [23].

Faults of wind turbine gearboxes include tooth wear or breaks, eccentricity of tooth wheels, gearbox bearing faults, etc. [24], [25]. The gearbox has compact structure, fixed transmission ratio, great drive torque, complicated load, and changeable state in the running process [26]. It reports that gearboxes are considered highly critical for maintenance purpose [23].

The yaw system of a WTG controls how the tower turns, because as the wind direction turns the nacelle needs to adjust itself to face the wind properly [13]. A yaw system may be subject to yaw angle offset and wear or break of yaw gear tooth and has a high failure rate in WTGs [27]-[29].

Currently, most WTGs are equipped with a doubly-fed induction generator (DFIG) or a direct-drive permanent-magnet synchronous generator (PMSG). Faults in generators include generator rotor damage, bearing faults, stator turn faults, overheating, etc. Many technologies have been developed for condition monitoring and fault detection of electric machines based on current measurements [30]-[34]. Therefore, electric generator faults are not in the scope of this dissertation research.

Bearing faults constitute a significant portion of all faults in WTGs. As mentioned before, bearing faults may occur in rotors and shafts, gearboxes, or generators of WTGs.

The experience feedback from the wind energy industry corroborates that bearing failure is one of the typical failures in WTGs [10], [23]. According to different stages of the fault development process, bearing faults can be categorized into two types [35]: 1) single-point defect, which is defined as a single and localized defect on an otherwise relatively undamaged bearing surface; and 2) generalized roughness, which is a type of incipient fault where the condition of a bearing surface has degraded considerably over a large area and becomes rough, irregular, or deformed.

1.1.2 The failure frequency and downtime

The failure frequency and the associated downtime vary among main components of WTGs. To find the most critical components of a WTG, both the failure frequencies and the associated downtime of the WTG components should be considered [36]. Since wind turbine failure statistics are usually considered a trade secret of wind turbine manufacturers, there are few publications discussing failure frequencies and associated downtime of wind turbine components. The failure frequencies and associated downtime of wind turbine main components are summarized in Table 1.2 according to [5], [13], [27], [28], [36].

Table 1.2: Wind Turbine Failure Statistics.

Main components	Failure frequency distribution	Downtime distribution
Blade	5% - 13.4%	9.4%
Rotor and shaft	N/A	N/A
Gearbox	9.8% - 12%	19.4%
Yaw system	6.7% - 8%	13.3%
Generator	5% - 5.5%	8.9%

In Table 1.2, the faults in wind turbine main components at least contribute to 26.5% to 38.9% of the total faults and 41.9% of the total downtime of WTGs. Moreover, gearbox has the most high failure frequency and downtime among the wind turbine main components listed in Table 1.2. It should be mentioned that bearing faults are a typical type of faults in gearboxes [23], [37]. In WTGs, 40% of failures are related to bearings [38]. Therefore, bearing faults have significant contribution to the total faults and downtime of WTGs.

1.2 WTG Condition Monitoring and Fault Detection Methods

According to the sensor measurements used, most methods for condition monitoring and fault detection of WTGs can be classified into following categories: vibration monitoring, torque monitoring, temperature monitoring, oil/debris analysis, acoustic emission monitoring, optical fiber monitoring, and current/power monitoring.

The requirements of using these sensors and performance of these sensors are discussed in this section and summarized in Table 1.3.

1.2.1 Vibration monitoring

Most faults generated in the main components of WTGs cause vibrations of the WTGs. The blade or shaft imbalance of a WTG generates vibrations of the nacelle in the horizontal direction, due to a larger stiffness in the vertical direction and a smaller stiffness in the horizontal direction of the wind turbine tower [39], [40]. It has been reported that bolt loosing at the root of a blade would increase the vibration of the wind turbine nacelle [41]. A fault, e.g., surface pitting or tooth wear or break, in a gearbox may lead to the vibration of the gearbox [25], [42]. A bearing defect can generate a radial rotor movement and a shaft torque variation in the WTG, and consequently vibration of the wind turbine nacelle [43]-[47]. Therefore, commercial WTG condition monitoring and fault detection systems mostly employ vibration-based techniques, which are sophisticated, and the sensors and cabling are costly [48].

The vibration monitoring has been intensively studied in academia and widely used in industrial applications. The standards for vibration-based monitoring, ISO 10816, have been well accepted and provide guidance for evaluating vibration severity in electric machines operating in the 10 to 200 Hz (600 to 12,000 RPM) shaft rotating frequency range [49], [50]. However, one of the major disadvantages of vibration monitoring is high cost [51]. The second disadvantage is that vibration sensors are mounted on the surface of WTG components, which are situated on high towers and are difficult to access during WTG operation. Moreover, the sensors and equipment are inevitably subject to failure, which could cause additional problems with system reliability and additional operating

and maintenance costs. It has been reported that sensor failures contribute directly to more than 14% of failures in WTG systems, and more than 40% of WTG failures are related to the failure of sensors [5].

1.2.2 Torque monitoring

Torque oscillations can be detected in a blade or rotor imbalance condition of WTGs [20]. Torque monitoring has been utilized to detect the faults of a wind turbine's blades and rotors by measuring the torque on the shaft of the WTG [52]-[54]. Torque monitoring has also been applied to detect stator short-circuit faults in the generator of a WTG [55]. However, the complexity and cost of using torque monitoring is high. For instance, a torque transducer needs to be installed in the shaft in order to measure the torque of the wind turbine shaft, which increases the structure complexity of the WTG. Therefore, torque monitoring is rarely used in the wind industry.

1.2.3 Temperature monitoring

Bearing temperature should be in a certain range during wind turbine normal operating conditions. The IEEE standard 841 points out that the stabilized bearing temperature rises at the rated load should not exceed 45 °C [56]. Abrupt temperature increases while in the ordinary operating condition often means the failure of wind turbine bearings [22]. For example, the lack of lubrication will lead to abrupt increases in the bearing temperature. Similarly, the temperature of gearbox oil should be in a certain range during wind turbine rated operating conditions [57]. Therefore, temperature monitoring is able to disclose the health condition of wind turbine bearings and gearboxes. The major disadvantage of temperature monitoring is that the measured temperature is determined by multiple factors. Research shows that bearing temperature

depends on bearing fault, environment temperature, stator current heating, and generator rotating speed [58]. Therefore, further analysis is required to find the reason of abnormal temperature conditions in WTGs. Since a WTG normally works in rough conditions, the environment temperature changes frequently. It is complicated to simply use temperature monitoring for bearing and gearbox fault detection of WTGs.

1.2.4 Oil/debris analysis

Oil/debris analysis is currently one of the important means of condition monitoring in industry [59]. By analyzing the composition, content, size, and classification of wear particles in the lubrication oil of wind turbine components, their health conditions can be evaluated. In the wind industry, the oil/debris analysis data is one of the typical data for condition-based maintenance of WTGs [60]. However, the use of oil/debris analysis requires oil for lubrication and/or cooling of wind turbine bearings and gearboxes. Therefore, this method only works for high power rating WTGs with oil-lubricated bearings and gearboxes. For WTGs whose lubrication of bearings and gearboxes is sealed inside, oil/debris analysis methods are not practical [61].

1.2.5 Acoustic emission monitoring

Acoustic emission monitoring (from 1 kHz to 2 MHz) can provide a significant improvement over vibration monitoring, especially in the situation with high surrounding noise [62]. In the wind industry, acoustic emission monitoring is a typical method for condition-based maintenance of WTGs [60], [63]. For instance, when a low-speed rolling bearing is loaded and stress reaches the limit of the material strength, it will result in a slight gap of the failed bearing components to emit some stress to keep energy balance [64]. The stress wave generated by a broken bearing can be measured and applied to

detect the bearing fault of WTGs [65]. In [66], acoustic emission monitoring has been successfully applied to detect wind turbine bearing faults. The disadvantage of acoustic emission monitoring is its high cost. Since the frequency of acoustic emission signal is up to 100 MHz, sensors and data acquisition equipment are much more expensive than those used in other fault detection methods.

1.2.6 Optical fiber monitoring

Optical fiber monitoring can detect multiple physical parameters, e.g., temperature and strain of wind turbine components. Therefore, more and more attention is drawn to apply optical fiber monitoring in the wind industry. An optical fiber sensor system has been used to detect the structural states of wind turbine blades for condition-based maintenance [67]. To prevent consequential damages due to lightning on WTGs, the optical fiber monitoring has also been used for WTG lighting detection [68]. However, the optical fibers need to be mounted on the surface or embedded into the body of WTG components being monitored. Therefore, optical fiber monitoring is more complicated in real-world applications compared to other condition monitoring and fault detection methods.

1.2.7 Current/power monitoring

Current/power monitoring uses WTG current and/or voltage measurements that have been used by the control system of the WTG; no additional sensors or data acquisition equipment is needed. Moreover, current and/or voltage signals are reliable and easily accessible from the ground without intruding the WTGs. Therefore, current/power monitoring, as a nonintrusive monitoring method, has great economic benefits and potential to be adopted by the wind power industry. Some research has been

done on bearing fault detection of WTGs by using current measurements. For example, current measurements have been applied for bearing fault detection of DFIG and PMSG wind turbines [69]-[71]. Power measurements have also been used for bearing fault and generator fault detection of WTGs [72]. Ice accumulation on WTGs can be estimated by using d–q axis components of the WTG currents [73]. It has been reported that wind turbine blade faults can be successfully detected by using current measurements or power measurements [15], [74]. Moreover, current and power measurements have been used together for wind turbine rotor imbalance fault detection and gearbox failure detection [55], [75].

However, there are still challenges in using current and/or voltage signals for wind turbine condition monitoring and fault detection. First, the useful information in current and/or voltage signals has nonstationary statistics [18], due to the variable-speed operating condition of WTGs [76], [77]. It is a problem to extract WTG fault signatures from nonstationary current and/or voltage signals by using traditional spectrum analysis methods. Moreover, the dominant components of current and voltage signals are the fundamental-frequency component. Therefore, the useful information in current and voltage signals for wind turbine condition monitoring and fault detection usually has a low signal-to-noise ratio (SNR), which makes the condition monitoring and fault detection difficult.

Table 1.3: Summary of WTG Condition Monitoring and Fault Detection Methods

Monitoring methods	WTG components that can be monitored	Major disadvantages
Vibration monitoring	Blade, gearbox, bearing, generator	High cost, intrusive
Torque monitoring	Blade, shaft, generator	High cost, high complexity, intrusive
Temperature monitoring	Gearbox, bearing, generator	Multiple factors affect sensor outputs, intrusive
Oil/debris analysis	Gearbox, bearing	Only for oil cooled or lubricated components, intrusive
Acoustic emission monitoring	Bearing, blade, gearbox	High cost, intrusive
Optical fiber monitoring	Blade	High complexity, intrusive
Current/power monitoring	Blade, gearbox, bearing, shaft, generator	Low SNR

1.3 Current-Based Condition Monitoring and Fault Detection Techniques

As mentioned in Section 1.2.7, the current signals of WTGs are not acquired for condition monitoring and fault detection in the existing WTG systems. The useful information in current signals for wind turbine condition monitoring and fault detection usually has a low SNR. Therefore, it is much more difficult to use current signals than other signals, i.e. vibration signals, for wind turbine condition monitoring and fault

detection. Advanced signal processing and statistical analysis techniques need to be developed for online nonintrusive condition monitoring and fault detection of WTGs using generator current measurements. This section will summarize the current-based condition monitoring and fault detection system for WTGs proposed in this dissertation. The signal processing techniques, which have already been applied in wind turbine condition monitoring and fault detection systems, will be reviewed.

Several signal processing techniques, e.g., the classical power spectral density (PSD) analysis, wavelet analysis, demodulation methods, and Hilbert-Huang transform, are the candidates for current-based condition monitoring and fault detection of WTGs.

The PSD analysis is a classical method in the area of signal processing. The definition of this method can be found in many textbooks of signal processing. The PSD analysis has been widely used to find the excitations generated by fault components at the fault characteristic frequencies for condition monitoring and fault detection of WTGs,. In [17], [18], [20], [39], [41], [74], [78], the characteristic frequency of blade imbalance was found by using the PSD method based on current or vibration measurements. In [46], [79]-[82], the PSD method has been successfully applied to extract the characteristic frequencies of bearing faults for the generators of WTGs and electric machines based on current or vibration measurements. In 1995, it was firstly reported that the PSD method can be applied for bearing fault detection by using current signals of electric machines [43].

Wavelet analysis offers a powerful tool for feature extraction, data compression, and noise reduction in processing nonstationary signals [83]. Wavelet analysis has

already been applied for fault detection of WTGs and electric machines owing to its capability of frequency analysis for nonstationary signals. Rotor circuit imbalance fault of a WTG has been detected by using wavelet analysis during variable shaft rotating speed conditions [45]. That paper also mentioned that bearing faults of WTGs can also be detected by using the same method. It was reported in [84] that unbalanced stator windings of WTGs could be found by using a wavelet-based method. In [64], [85], [86], wavelet analysis has been applied for detection of broken rotor bars and bearing faults in electric machines. The gearbox faults of WTGs have also been analyzed by using the wavelet method [87]-[90]. It has been reported that both mechanical and electrical fault-like perturbations were successfully detected by using a continuous wavelet transform method for the wind turbines equipped with a DFIG and a PMSG [48], [91].

Demodulation methods, consisting of amplitude demodulation and frequency demodulation, can separate the useful information related to a WTG fault from the dominant components in the current signals to facilitate fault signature extraction. It has been proved that amplitude demodulation methods are able to discover bearing faults via stator current measurements for wind turbines equipped with DFIGs [70], [71], [92]. In other papers [93], [94], fundamental frequencies of stator currents were used for electric machine bearing fault detection. Fundamental frequencies are actually frequency demodulated signals of stator currents. The amplitude demodulation method based on Cepstrum and Hilbert transform has also been reported for fault detection of wind turbine gearboxes [95].

Hilbert-Huang transform can characterize both nonstationarity and nonlinearity of a signal [96], [97]. Recognition of the types of defects in gearboxes and blades of WTGs

has been developed by using Hilbert-Huang transform, which converts the measured current signals into time-frequency domain for analysis [98]. In [66], Hilbert-Huang transform was used to characterize the acoustic emission signals released from a wind turbine bearing. Demagnetization in PMSG has also been diagnosed by using Hilbert-Huang transform via current measurements [99].

The features of the aforementioned signal processing methods are listed in Table 1.4. The classical PSD analysis can identify WTG faults based on their characteristic frequencies in the measured signals. However, this capability is only available for stationary signals. As mentioned in Section 1.2.7, the measured current signals of WTGs are normally nonstationary. Therefore, the PSD analysis is able to be applied directly for condition monitoring and fault detection of WTGs. Wavelet analysis, demodulation methods, and Hilbert-Huang transform are able to extract WTG fault signatures from nonstationary signals. However, they cannot clearly identify WTG faults from interferences that have similar patterns as the faults in the time or frequency domain. Furthermore, these methods usually have low resolution and require high computational resources compared to the PSD analysis. Therefore, a computationally efficient, highly sensitive signal processing method is desired for current-based online condition monitoring and fault detection for WTGs operating in variable-speed conditions.

Table 1.4: Features of Signal Processing Methods.

Signal processing methods	Faulted components detected in WTGs	Major disadvantages
PSD analysis	Blade, bearing	Only for constant rotating speed WTGs
Wavelet analysis	Generator, gearbox	Low resolution in frequency domain
Demodulation methods	Bearing, gearbox	Low accuracy
Hilbert-Huang transform	Blade, bearing, gearbox	Require high computational resources

1.4 Current-based condition monitoring and fault detection of WTGs

Wind turbines equipped with DFIGs or PMSGs are used in most large wind power plants. Compared to fixed-speed WTGs, the use of DFIG wind turbines increases wind energy capture capability, reduces stresses of the mechanical structure, mitigates acoustic noise, and make the active and reactive power controllable for better grid integration [100], [101]. For PMSG wind turbines, less maintenance, higher efficiency, and better performance are the major advantages to make them a more attractive choice among different types of wind turbine systems [102], [103].

This dissertation research focuses on condition monitoring and fault detection of the mechanical components, including bearings, blades, and shafts, of the wind turbines equipped with DFIGs and PMSGs. The stator current signals of PMSGs and the rotor current signals of DFIGs, which are always used for controlling WTGs, are used for

condition monitoring and fault detection. The WTG faults considered in this research are classified into two types: Type 1 faults, which have specific characteristic frequencies in the frequency spectra of the current signals, and Type 2 faults, which are incipient faults without any characteristic frequency in the frequency spectra of the current signals. The schematic diagram of the proposed wind turbine online nonintrusive condition monitoring and fault detection system is shown in Figure 1.2. The current measurements are firstly processed such that the information of WTG faults can be easily extracted from these measurements. The signatures of bearing faults, blades imbalance, and shaft imbalance, etc., are then extracted from the fault information contained in the current measurements. Then, based on the results of fault signature extraction, the physical condition of wind turbine components is estimated. This information will be used to schedule maintenance for the WTG.

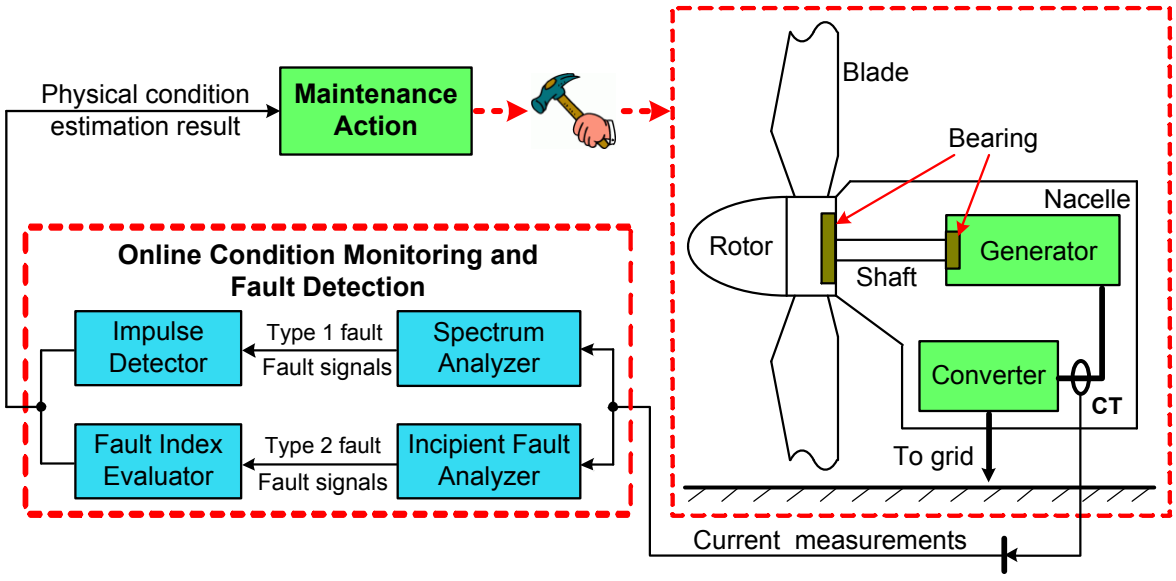

Figure 1.2: The proposed online nonintrusive condition monitoring and fault detection system for WTGs.

The dissertation is organized as following. Chapter 2 will analyze the frequency and amplitude modulation of current signals in WTG fault conditions, and introduce the corresponding demodulation methods to facilitate WTG fault detection. Chapter 3 will propose novel PSD methods of using nonstationary generator current signals for online condition monitoring and fault detection of WTGs operating in variable-speed conditions. Chapter 4 will propose a novel wavelet filter-based method for WTG incipient bearing fault detection using generator current measurements. Chapter 5 will propose an impulse detection method to detect WTG faults, which generate excitations at the fault characteristic frequencies in the 1P-invariant PSDs of the current demodulated signals, and introduce a statistical control method to design a fault index evaluator to detect the Type 2 WTG faults. In Chapter 6, simulation and experimental setups will be described to facilitate other researchers to verify the methods proposed in this dissertation research. Simulation and experimental results will be presented in Chapter 7 to verify the proposed methods for online nonintrusive condition monitoring and fault detection of WTGs.

Chapter 2 Current Signals in WTG Fault Conditions

In previous research, current signals have been used directly for fault detection of electric machines. The harmonics of current signals are analyzed and used for generator fault detections, including broken rotor bars, unbalanced voltages, stator winding faults, and eccentricity problems [104], [105]. In electric machines, the generalized roughness of bearings can be detected by using the increasing energy of current signals in high frequencies bands [35], [106]-[109].

A fault in a WTG may cause radial rotor movement and shaft torque variation of the WTG. These fault effects will modulate the amplitude and frequency of the generator current signals of the WTG. In has been reported that a bearing fault would generate stator current amplitude modulation in electric machines [43], [110]-[112]. According to [44], [113], a bearing fault of electric machines also leads to stator current frequency modulation. In a PMSG wind turbine, imbalance faults of the blades or rotor usually generates stator current frequency modulation [74]. The modulation of the current signal can be used for gearbox fault detection in electric machines and DFIG wind turbines [24], [95].

The current signal C of a healthy WTG can be modeled as follows:

$$C = I_1 \cdot \sin(2\pi \cdot f_1 \cdot t + \varphi_1) + C^n \tag{2.1}$$

where t is the time index in second; I_1, f_1 and φ_1 are the amplitude, frequency and phase of the fundamental component of the current signal, respectively; C^n represents the high

order harmonics in the current signal. The modulated current signal C_f of a faulted WTG can be modeled as:

$$C_f = (I_1 + I_f) \cdot \sin[2\pi \cdot (f_1 + f_f) \cdot t + (\varphi_1 + \varphi_f)] + C^n + H_f \tag{2.2}$$

where I_f, f_f and φ_f are the current components due to amplitude modulation, frequency modulation and phase modulation generated by WTG faults, respectively; H_f is the harmonics and other excitations of the current signal in WTG fault conditions. One of the major objectives of online nonintrusive WTG condition monitoring and fault detection is to detect I_f, f_f, φ_f and H_f, which are the signatures of the WTG fault in the current signal. This chapter will analyze the frequency and amplitude modulation of current signals in WTG fault conditions. The corresponding demodulation methods to facilitate fault detection will then be introduced.

2.1 Modulation of Wind Turbine Current Signals

In WTG fault conditions, current signals usually suffer amplitude modulation and frequency modulation generated by the effects of faults. The effects of faults include radial rotor movement and shaft torque variation of the WTGs. Radial rotor movement is the eccentricity of the wind turbine rotor generated by the fault. Shaft torque variation stands for the torque oscillation in the wind turbine shaft generated by the fault. The former has only been reported for bearing fault detection of WTGs. Furthermore, the effect of a radial rotor movement is negligible in some real applications of bearing fault detection [94]. This section will focus on the modulation of current signals by shaft torque variation generated by WTG faults.

2.1.1 Torque variation generated by WTG faults

As examples, the torque variations generated by WTG blade imbalance, aerodynamic asymmetry and bearing faults are discussed in this section. The blade imbalance fault stands for that the mass distribution of one blade is different from others. When a blade imbalance fault occurs on the shaft of a WTG, a torque variation will be induced in the shaft, which in turn will induce vibrations in the shaft rotating frequency f_r , which is named as 1P frequency, of the WTG and generate vibrations of the wind turbine nacelle. Figure 2.1 shows the effect generated by a blade imbalance fault, where m_R is the equivalent imbalance mass; r_R is the distance between the equivalent imbalance mass and the center of the shaft; and ω_r is the angular shaft rotating speed. When the equivalent imbalance mass rotates from the top to the bottom of the rotating plane, the power of gravity increases the torque on the shaft. On the other hand, when the equivalent imbalance mass rotates from the bottom to the top of the rotating plane, the power of gravity decreases the torque on the shaft. Consequently, the shaft torque vibrates at the frequency of 1P or f_r. Furthermore, the centrifugal force generated by the imbalance mass leads to vibration of the WTG at the frequency of f_r due to a larger stiffness in the vertical direction and a smaller stiffness in the horizontal direction of the WTG [39].

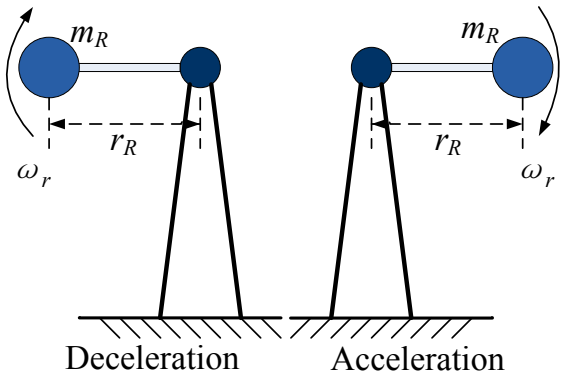

Figure 2.1: Effect of a blade imbalance fault.

Aerodynamic asymmetry occurs when the force affected on one blade is different from those on other blades. A fault in the pitch control system may introduce an aerodynamic asymmetry in the WTG. Aerodynamic asymmetry along with yaw error, wind shear, or tower shadow together influences the shaft torque of the WTG. For example, Figure 2.2 shows the effect of an aerodynamic asymmetry caused by wind shear, where F_{wind} is the force of the wind flow affected on the blades; F_t is the force of the wind flow affected on the blade that is on the top of the rotating plane; F_b is the force of the wind flow affected on the blade that is at the bottom of the rotating plane. The amplitude of F_t is always greater than that of F_b due to the effect of wind shear, which follows the following power law:

$$\frac{U(z)}{U(z_r)} = \left(\frac{z}{z_r}\right)^{\alpha_e} \tag{2.3}$$

where $U(z)$ and $U(z_r)$ are wind velocities at height z and the reference height z_r, respectively; and α_e is the power law exponent, which is approximately 1/7 [114]. Normally, a blade has the largest load caused by F_t and the smallest load caused by F_b.

Therefore, a vibration at the 3P frequency, which is the frequency of $3\times f_r$, is produced in the shaft torque by wind shear in a balanced wind turbine with three blades. In the case of an aerodynamic asymmetry, a blade of the WTG has different F_t and F_b from the other two blades. As a result, the acceleration and deceleration of the imbalanced blade produce a vibration at the 1P frequency in the shaft torque of the WTG. On the other hand, the other two blades have different F_t and F_b from the imbalanced one. As a result, a vibration also appears at the 2P frequency, which is the frequency of $2\times f_r$, in the shaft torque of the WTG.

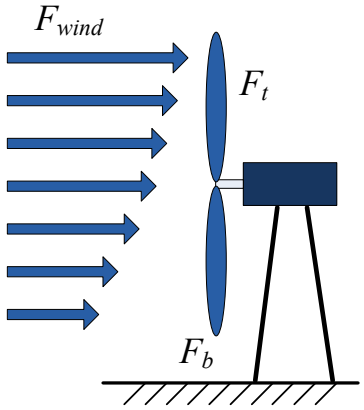

Figure 2.2: Effect of an aerodynamic asymmetry caused by wind shear.

A WTG bearing fault also modulates the current signal. The configuration of a ball bearing is shown in Figure 2.3, where D_b is the ball diameter; D_c is the pitch diameter; and θ is the ball contact angle, which is normally zero. If there is a fault in the outer race of the ball bearing, a torque variation will be generated due to the high friction at the fault point in the outer race compared to other parts of the outer race. Each time a ball passes through the fault, a mechanical resistance will appear when the ball tries to

leave the fault. The consequence is a small increase of the load torque at each contact between the fault and the bearing balls [44]. The characteristic frequencies of the torque variation generated by WTG bearing faults depend on the bearing geometry and the 1P frequency of the wind turbine. The theoretical characteristic frequencies of the typical four types of single-point bearing faults in vibration measurements are given below [115], [116]:

$$f_i = 0.5 \cdot N_B \cdot f_r \left(1 + \frac{D_b \cdot \cos\theta}{D_c} \right) \tag{2.4}$$

$$f_o = 0.5 \cdot N_B \cdot f_r \left(1 - \frac{D_b \cdot \cos\theta}{D_c} \right) \tag{2.5}$$

$$f_b = 0.5 \cdot f_r \cdot \left(\frac{D_c}{D_b} \right) \cdot \left[1 - \left(\frac{D_b \cdot \cos\theta}{D_c} \right)^2 \right] \tag{2.6}$$

$$f_c = 0.5 \cdot f_r \left(1 - \frac{D_b \cdot \cos\theta}{D_c} \right) \tag{2.7}$$

where f_i is the characteristic frequency of an inner-race fault; f_o is the characteristic frequency of an outer-race fault; f_b is the characteristic frequency of a ball fault; f_c is the characteristic frequency of a cage fault; f_r is the rotating frequency of the bearing; and N_B is the number of balls in the bearing.

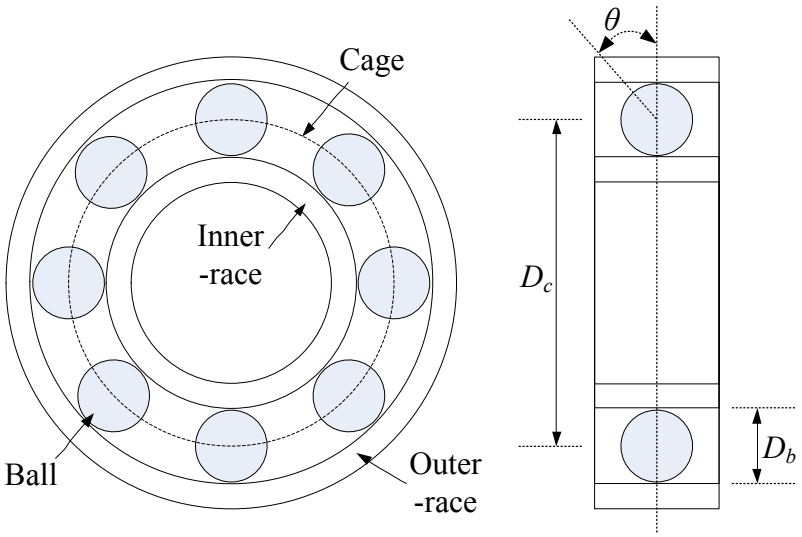

Figure 2.3: Configuration of a ball bearing.

2.1.2 Current modulation generated by torque variation

Suppose that a WTG fault leads to a shaft torque variation at the frequency of f_{fault}, where f_{fault} can be 1P, 2P, f_i, f_o, etc., depending on the types of the WTG faults. The WTG current signals are frequency and amplitude modulated by the shaft torque variation at the corresponding characteristic frequency f_{fault}, which is analyzed below.

The shaft torque of a faulted WTG can be modeled as follows:

$$T(t) = T_0(t) + T_v \cdot \cos(2\pi \cdot f_{fault} \cdot t) \tag{2.8}$$

where T is the torque on the wind turbine shaft; T_0 is the torque due to variable wind power; T_v is the amplitude of the shaft torque variation created by the WTG fault. The shaft torque variation has a characteristic frequency of f_{fault}, which is assumed to be constant in steady-state operation of the WTG, where the steady state stands for that the shaft speed varies slowly due to variable wind power.

If the shaft system of the WTG is simply represented by a one-mass model, the motion equation is given by [117]:

$$J\frac{d\omega_r(t)}{dt} = T(t) - T_e(t) - D\cdot\omega_r(t) \tag{2.9}$$

$$\omega_r(t) = 2\pi\cdot f_r(t) \tag{2.10}$$

where J is the total inertia constant of the WTG; ω_r is the angular shaft rotating speed of the WTG; $d\omega_r(t)/dt$ is the angular acceleration; T_e is the electric torque of the WTG; and D is the damping coefficient, which is approximately zero. If the WTG with the fault is operated at steady state, the electric torque T_e can be expressed by:

$$T_e(t) = T_{e.0}(t) + T_{e.v}\cdot\cos(2\pi\cdot f_{fault}\cdot t + \varphi_e) \tag{2.11}$$

where $T_{e.0}$ and $T_{e.v}\cdot\cos(2\pi\cdot f_{fault}\cdot t + \varphi_e)$ are the electric torques induced by T_0 and $T_v\cdot\cos(2\pi\cdot f_{fault}\cdot t)$, respectively; φ_e is the phase shift between the torque variations in the shaft and in the generator created by the WTG fault. Therefore, the angular shaft rotating speed is derived from (2.8), (2.9) and (2.11):

$$\frac{d\omega_r(t)}{dt} = \frac{T_0(t) - T_{e,0}(t)}{J} + \frac{T_f}{J}\cdot\cos(2\pi\cdot f_{fault}\cdot t + \varphi_f) \tag{2.12}$$

where

$$T_f\cdot\cos(2\pi\cdot f_{fault}\cdot t + \varphi_f) = T_v\cdot\cos(2\pi\cdot f_{fault}\cdot t) - T_{e.v}\cdot\cos(2\pi\cdot f_{fault}\cdot t + \varphi_e) \tag{2.13}$$

$$T_f = \{[T_v - T_{e.v}\cdot\cos(\varphi_e)]^2 + [T_{e.v}\cdot\sin(\varphi_e)]^2\}^{1/2} \tag{2.14}$$

$$\varphi_f = \arctan\left[\frac{-T_{e,v}\cdot\sin(\varphi_e)}{T_v - T_{e,v}\cdot\cos(\varphi_e)}\right] \tag{2.15}$$

The angular shaft rotating speed can then be calculated by integrating the right-hand side of (2.12), given by:

$$\omega_r(t) = \omega_{r.0} + \frac{1}{J} \cdot \int [T_0(t) - T_{e.0}(t)] \cdot dt + \frac{1}{J} \cdot \int T_f \cdot \cos(2\pi \cdot f_{fault} \cdot t + \varphi_f) \cdot dt \tag{2.16}$$

Equation (2.16) can be rewritten as:

$$\omega_r(t) = \omega_{r.0} + \omega_{r.w}(t) + \omega_{r.v} \cdot \sin(2\pi \cdot f_{fault} \cdot t + \varphi_f) \tag{2.17}$$

where $\omega_{r.0}$ is the constant component of the angular shaft rotating speed due to the integration operation; $\omega_{r.w}$ is the angular shaft rotating speed generated by the variable wind power; $\omega_{r.v}$ is the amplitude of the excitation in the angular shaft rotating speed due to the WTG fault. $\omega_{r.w}$ and $\omega_{r.v}$ are expressed as follows:

$$\omega_{r.w}(t) = \frac{1}{J} \cdot \int [T_0(t) - T_{e.0}(t)] \cdot dt \tag{2.18}$$

$$\omega_{r.v}(t) = \frac{T_f}{J \cdot 2\pi \cdot f_{fault}} \tag{2.19}$$

Using (2.10), the shaft rotating frequency of a WTG with a fault can be modeled as:

$$f_r(t) = f_{r.w}(t) + f_{r.v} \cdot \sin(2\pi \cdot f_{fault} \cdot t + \varphi_f) \tag{2.20}$$

where

$$f_{r,w} = \frac{\omega_{r,0} + \omega_{r,w}(t)}{2\pi} \tag{2.21}$$

$$f_{r,v} = \frac{\omega_{r,v}}{2\pi} \tag{2.22}$$

If the WTG system is equipped with a PMSG, the relationship between the shaft rotating frequency and the fundamental frequency f_1 of the stator current signal is given below:

$$f_1(t) = p \times f_r(t) \tag{2.23}$$

where p is the number of pole pairs of the PMSG. Using (2.20) and (2.23), the fundamental frequency of the stator current signal is:

$$f_1(t) = p \cdot f_{r.w}(t) + p \cdot f_{r.v} \cdot \sin(2\pi \cdot f_{fault} \cdot t + \varphi_f) \tag{2.24}$$

Therefore, the stator current signal C_s of the PMSG can be modeled as follows:

$$C_s(t) = I_s(t) \cdot \sin\{2\pi \int [p \cdot f_{r.w}(t) + p \cdot f_{r.v} \cdot \sin(2\pi \cdot f_{fault} \cdot t + \varphi_f)] \cdot dt\} \tag{2.25}$$

where the harmonics of the stator current C_s are not considered due to their low magnitudes compared to the fundamental-frequency component; I_s is the amplitude of the stator current signal. It shows that the stator current signal of a direct-drive PMSG wind turbine is frequency modulated by the shaft torque variation generated by the WTG fault.

The amplitude of the voltage E_s induced in a given stator phase of a PMSG is shown below [118]:

$$E_s(t) = K \cdot \phi \cdot f_1(t) \tag{2.26}$$

where K is a constant representing the structure of the PMSG; ϕ is the total flux in the PMSG. The amplitude of the phase current I_s is:

$$I_s(t) = \frac{E_s(t)}{|\boldsymbol{Z}_s(t)|} \tag{2.27}$$

where $\boldsymbol{Z_s}$ is the equivalent complex impedance of the generator stator circuit and the external circuit or load to which the PMSG is connected. According to (2.24), (2.26) and (2.27), the amplitude of the stator current signal I_s can be presented as:

$$I_s(t) = I_{s.w}(t) + I_{s.v}(t)\cdot\sin(2\pi\cdot f_{fault}\cdot t + \varphi_f) \tag{2.28}$$

$$I_{s,w}(t) = \frac{K\cdot\phi\cdot p\cdot f_{r,w}(t)}{|\boldsymbol{Z_s}(t)|} \tag{2.29}$$

$$I_{s,v}(t) = \frac{K\cdot\phi\cdot p\cdot f_{r,v}}{|\boldsymbol{Z_s}(t)|} \tag{2.30}$$

It shows that the stator current signal of the PMSG is amplitude modulated by the shaft torque variation created by the WTG fault.

If the WTG system is equipped with a DFIG, the relationship between the shaft rotating frequency and the electrical frequency f_{rotor} of the rotor current signal is given below:

$$f_{rotor}(t) = p\times f_r(t) - f_{syn} \tag{2.31}$$

where p is the number of pole pairs of the DFIG; f_{syn} is the frequency of the DFIG stator current, which is normally constant at 50 Hz or 60 Hz. Using (2.20) and (2.31), the electrical frequency of the rotor current signal is:

$$f_{rotor}(t) = p\cdot f_{r.w}(t) + p\cdot f_{r.v}\cdot\sin(2\pi\cdot f_{fault}\cdot t + \varphi_f) - f_{syn} \tag{2.32}$$

Therefore, the rotor current signal C_r of the DFIG can be modeled as follows:

$$C_r(t) = I_r(t)\cdot\sin\{2\pi\int[p\cdot f_{r.w}(t) + p\cdot f_{r.v}\cdot\sin(2\pi\cdot f_{fault}\cdot t + \varphi_f) - f_{syn}]\cdot dt\} \tag{2.33}$$

where I_r is the amplitude of the rotor current signal. It shows that the rotor current signal of a DFIG wind turbine is frequency modulated by the shaft torque variation generated by the WTG fault.

The amplitude of the induced rotor voltage E_r in a DFIG is [118]:

$$E_r(t) = -s \cdot E_{r0} \tag{2.34}$$

$$s = \frac{-f_{rotor}(t)}{f_{syn}} \tag{2.35}$$

where s is the slip of the DFIG; E_{r0} is the magnitude of the induced rotor voltage at locked-rotor conditions, which is a constant at a given stator voltage level. The amplitude of the DFIG rotor current I_r is:

$$I_r(t) = \frac{E_r(t)}{|\boldsymbol{Z}_r(t)|} \tag{2.36}$$

where $\boldsymbol{Z_r}$ is the equivalent complex impedance of the DFIG rotor circuit and the external circuit to which the DFIG rotor windings are connected. According to (2.31), (2.34), (2.35) and (2.36), the amplitude of the rotor current signal I_r can be presented as:

$$I_r(t) = I_{r,w}(t) + I_{r,v}(t) \cdot \sin(2\pi \cdot f_{fault} \cdot t + \varphi_f) \tag{2.37}$$

$$I_{r,w}(t) = \frac{E_{r0} \cdot [p \cdot f_{r,w}(t) - f_{syn}]}{|\boldsymbol{Z}_r(t)| \cdot f_{syn}} \tag{2.38}$$

$$I_{r,v}(t) = \frac{E_{r0} \cdot p \cdot f_{r,v}}{|\boldsymbol{Z}_r(t)| \cdot f_{syn}} \tag{2.39}$$

It shows that the rotor current signal of the DFIG is amplitude modulated by the shaft torque variation created by the WTG fault.

2.2 Demodulation Methods for Current Signal

As mentioned in Section 2.1, the torque variation generated by a WTG fault always modulates the frequency and amplitude of the WTG current signals. Therefore, appropriate demodulation methods which separate the useful information related to the WTG fault from the dominant components in the WTG current signals can facilitate the extraction of fault signatures from the current signals. Instead of using WTG current signals directly, the current demodulated signals are applied for online nonintrusive condition monitoring and fault detection.

According to (2.25), (2.29), (2.33) and (2.37), the stator current C_s of a PMSG and the rotor current C_r of a DFIG are expressed in (2.40) and (2.41), respectively:

$$C_s(t) = I_s(t) \cdot \sin[2\pi \int p \cdot f_r(t) \cdot dt] \tag{2.40}$$

$$C_r(t) = I_r(t) \cdot \sin\{2\pi \int [p \cdot f_r(t) - f_{syn}] \cdot dt\} \tag{2.41}$$

Therefore, both frequency and amplitude demodulation methods can be used to discover the excitations in $f_r(t)$, $I_s(t)$ and $I_r(t)$ created by the WTG fault.

2.2.1 Amplitude demodulation by using square law

The square law is a classical method for amplitude demodulation or envelope detection [119]. For online nonintrusive condition monitoring and fault detection of WTGs, the square law can be used to extract the variable amplitudes of the current signals. The analysis of using the square law for the fault modulated stator current signals is given below.

According to (2.28), the current signal of a WTG equipped with a PMSG in (2.40) can be rewritten as:

$$C_s(t) = [I_{s.w}(t) + I_{s.v}(t)\cdot\sin(2\pi\cdot f_{fault}\cdot t + \varphi_f)]\cdot\sin[\theta(t)] \tag{2.42}$$

where

$$\theta(t) = 2\pi\int p\cdot f_r(t)\cdot dt \tag{2.43}$$

Apply the square law to the signal C_s:

$$C_s(t)^2 = \{[I_{s.w}(t) + I_{s.v}(t)\cdot\sin(2\pi\cdot f_{fault}\cdot t + \varphi_f)]\cdot\sin[\theta(t)]\}^2 \tag{2.44}$$

Rewrite (2.44) by using trigonometric functions and sort the components form low frequency to high frequency:

$$C_s^{\,2}(t) = I_{DC} + I_{s,w}(t)\cdot I_{s,v}(t)\cdot\sin(2\pi\cdot f_{fault}\cdot t + \varphi_f) - \frac{1}{4}\cdot I_{s,v}^{\,2}(t)\cdot\cos(4\pi\cdot f_{fault}\cdot t + 2\varphi_f) + I^n \tag{2.45}$$

where I_{DC} is the constant component of C_s^2; I^n stands for the high-frequency components of C_s^2. The second component in (2.45) is an excitation due to the shaft torque variations created by the WTG fault. The third component in (2.45) is the second harmonic of the excitation generated by the shaft torque variations. Both terms can be easily separated from other components of C_s^2 that are not related to the WTG fault by using frequency spectrum analysis. Since the fundamental-frequency component is the dominant component in the stator current signals, the amplitude of $I_{s.w}(t)$ is much larger than that of $I_{s.v}(t)$. Therefore, the second harmonic of the excitation generated by the WTG fault usually has a lower magnitude than the second component in (2.45) and can be neglected.

2.2.2 Amplitude demodulation by using Hilbert transform

Considering measured current data $C(n)$, n = 1, 2, 3, … N, where N is the length of $C(n)$, the discrete Hilbert transform of $C(n)$ is given by [120]:

$$\mathcal{H}[C(n)] = \mathcal{F}^{-1}\{\mathcal{F}[C(n)]\cdot u(n)\} \tag{2.46}$$

where $\mathcal{F}()$ and $\mathcal{F}^{-1}()$ stand for the fast Fourier transform (FFT) and inverse FFT (IFFT), respectively; and $u(n)$ is defined as:

$$u(n) = \begin{cases} 1, & n = 0, N/2 \\ 2, & n = 1, 2, ..., N/2 - 1 \\ 0, & n = N/2 - 1, ..., N - 1 \end{cases} \tag{2.47}$$

The amplitude of $C(n)$, which is presented by $I_1(n)$, can be calculated by using the Hilbert transform of $C(n)$:

$$I_1(n) = \{C^2(n) + \{\mathcal{H}[C(n)]\}^2\}^{1/2} \tag{2.48}$$

It needs to be pointed out that Hilbert transform cannot be used to calculate the amplitude of an arbitrary time series. The $C(n)$ need to be an intrinsic mode function component, which is defined as any time series having the same number of zero-crossings and extrema, and also having symmetric envelopes defined by local maxima and minima, respectively [121]. Since the dominant component of the measured current data $C(n)$ is sinusoidal, $C(n)$ meets the requirement to be an intrinsic mode function component. Therefore, Hilbert transform can be used for amplitude demodulation of the measured current data $C(n)$ for condition monitoring and fault detection of the WTG.

Using the square law for amplitude demodulation of current signals requires low computational resources compared with using Hilbert transform. However the $C_s(t)^2$ in

(2.45) have the components I^n, which may interfere with the amplitude demodulation of the current signals. The Hilbert transform-based method leads to a better performance for amplitude demodulation.

2.2.3 Frequency demodulation by using phase lock loop

The frequency of the current signal of a WTG can be calculated by using the phase lock loop (PLL) method [122], which has been widely applied in control systems of electric machines. A PLL is designed in this research, as shown in Figure 2.4. Firstly, the Hilbert transform is used to calculate the instantaneous amplitude of the measured current data $C(n)$. The current measurement is then normalized by the calculated amplitude. The normalization eliminates the interference generated by the variable amplitude of the current signal. A modified mixer phase detector-based PLL is applied to calculate the stator current fundamental frequency f_1 of a PMSG or the rotor current electrical frequency f_{rotor} of a DFIG [123]. A proportional integral derivative (PID) module is employed as the lowpass filter in the proposed PLL. The fundamental frequency f_1 or electrical frequency f_{rotor} is the frequency demodulation signal of the measured current data $C(n)$.

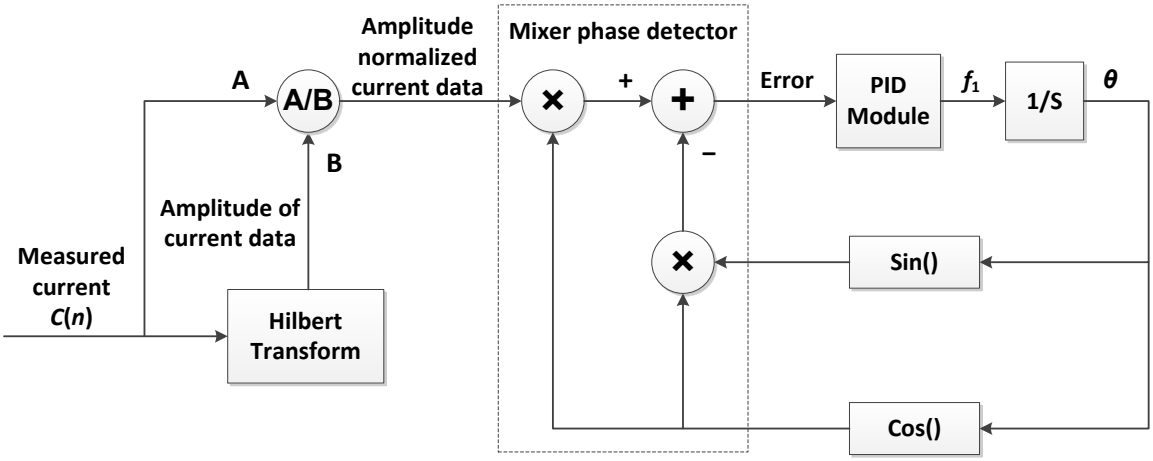

Figure 2.4: The proposed PLL method for signal frequency demodulation.

The PLL algorithm has already been embedded into microcontrollers and dedicated chips [122], [124]. Therefore, using the PLL method for frequency demodulation of WTG current signals does not require additional hardware or computational resource.

Chapter 3 1P-Invariant PSD Method

As mentioned in Chapter 1, the classical PSD analysis can identify WTG faults based on their characteristic frequencies in the frequency domain of processed signals. For instance, the characteristic frequency of a blade imbalance fault in the WTG shaft torque is the shaft rotating frequency f_r [18], [20], [74]; the characteristic frequencies of a bearing single-point fault in vibration measurements depend on the bearing geometry and rotating frequency, as listed in (2.4)-(2.7). The classical PSD analysis can be applied to detect these characteristic frequencies for WTG condition monitoring and fault detection. However, this capability is only available for stationary signals. This chapter proposes novel PSD methods of using nonstationary generator current signals for online condition monitoring and fault detection of WTGs operating in variable-speed conditions.

3.1 1P-Invariant PSD Method

Since the WTG fault characteristic frequencies vary with shaft rotating speed, which is variable when a WTG operates in variable-speed conditions [125], it is difficult to extract the fault signatures from the nonstationary current demodulated signals of the WTG by using classical spectrum analysis methods [18], [45], where the fault signatures are typically the excitations of the frequency spectra of the current demodulated signals at the fault characteristic frequencies. However, as mentioned in [18], [43], [44], if a WTG rotates at a constant speed, the classical PSD analysis could extract the signatures of WTG faults effectively. Therefore, if the WTG current demodulated signals are preprocessed in a way such that the variable shaft rotating frequency of the WTG is converted to a fixed value, the classical PSD analysis then can be used to detect the faults

of the WTG in variable-speed operating conditions. The proposed method, named 1P-invariant PSD method, is presented and verified by using artificial data in the following sections.

3.1.1 Proposed 1P-invariant PSD method

WTG current signal is the only required measurement in the proposed method. The current signal is firstly demodulated by using the methods presented in Section 2.2. Define Ω_r the normalized frequency of the WTG shaft rotating frequency or 1P frequency signal, which is calculated from the current measurements; and define f_s the sampling frequency of the current measurement. The relationship among f_r, f_s and Ω_r can be written as:

$$\frac{\Omega_r(t)}{2\pi} = \frac{f_r(t)}{f_s} \tag{3.1}$$

where $\Omega_r(t)$ is expected to be constant for the subsequent PSD analysis. Therefore, if the sampling frequency f_s is changed continuously with $f_r(t)$ to make the right-hand side of (3.1) constant by resampling the current demodulated signal, $\Omega_r(t)$ will become constant. Then classical PSD analysis can then be applied for the extraction of WTG fault signatures, in which the sampling frequency of the resampled current demodulated signals is treated as a constant value. Therefore, the shaft rotating frequency and the consequent WTG fault characteristic frequency are both constant values in the PSD of the resampled current demodulated signal. The proposed 1P-invariant PSD method is shown in Figure 3.1 and is implemented in the following steps.

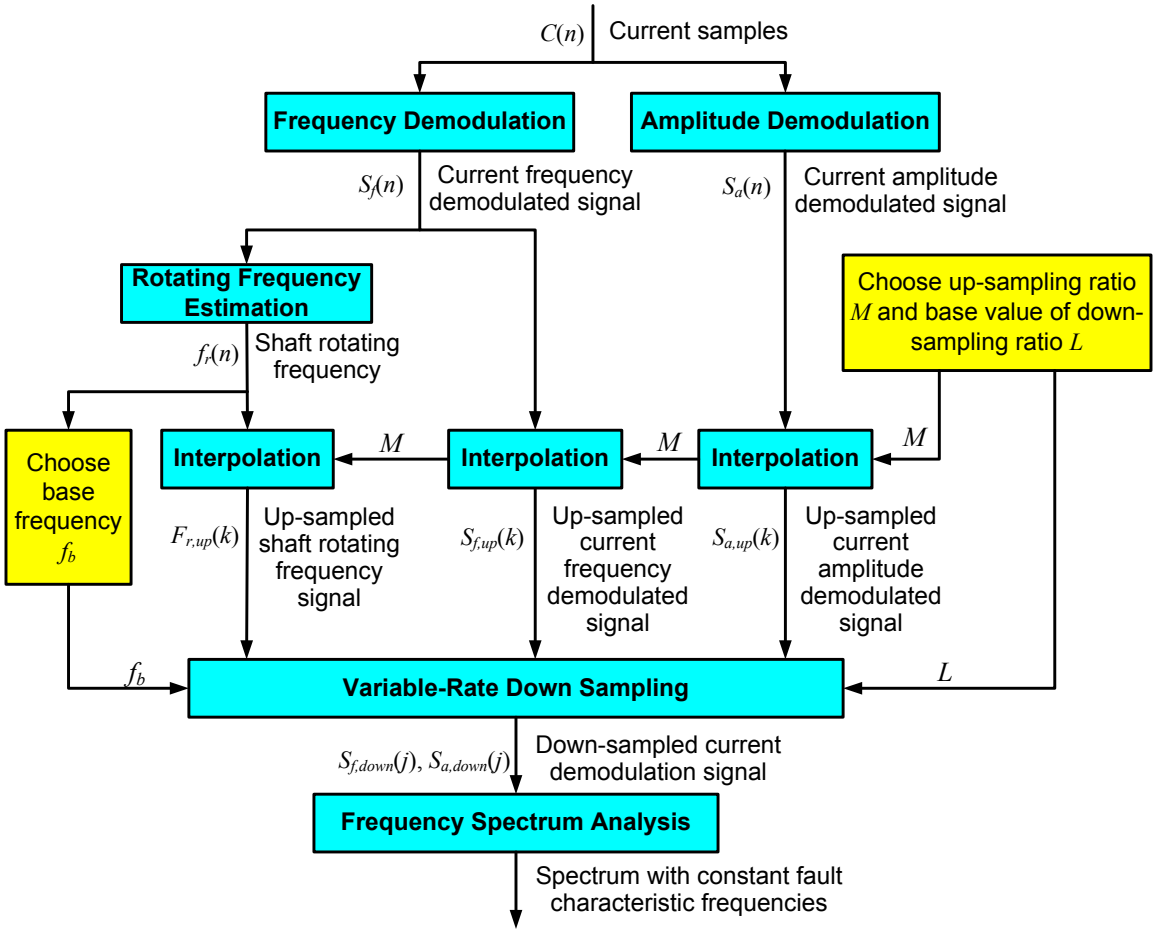

Figure 3.1: Schematic diagram of the 1P-invariant PSD method.

(1) Choose an up-sampling ratio M and a base value of the down-sampling step size L.

(2) Sample the measured nonstationary current of the WTG with a fixed sampling rate; the result is $C(n)$, where $n = 1, 2, 3, \ldots, N$ and N is the length of the current measurement.

(3) Demodulate the frequency and amplitude of the nonstationary current signal $C(n)$ by using PLL and Hilbert transform, respectively; the results are a current frequency demodulated signal $s_f(n)$ and a current amplitude demodulated signal $s_a(n)$.

(4) Estimate the shaft rotating frequency $f_r(n)$ by using the current frequency demodulated signal $s_f(n)$; and choose a base frequency f_b based on $f_r(n)$. For a PMSG, $f_r(n) = s_f(n)/p$; for a DFIG, $f_r(n) = [s_f(n) + f_{syn}]/p$.

(5) Interpolate (up-sample) f_r(n), $s_f(n)$ and $s_a(n)$ by a constant up-sampling ratio of M; the results are $f_{r,up}(k)$, $s_{f,up}(k)$ and $s_{a,up}(k)$, respectively, where $k = 1, 2, 3, \ldots, M \times N$.

(6) Down-sample $s_{f,up}(k)$ and $s_{a,up}(k)$ by a variable down-sampling step size; the results are $s_{f,down}(j)$ and $s_{a,down}(j)$, respectively, where $j = 1, 2, 3, \ldots, J$ and J is determined by M, N, and L. Suppose that $s_{down}(j)$ stands for $s_{f,down}(j)$ or $s_{a,down}(j)$; and $s_{up}(k)$ stands for $s_{f,up}(k)$ or $s_{a,up}(k)$. In the down-sampling process:

$$s_{down}(1) = s_{up}(1) \tag{3.2}$$

If $s_{down}(j) = s_{up}(k)$, then,

$$s_{down}(j+1) = s_{up}\left(k + R_{round}\left(\frac{L \cdot f_b}{f_{r,up}(k)}\right)\right) \tag{3.3}$$

where $R_{round}\left(\frac{L \cdot f_b}{f_{r,up}(k)}\right)$ is the variable down-sampling step size, which depends on the up-sampled shaft rotating frequency $f_{r,up}(k)$; and $R_{round}(\cdot)$ stands for rounding a number to the nearest integer. The down-sampling process to obtain $s_{down}(j)$ is equivalent to resampling the original or up-sampled current demodulated signal, $s(n)$ or $s_{up}(k)$, respectively, with a variable sampling frequency $f_s(k)$, whose value is proportional to the value of $f_{r,up}(k)$. According to (3.1), the normalized frequency of $s_{down}(j)$, which is $\Omega_{down}(j)$, is given by:

$$\frac{\Omega_{down}(j)}{2\pi} = \frac{s_{down}(j)}{f_s(j)} \tag{3.4}$$

where $\Omega_{down}(j)$ is now a constant value.

(7) Calculate the classical PSD of the down-sampled current demodulated signal $s_{down}(j)$ for the extraction of WTG fault signature.

By using the proposed method, the variable 1P frequency and consequently the variable characteristic frequency f_{fault} of a WTG fault becomes a constant value in the frequency spectrum of $s_{down}(j)$. Therefore, the resulting PSD spectrum is called the 1P-invariant PSD spectrum; and the amplitude of the excitation at f_{fault} in the PSD spectrum of $s_{down}(j)$ can be used as a signature to clearly identify and quantify the WTG fault. In the proposed method, the constant base value of the down-sampling step size, L, should be chosen based on two criteria. First, L should be large enough to eliminate the quantization error due to the requirement of an integral down-sampling step size. Second, L should be small enough to ensure that the sampling frequency after down sampling is greater than twice the f_{fault}. Normally, L should be larger than 10. The base frequency f_b is chosen to be the mean value of the estimated shaft rotating frequency $f_r(n)$. Furthermore, if the measured current is sampled with a sufficiently high sampling rate in Step (2) such that the sampling frequency of the down-sampled signal $s_{down}(j)$ without using up sampling is greater than twice the characteristic frequency of the WTG fault, then M is 1 and Step (5) is not necessary.

3.1.2 Verification of 1P-invariant PSD method

The proposed 1P-invariant PSD method is verified by using artificial sinusoidal data. The length of the artificial data is 10 seconds with a sampling frequency of 1 kHz. The artificial data is given by:

$$F_a(t) = A_a \cdot \sin(2\pi \cdot f_a \cdot t) \tag{3.5}$$

where A_a is the amplitude of artificial data and is equal to 1; f_a is the frequency of the artificial data, which increases from 0.1 Hz to 1 Hz linearly, as shown in Figure 3.2.

The artificial data are processed by using the proposed 1P-invariant PSD method, where the base value of the down-sampling step size L and up-sampling ratio of M are both 20, and f_b is set to be 0.5 Hz. The original artificial sinusoidal signal and its processed result by using the 1P-invariant PSD method are compared in Figure 3.3. By using the proposed method, the variable frequency of the artificial sinusoidal signal is converted to a constant value. The classical and 1P-invariant PSDs of the artificial sinusoidal signal are compared in Figure 3.4. The excitations of the artificial sinusoidal signal are in the range of 0.1 Hz to 1 Hz; the excitation of the 1P-invariant PSD method processed result appears only at 0.5 Hz, which is f_b. These results verify the viability of the proposed 1P-invariant PSD method for converting the variable frequency of a sinusoidal signal to a constant value.

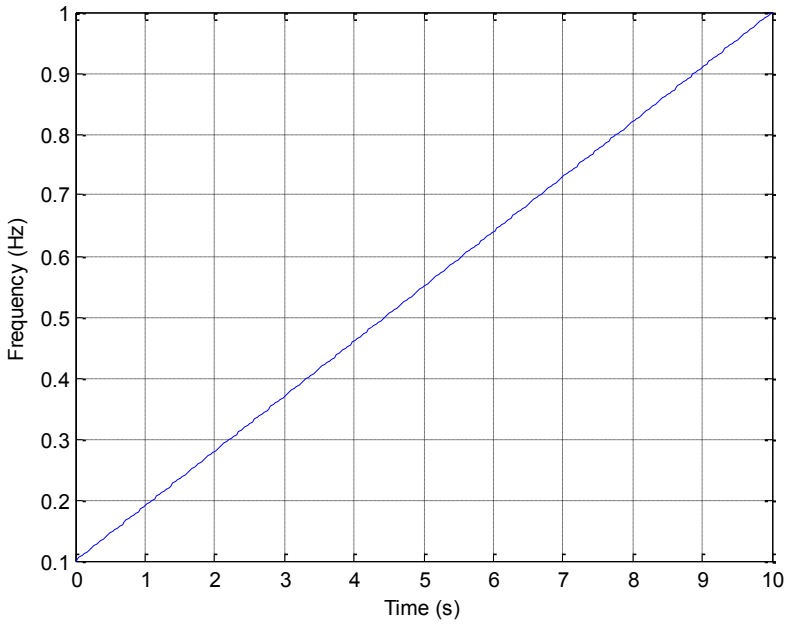

Figure 3.2: Frequency of the sinusoidal artificial data.

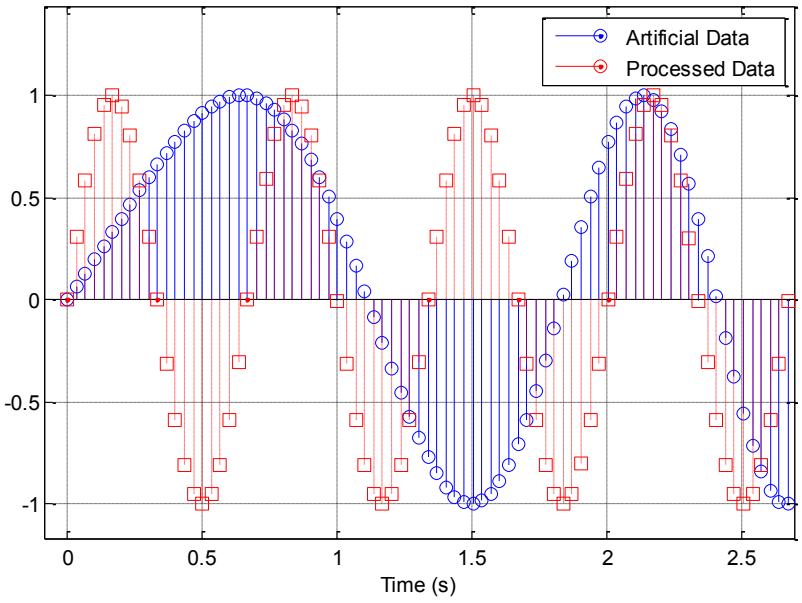

Figure 3.3: Comparison between the artificial sinusoidal signal and its processed result by using 1P-invarant PSD method.

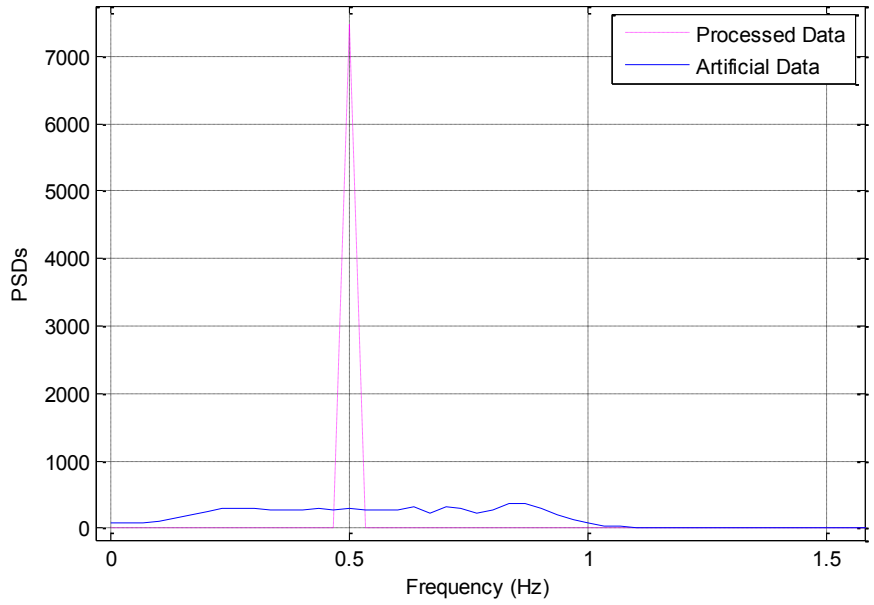

Figure 3.4: Classical and 1P-invariant PSDs of the artificial sinusoidal signal.

3.2 High-Performance 1P-Invariant PSD Method

The 1P-invariant PSD method proposed in Section 3.1 is a good approach to discover the excitations of WTG faults when the WTG operates in variable-speed operating conditions. However, the 1P-invariant PSD method requires significant memory space to store the up-sampled data, and has inevitable quantization error due to the requirement of an integral down-sampling step size. These limitations degrade the performance of the 1P-invariant PSD method, which may only be applicable to the low-frequency WTG fault detection due to limited computational resources of a WTG system. To improve the performance of the 1P-invariant PSD method, a high-performance 1P-invariant PSD method is proposed and verified in this section.

3.2.1 Proposed high-performance 1P-invariant PSD method

The objective of the high-performance 1P-invariant PSD method is also to convert the WTG shaft rotating frequency f_r, and consequently the WTG fault characteristic frequency, to a constant value in the PSD of the resampled current demodulated signal. The high-performance 1P-invariant PSD method is implemented in the following steps and shown in Figure 3.5.

(1) Sample the measured nonstationary current of the WTG with a fixed sampling rate; the result is $C(n)$, where n = 1, 2, 3, …, N and N is the length of the current measurement.

(2) Demodulate the frequency and amplitude of the nonstationary current signal $C(n)$; the results are a current frequency demodulated signal $s_f(n)$ and a current amplitude demodulated signal $s_a(n)$.

(3) Estimate the shaft rotating frequency $f_r(n)$ by using the current frequency demodulated signal $s_f(n)$. For a PMSG, $f_r(n) = s_f(n)/p$; for a DFIG, $f_r(n) = [s_f(n) + f_{syn}]/p$.

(4) Assume sampling interval of $f_r(n)$, $s_f(n)$, and $s_a(n)$ between consecutive samples is 1. The location $X_i(n)$ of the time series $f_{r,i}(n)$, $s_{f,i}(n)$, and $s_{a,i}(n)$ is calculated, where i = 0, 1, 2, …, is the iteration number in the interpolation process described in Steps (5) and (6); $X_0(n) = n$ and $f_{r,0}(n) = f_r(n)$ are the initial values of the interpolation process.

(5) Define $T_{r,i}(n) = \dfrac{1}{f_{r,i}(n) + f_{r,i}(n+1)}$, the objective locations of each sample of the time series $f_{r,i}(n)$, $s_{f,i}(n)$, and $s_{a,i}(n)$ in the interpolation are:

$$X_{i+1}(1) = 1 \tag{3.6}$$

$$X_{i+1}(N) = N \tag{3.7}$$

$$X_{i+1}(n+1) = X_{i+1}(n) + \frac{(N-1)\cdot T_{r,i}(n)}{\sum_{n=1}^{N-1} T_{r,i}(n)} \tag{3.8}$$

(6) The $f_r(n)$, $s_f(n)$ and $s_a(n)$ are interpolated [126] to get $f_{r,i}(n)$, $s_{f,i}(n)$ and $s_{a,i}(n)$, respectively, based on the objective locations $X_{i+1}(n)$ of the time series $f_{r,i}(n)$, $s_{f,i}(n)$, and $s_{a,i}(n)$ in Step (5).

(7) Repeat (4)-(6) until $c_r(i)$ in (3.9) is smaller than C_t, where C_t is chosen to be the criterion to stop the iteration.

$$c_t(i) = \sum_{n=1}^{N} \left| X_i(n) - X_{i+1}(n) \right| \tag{3.9}$$

(8) Calculate the classical PSD of the resampled current demodulated signal $s_{f,i}(n)$ and $s_{a,i}(n)$ for WTG fault signature extraction.

By using the proposed high-performance 1P-invariant PSD method, the variable characteristic frequency f_{fault} of a WTG fault becomes a constant value in the frequency spectra of $s_{f,i}(n)$ and $s_{a,i}(n)$. The amplitude of the excitation at f_{fault} is used as a signature to identify and quantify the appearance and degree of WTG faults, respectively.

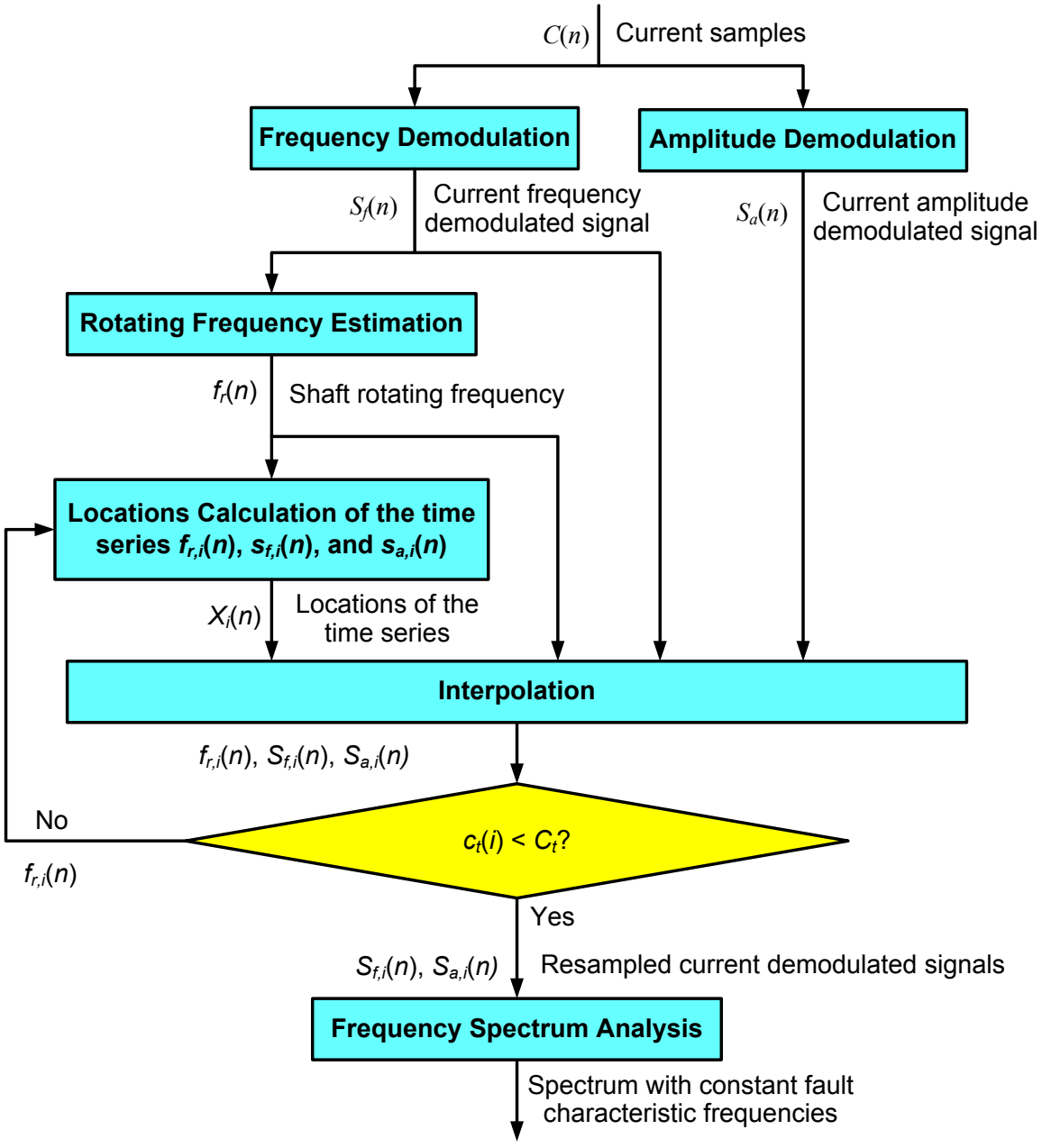

Figure 3.5: Schematic diagram of the high-performance 1P-invariant PSD method.

The proposed method requires little memory space to store the data. No quantization error is generated during the interpolation, as given in Step (6). Moreover, the sampling frequency of the resampled current demodulated signal is the same as that

of the original current signal. Therefore, the resulting PSD spectrum has higher performance than the previous 1P-invariant PSD spectrum described in section 3.1 in terms of frequency resolution. However, the cost is that more CPU time is needed by the high-performance 1P-invariant PSD method. Decreasing the value of criterion C_t in Step (7) leads higher performance of the proposed method to convert the variable characteristic frequency f_{fault} of a WTG fault to a constant value in the frequency spectra of the resamped current demodulated signals $s_{f,i}(n)$ and $s_{a,i}(n)$ but a longer calculation time. In real-world applications a tradeoff between performance and computational resource should be considered to determine the value of C_t.

An example of the proposed high-performance 1P-invariant PSD method is given in Figure 3.6, where $s_{f,i}(n)$ is the processed time series; N is 4; i = 0, 1. In the first iteration of the interpolation process (i.e., resampling), the sampling frequency $f_{s,1}$ needs to be proportional to the shaft rotating frequency $f_{r,0}$ to make the right-hand side of (3.1) constant, as given below:

$$f_{s,1}(n) \propto f_{r,0}(n) \tag{3.10}$$

The sampling interval $T_{s,1}$ between two consecutive samples is defined to be the reciprocal of the average sampling frequencies of the two samples:

$$T_{s,1}(n) = \frac{2}{f_{s,1}(n) + f_{s,1}(n+1)} \tag{3.11}$$

Based on (3.10) and (3.11), the relationship between $T_{s,1}$ and $f_{r,0}$ is given below to make the right-hand side of (3.1) constant:

$$T_{s,1}(n) \propto \frac{1}{f_{r,0}(n) + f_{r,0}(n+1)} = T_{r,0}(n) \tag{3.12}$$

Then the objective of a constant Ω_r can be achieved by the setting $T_{r,0}(n)$ in the interpolation process as follows, where $T_{r,0}(n)$ determines the objective locations of the samples of the processed time series $s_{f,i}(n)$ in the interpolation:

$$T_{s,1}(n) = \frac{3 \cdot T_{r,0}(n)}{\sum_{k=1}^{3} T_{r,0}(k)} \tag{3.13}$$

Equation (3.13) meets the proportional constraint of $T_{s,1}$ and $T_{r,0}$ given in (3.12).

In the proposed high-performance 1P-invariant PSD method, the sampling interval $T_{s,1}$ for the interpolation is based on the previous shaft rotating frequency signal $f_{r,0}$, as given in (3.8). However, shaft rotating frequency signal changes from $f_{r,0}$ to $f_{r,1}$ due to the interpolation. Normally we have:

$$T_{s,1}(n) = \frac{3 \cdot T_{r,0}(n)}{\sum_{k=1}^{3} T_{r,0}(k)} \neq \frac{3 \cdot T_{r,1}(n)}{\sum_{k=1}^{3} T_{r,1}(k)} \tag{3.14}$$

Therefore, one-step interpolation cannot convert Ω_r to a constant value for WTG fault detection. A recursive process is needed to keep searching for a better solution until an acceptable c_r, defined in (3.9), is achieved, where the difference between $f_{r,i}$ and $f_{r,i+1}$ is small and negligible.

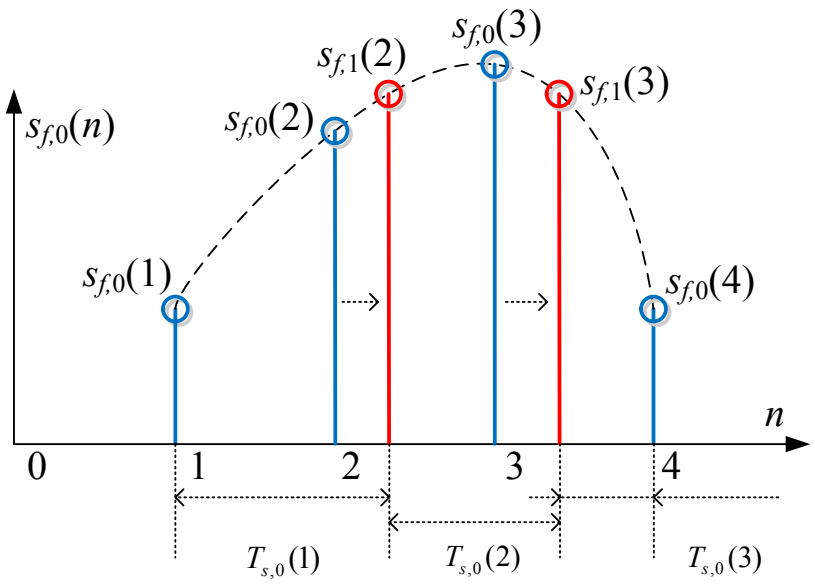

Figure 3.6: An example of implementation of the high-performance 1P-invariant PSD method.

In the following classical PSD calculation, the shaft rotating frequency f_r becomes a constant value F_r in the high-performance 1P-invariant PSD of the current demodulated signal. The value of F_r needs to be determined for WTG fault detection. In the proposed method, the total number of cycles of the shaft rotating frequency signal are the same before and after the resampling, which can be expressed by:

$$\sum_{n=1}^{N-1} f_{r,0}(n) \cdot T_{s,0} = F_r \cdot T_{s,0} \cdot (N-1) \tag{3.15}$$

where $T_{s,0}$ is sampling interval of the current signal and is a constant value. Therefore, the constant shaft rotating frequency F_r in the high-performance 1P-invariant PSD of the current demodulated signal is the mean value of the estimated shaft rotating frequency signal $f_r(n)$, given as follows.

$$F_r = \frac{\sum_{n=1}^{N-1} f_{r,0}(n)}{N-1} \tag{3.16}$$

3.2.2 Verification of high-performance 1P-invariant PSD method

The high-performance 1P-invariant PSD method is validated by using the same artificial sinusoidal signal in section 3.1. The artificial sinusoidal signal is processed by using the proposed method to illustrate the convergence and the performance of converting the variable frequency of the artificial sinusoidal signal to a constant value, where the number of iterations is three. The artificial sinusoidal signal and its processed results after each iteration of the proposed method are compared in Figure 3.7. By using the high-performance 1P-invariant PSD method, the nonstationary artificial sinusoidal signal is converted to a stationary signal step by step. In Figure 3.7, the processed result of the artificial sinusoidal signal after the third iteration is almost a stationary sinusoidal signal. The PSDs of the artificial sinusoidal signal and its processed result after the third iteration are compared in Figure 3.8. The excitations of the artificial sinusoidal signal are in the range of 0.1 Hz to 1 Hz; while the excitation of the high-performance 1P-invariant PSD method processed result of the artificial sinusoidal signal after the third iteration is constant at 0.55 Hz, which is the average frequency of the artificial sinusoidal signal. The result demonstrates the effectiveness of the high-performance 1P-invariant PSD method for converting the variable frequency of a sinusoidal signal to a constant value.

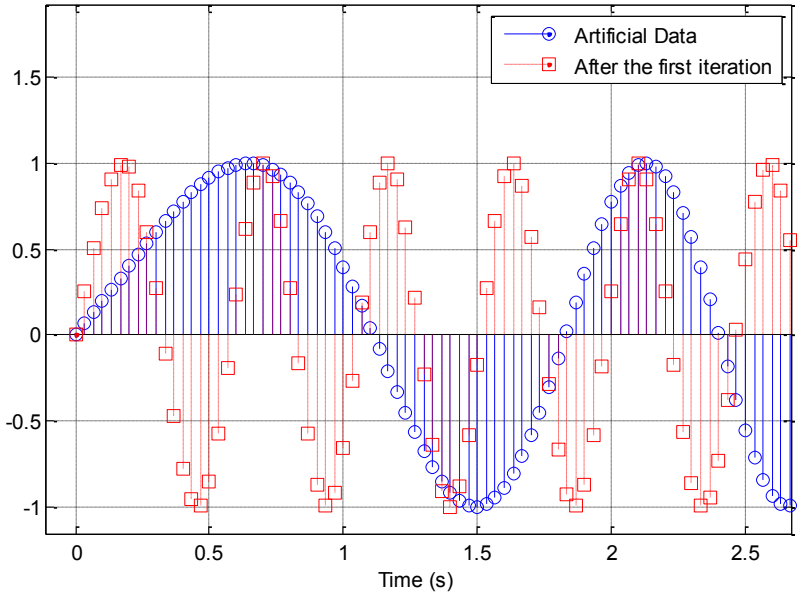
Artificial Data
After the first iteration
1.5
1
0.5
0
-0.5
-1
0
0.5
1
1.5
2
2.5
Time (s)

(a)

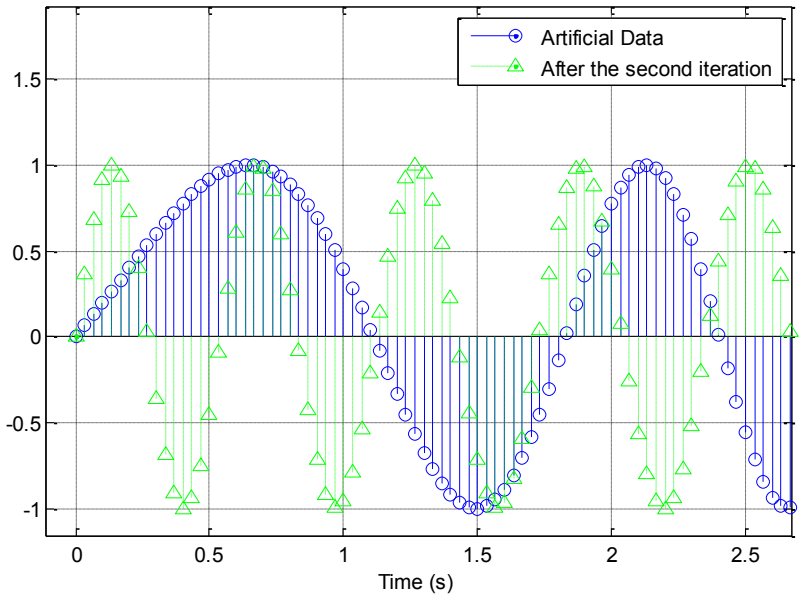
Artificial Data
After the second iteration
1.5
1
0.5
0
-0.5
-1
0
0.5
1
1.5
2
2.5
Time (s)

(b)

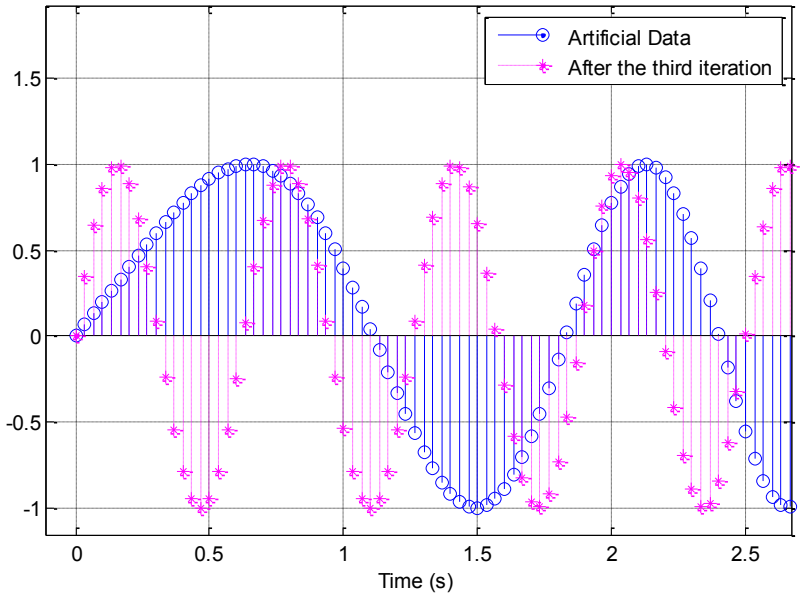

(c)

Figure 3.7: Comparison between the artificial sinusoidal signal and its processed results after (a) the first iteration, (b) the second iteration, and (c) the third iteration.

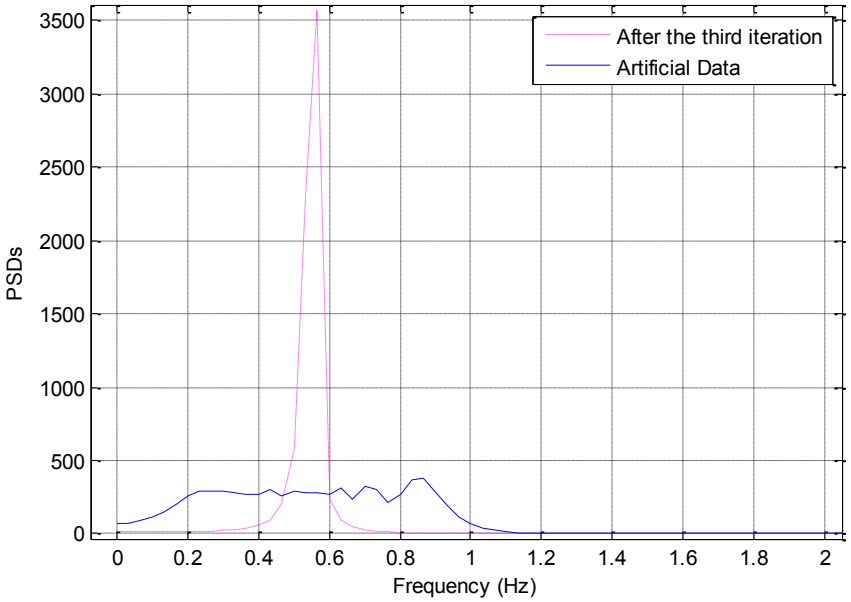

Figure 3.8: PSDs of the sinusoidal artificial signal and its high-performance 1P-invariant PSD method processed result after the third iteration.

3.3 Benefits of Using Current Demodulated Signals

In previous research, current measurements have been directly used for electric machine fault detection. For instance, to directly apply current measurements for electric machine bearing fault detection, the influence of bearing faults in the current signals needs to be modeled. The most frequently used model is given in [43] for induction machine bearing fault detection. Reference [44] extended the result of [43] by taking into account both the radial rotor movement and the shaft torque variation of electric machines in bearing fault condition. The current signals are modulated by the characteristic frequency f_{fault} of a bearing fault in vibration measurements, where f_{fault} is one of the bearing fault characteristic frequencies given in (2.4)-(2.7). The characteristic frequencies of bearing faults in the modulated current signals are summarized in Table 3.1, where $l = 1, 2, \cdots$; $f_{c.i}$, $f_{c.o}$, $f_{c.b}$ and $f_{c.c}$ are the characteristic frequencies of a bearing inner-race fault, outer-race fault; ball fault; and cage fault in current signals, respectively; and f_1 is the fundamental frequency of the current signal. The harmonics of electric machine current signals are also modulated by the bearing fault characteristic frequencies in vibration measurements [127]. Since the harmonics of current signals have much lower magnitudes than the fundamental-frequency component, the excitations at the harmonics due to bearing faults are minor and are not listed here.

Table 3.1: Characteristic Frequencies of Bearing Faults in Current Measurements

	Radial rotor movement [43]	Radial rotor movement [44]	Shaft torque variation [44]
Inner-race fault	$f_{c.i} = f_1 \pm l \cdot f_i$	$f_{c.i} = f_1 \pm f_r \pm l \cdot f_i$	$f_{c.i} = f_1 \pm l \cdot f_i$
Outer-race fault	$f_{c.o} = f_1 \pm l \cdot f_o$	$f_{c.o} = f_1 \pm l \cdot f_o$	$f_{c.o} = f_1 \pm l \cdot f_o$
Ball fault	$f_{c.b} = f_1 \pm l \cdot f_b$	$f_{c.b} = f_1 \pm f_c \pm l \cdot f_b$	$f_{c.b} = f_1 \pm l \cdot f_b$
Cage fault	$f_{c.c} = f_1 \pm l \cdot f_c$	N/A	N/A

Similarly, the current signal is also modulated by the characteristic frequency f_{fault} of other WTG faults, which generates oscillations in the shaft torque of the WTG with a characteristic frequency of f_{fault}. Therefore, the characteristic frequency of a WTG fault in the modulated current signal is:

$$f_{c.fault} = f_1 \pm l \cdot f_{fault} \tag{3.9}$$

Using the current demodulated signals for WTG fault detection has obvious advantages over directly using the current measurements. The major noise in the current signals and the current demodulated signals are fundamental-frequency component and the DC component, respectively. The DC component can be easily removed compared to the fundamental-frequency component. However, useful information for WTG fault detection is easily interfered by fundamental-frequency component when the WTG operates in variable-speed operating conditions. Moreover, when a WTG fault occurs, only one main fault characteristic frequency f_{fault} will appear in the current demodulated

signals. On the other hand, there are multiple characteristic frequencies, as given in Table 3.1, in current signals. If current measurements are directly used for WTG fault detections, the energy of excitations related to WTG faults are dispersed into multiple characteristic frequencies. Therefore, the magnitudes of excitations at those multiple characteristic frequencies are less detectable than that of excitation at f_{fault} in the current demodulated signals, which have only one characteristic frequency f_{fault} of the WTG fault.

Chapter 4 Wavelet-Based Filter

As mentioned in Chapter 1, not all WTG faults lead to an excitation at the characteristic frequency. For instance, bearing faults can be categorized as two types: single-point faults and generalized roughness (incipient bearing faults), according to different stages of the fault development process. Incipient bearing faults do not generate any excitation at the characteristic frequency [35]. Much research effort has gone into the detection of single-point faults, where the fault characteristic frequencies are clear indicators for a present damage [93]. In fact, generalized roughness faults have also been observed in a significant number of cases of failed bearings from various industrial applications [35]. This type of faults exhibits degraded bearing surfaces, but not necessarily distinguished faults. However, little research has been done on detection of incipient generalized roughness faults, which will be the objective of this chapter. This chapter proposes a novel wavelet filter-based method for WTG incipient bearing fault detection using generator current measurements. The proposed wavelet-based filter is based on the discrete wavelet transform (DWT) and wavelet shrinkage [128]. The latter is a classical algorithm for noise elimination by using DWT.

4.1 Wavelet-Based Filter for WTG Incipient Bearing Fault Detection

In the frequency domain, the dominant components of current signals of an induction machine are the fundamental-frequency component and its multiple harmonics, e.g., the eccentricity, slot and saturation harmonics, and other components from unknown sources including environmental noise [129]. This conclusion is also true for the generators used in WTGs. These dominant components are not created by bearing faults.

In this sense, they are treated as noise in the problem of bearing fault detection. To discover the bearing fault index in the current measurements, it is desired to remove those dominant noise components from the measured current signals.

Since the incipient bearing faults do not have characteristic frequencies [35], traditional frequency-domain analysis based methods are not effective to detect this type of faults. In this chapter, the energy of the bearing fault related component in a current signal is extracted by using a wavelet-based filter, where the energy is defined as the square of the signal processed. Because the vibration of an electric machine is positively correlated to the degradation of bearings, the amplitude of the energy of the bearing fault related component indicates a physical condition of the bearing. If the amplitude of the fault related energy remains at a high level or vibrates with a large magnitude, it means the degradation of the bearing and maintenance is required. This section proposes a wavelet-based filter, which can eliminate the dominant components in the current measurements that are not related to the bearing faults. The energy of the filtered current signal is then chosen as the fault index for incipient bearing fault detection.

4.1.1 Wavelet decomposition

The continuous wavelet transform (CWT) of a time-domain signal $f(t)$ is given by [130]:

$$W_{CWT}(a,b) = \left|a^{-1/2}\right| \int f(t) \cdot \psi\left(\frac{t-b}{a}\right) \cdot dt \tag{4.1}$$

where ψ is a wavelet function; a is a scaling parameter; and b is a time shifting parameter. For incipient bearing fault detection of WTGs, the discrete wavelet transform is applied by discretizing (4.1) and the result is given by [130]:

$$W_{DWT}(m,n) = \left|a^{-m/2}\right| \int f(t) \cdot \psi(a_0^{-m} t - n b_0) \cdot dt \tag{4.2}$$

where m and n are integers; $a_0 > 1$ and $b_0 > 0$ are constant.

In the algorithm of DWT, a wavelet function is associated with a scaling function. The wavelet function and the scaling function are finite vectors. The original data is decomposed into trend subsignals by the scaling function and into fluctuations by the wavelet function. The wavelet decomposition is recursive, as shown in Figure 4.1. This is known as multiresolution analysis [131]. Each of the trend subsignals and fluctuations contains the time-domain features of the original data in a finite frequency band.

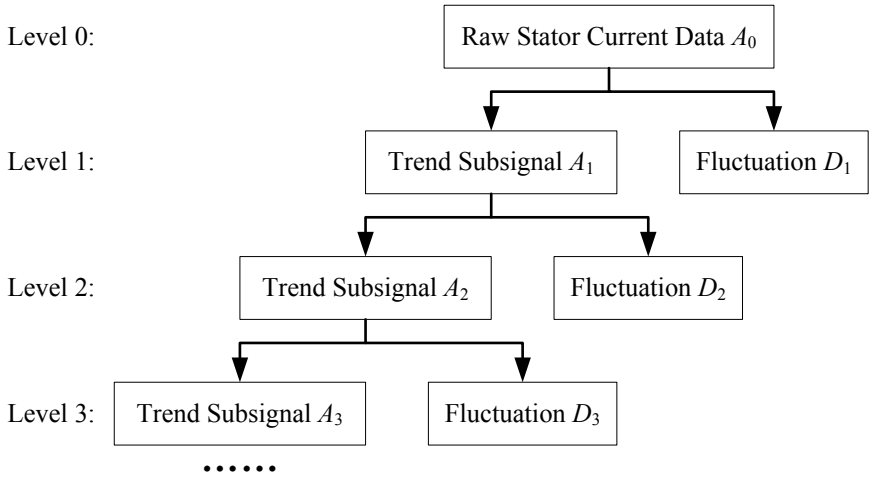

Figure 4.1: Schematic diagram of a wavelet decomposition.

Assume that the wavelet function is $W(x) = [w_1, w_2, \cdots, w_{2k}]$ and the scaling function is $V(x) = [v_1, v_2, \cdots, v_{2k}]$, where k is a positive integer. The wavelets and scaling signals need to be generated first for the wavelet decomposition. The wavelets $W_{i,m}$ are:

$$W_{i,m} = [0,\ldots 0, w_1, w_2, \cdots, w_{2k,} 0,\ldots 0],\ m = 1,\cdots, N_{i-1}/2\text{-}k\text{+}1 \tag{4.3}$$

$$W_{i,m} = [w_{2j+1}, \ldots w_{2k,}0,\ldots 0, w_1, \ldots w_{2j,}],\ m = N_{i-1}/2\text{-}k\text{+}2,\cdots, N_{i-1}/2 \tag{4.4}$$

where $i = 1, 2, 3,\cdots$ is the level of the wavelet decomposition in Figure 4.1; j is a positive integer, which is smaller than k; the length of $W_{i,m}$ is N_{i-1}; w_1 is the $(2m\text{-}1)^{th}$ element of $W_{i,m}$ in (4.3) and (4.4). The scaling signals $V_{i,m}$ are:

$$V_{i,m} = [0,\ldots 0, v_1, v_2, \cdots, v_{2k,} 0,\ldots 0],\ m = 1,\cdots, N_{i-1}/2\text{-}k\text{+}1 \tag{4.5}$$

$$V_{i,m} = [\ v_{2j+1}, \ldots v_{2k,} 0,\ldots 0, v_1, \ldots v_{2j,}],\ m = N_{i-1}/2\text{-}k\text{+}2,\cdots, N_{i-1}/2 \tag{4.6}$$

where the length of $V_{i,m}$ is N_{i-1}; v_1 is the $(2m\text{-}1)^{th}$ element of $V_{i,m}$ in (4.5) and (4.6).

At each level of the wavelet decomposition, the value $d_{i,m}$ of each element of the fluctuation $D_i=(d_{i,1}, d_{i,2}, \ldots, d_{i,m})$ is [83]:

$$d_{i,m} = A_{i-1}\cdot V_{i,m}, \quad m = 1,\cdots, N_{i-1}/2 \tag{4.7}$$

where $V_{i,m}$ is the scaling signal at the level i generated from the scaling function by using (4.5) and (4.6).

The performance of the DWT depends on the wavelet function chosen for decomposition. In this research, the Coiflet wavelet is applied due to its feature of vanishing moments. The vanishing moments of a wavelet function means that several moments of the wavelet function are zero. The vanishing moments of the Coiflet wavelet

are designed not only in the wavelet function but also in the scaling function. The following equations illustrate such a feature for a continuous Coiflet wavelet [130]:

$$\int V(x)\cdot dx = 1; \tag{4.8}$$

$$\int x^l \cdot W(x)\cdot dx = 0, for: l = 0,1,...,L_w - 1; \tag{4.9}$$

$$\int x^l \cdot V(x)\cdot dx = 0, for: l = 1,2,...,L_w - 1; \tag{4.10}$$

$$N_s = 3\cdot L_w - 1 \tag{4.11}$$

where $W(x)$ is the wavelet function; $V(x)$ is the scaling function; L_w is the order of the Coiflet wavelet; N_s is the support length of the Coiflet wavelet. The support length measures the effective width of a wavelet function. Equations (4.9) and (4.10) give the vanishing moments in the wavelet function and the scaling function of the Coiflet wavelet, respectively. Because of this feature, the Coiflet wavelet has the features of symmetry and compactness for numerical analysis applications [132]. In this research, the dominant noise components in the current measurement that are irrelevant to the bearing fault needs to be maximally compacted. The Coiflet wavelet is a good candidate to implement such compaction.

4.1.2 Choosing the support length for wavelet functions

The support length is an important parameter of a wavelet function. It determines the capability of compacting energy of a wavelet function in the DWT. The Coiflet wavelet functions with different support lengths are used to design the wavelet transform to maintain a close match between the trend values and the original signal values [83]. However, there are no rules for selecting the support length of the Coiflet wavelet in the

DWT. Therefore, a pretreatment scheme is proposed to choose the support length of the wavelet function in the filter.

When the WTG bearing is in the healthy condition, the Coiflet wavelets of different support lengths are applied to decompose the current signal. The Coiflet wavelet that can compact the largest energy of the current signal to a certain percent (e.g., 5%) of the whole length of the data is selected as the wavelet function for following fault detection. The resulting Coiflet wavelet is assumed to have the most powerful capability to compact the dominant noise components of the current signal into subsignals through the DWT. The schematic diagram of the pretreatment scheme is illustrated in Figure 4.2, where L_w is an even integer.

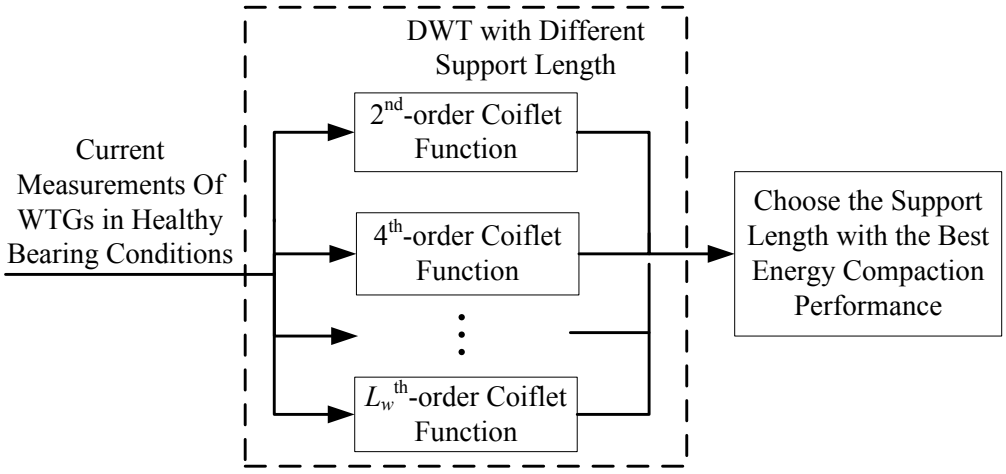

Figure 4.2: Schematic diagram of the pretreatment for choosing the support length of the Coiflet wavelet.

4.1.3 Proposed wavelet-based filter

The proposed wavelet-based filter is based on the DWT and wavelet shrinkage. The DWT is used to decompose the current signals into different components; and the wavelet shrinkage works in a similar way to an adaptive notch filter to remove the dominant noise components from the decomposed current signals. The resulting filtered signal is mainly related to the bearing fault.

The wavelet shrinkage is a traditional method for filter design [128]. In this research, the bearing fault signature in raw current measurements is subtle and broad-band. Therefore, the wavelet shrinkage should be operated to cancel the dominant noise components that are irrelevant to the bearing faults. The proposed wavelet-based filter is implemented as follows:

(1) Decompose a batch of current signal $C(n) = [c(1), c(2), \cdots, c(N)]$ by using the DWT with a 2^{nd}-order Coiflet wavelet and the result is $C_w(n) = [c_w(1), c_w(2), \cdots, c_w(N)]$.

(2) Calculate the energy of $C_w(n)$ and the result is $E_w(n) = [e_w(1), e_w(2), \cdots, e_w(N)]$, where $e_w(n) = c_w^2(n)$.

(3) Calculate the sum from $E_w(N/2+1)$ to $E_w(N)$ and the result is I_w, which is the total energy of fluctuations in the wavelet decomposed current samples $C_w(n)$. I_w is defined as an index of the energy of the components related to the bearing fault, i.e., the fault signature, in the current signal.

The amplitude of I_w indicates the physical condition of the bearing. If the amplitude of I_w remains at a high level or vibrates with a large magnitude, it indicates the degradation of the bearing and maintenance is required.

The DWT decomposes the original signal into two parts: trend subsignal and fluctuation. The high energy components of the original signal are compacted into its trend subsignal; while the fluctuation only contains the weak energy components. This is called the compaction of energy, which is one of the main characteristics of the DWT [83]. The proposed wavelet-based filter can eliminate the high energy components in the current signals, which are the dominant noise components irrelative to the bearing faults. Therefore, the fault signature can be discovered by using the wavelet filtered current signals. As the physical condition of the bearing becomes worse and worse, the energy of the fault related components in current signals becomes more and more significant, which results in an increase of I_w.

The schematic diagram of the proposed wavelet filter-based bearing fault detection algorithm is illustrated in Figure 4.3. The low-pass filters are used for anti-aliasing. The baseline current signals are the first several samples obtained from the healthy bearing, as it is assumed that the bearing is healthy initially. These baseline data are used to determine the support length of the Coiflet wavelet.

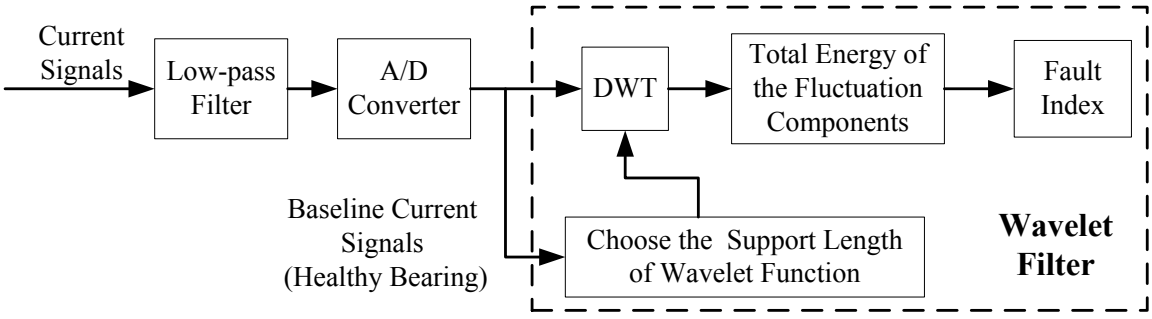

Figure 4.3: Schematic diagram of the proposed wavelet filter-based bearing fault detection algorithm.

4.2 Validating the Wavelet-Based Filter Using Artificial Data

The effectiveness of the proposed wavelet-based filter is validated by using artificial data. The artificial data consist of two parts. One part emulates the narrow-band dominant noise components in the current measurements that are irrelevant to bearing faults, defined as:

$$g(n) = \sum_{m=1}^{M_{nb}} A_m \cdot \sin(\omega_m n + \theta_m) \tag{4.12}$$

where $g(n)$ is the fault-irrelevant noise components, n = 1, 2, 3, …, N and N is the length of the artificial data; A_m, ω_m and θ_m are the amplitude, angular frequency and phase angle of each sinusoidal component. In this research, M_{rb} is 4 in (4.12), where the angular frequencies ω_m of the four different fault-irrelevant noise components are $\pi/3$, $2\pi/3$, π and $4\pi/3$, respectively. They emulate the fundamental current signal and its multiple harmonics. The broad-band bearing fault component is assumed to be a Gaussian white noise. A Gaussian white noise with a higher magnitude means a worse physical condition of the bearing. Therefore, the whole emulated current signal $s_w(n)$ is:

$$s_w(n) = g(n) + N_{Gaussian}(n) \tag{4.13}$$

where $N_{Gaussian}$ (n) is the Gaussian white noise.

One hundred realizations of $s_w(n)$ are generated to emulate the degradation of the bearing condition through adding a Gaussian white noise in each realization. The SNR of $s_w(n)$ reduces linearly from 50 dB for the first realization to 30 dB for the last realization. The reduction of the SNR leads to the increase of the Gaussian white noise in $s_w(n)$. In

order to simulate the variable-speed operation of a WTG, the amplitude A_m, angular frequency ω_m, and phase angle θ_m of $g(n)$ in (4.12) are randomly varied in a range of 0.8 to 1.2, $0.8\times\omega_m$ to $1.2\times\omega_m$, and $-\pi$ to π, respectively.

When applying the proposed wavelet-based filter to the artificial data, the 6^{th} order wavelet function, Coiflet3, is used. The simulation results are shown in Figures 4.4 and 4.5. Figure 4.4 shows the PSDs of four realizations, which obviously have different narrow-band dominant frequencies with each other, indicating emulated variable-speed condition of a WTG. Figure 4.5 shows the remaining energy of the emulated fault component, i.e., the Gaussian white noise, obtained from the wavelet-based filter, which clearly shows that the energy of the broad-band fault component increases with the number of realization. These results demonstrate the effectiveness of the proposed method, namely, the wavelet-based filter is able to detect the increasing energy of the broad-band bearing fault component in WTG current measurements.

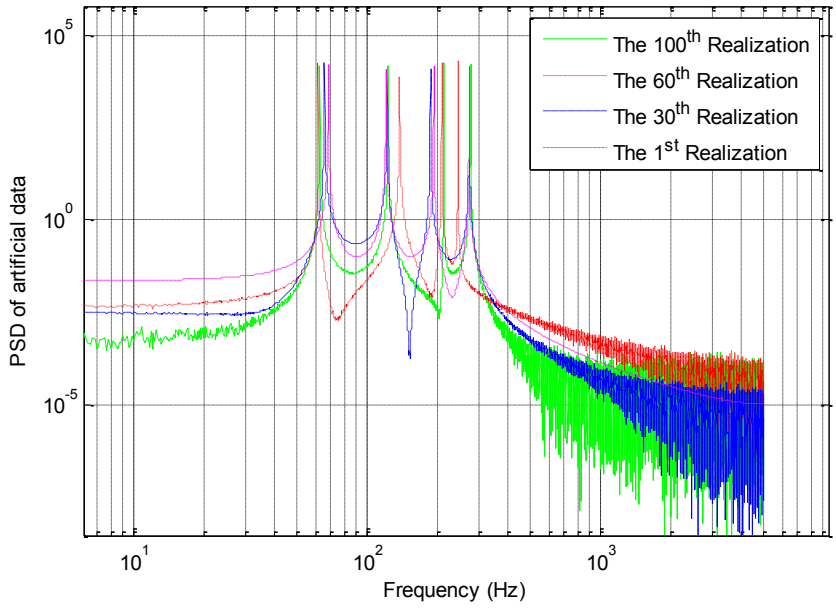

Figure 4.4: PSDs of four realizations.

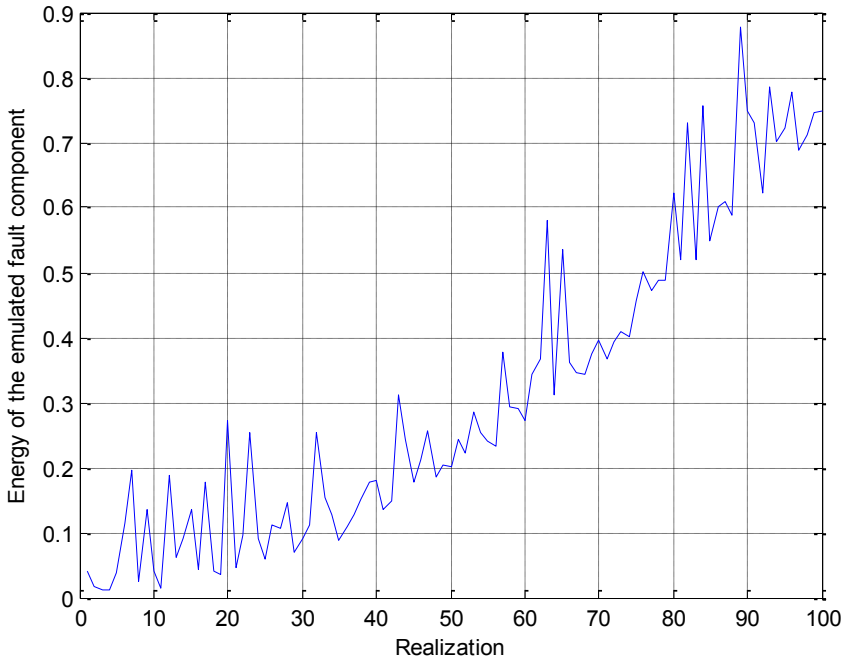

Figure 4.5: Energy of the emulated fault component vs. number of realization.

Chapter 5 Fault Signature Evaluation

As shown in Figure 1.2 of Chapter 1, the fault signatures of Type 1 WTG faults and fault indexes of Type 2 WTG faults need to be further analyzed to evaluate the physical condition of the WTGs. The excitations in the processed current signals generated by WTG faults will be found by using an impulse detection method. Once an impulse at the characteristic frequency of a WTG fault is detected, it indicates the occurrence of the fault and maintenance is required. For the WTG fault which does not have a characteristic frequency, a fault index evaluator is applied to the wavelet-based filter processed current signals to determine the physical condition of the wind turbine component and whether maintenance is required. This chapter proposes an impulse detection method to detect WTG Type 1 faults, which generate excitations at the fault characteristic frequencies in the 1P-invariant PSDs of the current demodulated signals. A statistical control method [108] is applied to design a fault index evaluator to detect the Type 2 WTG faults.

5.1 Impulse Detection Method

In practical applications, it is desired to evaluate the physical condition of WTGs solely based on the fault signature in real time. When a WTG fault signature is detected, it indicates that the WTG component corresponding to the fault signature is in a deteriorated condition and maintenance is required. For a WTG fault which generates excitations at the desired fault characteristic frequencies in the 1P-invariant PSDs of the processed current demodulated signals, an impulse detection method can be applied to find out the signature of the WTG fault. There are many impulse detection methods based on signal statistics [133], fuzzy algorithm [134], and median filter [135]. The design of an

impulse detection algorithm depends on the patterns of the signals to be processed. An effective method for detecting impulses in the frequency spectra of the processed current demodulated signals is desired in this research.

This section proposes a current-based online WTG fault signature evaluation method via impulse detection. The proposed impulse detection method is able to detect and quantize the excitations (i.e., impulses) generated by the WTG faults in the 1P-invariant PSDs of the current demodulated signals. The impulses detected are then used to evaluate the health condition of the corresponding wind turbine components. The proposed method is validated by using artificial data.

5.1.1 Proposed impulse detection method

The proposed 1P-invariant PSD methods can be used to convert the variable-frequency excitations of WTG faults to constant-frequency values in the frequency domain. To facilitate the implementation of the WTG fault detection in real-world automatically controlled and operated wind turbine systems, an impulse detection method is developed for automatic extraction of fault signatures in the 1P-invariant PSDs of the current demodulated signals.

In a PSD spectrum, the amplitude at a frequency represents the energy of the time-domain signal at that frequency. If the signal has high energy around a certain frequency, it will generate an impulse in the PSD at that frequency. The proposed impulse detection method is able to find out the high-energy frequency component in the 1P-invariant PSDs of current demodulated signals. It has been reported that the spectra of the vibration of a WTG with three blades are determined by certain events. For instance, the

vibration at 3P frequency, which is three times the shaft rotating frequency f_r of a WTG, is generated by the effect of yaw error, wind shear, or tower shadow [136]. This is also true for the WTG current demodulated signals. The 3P frequency excitations in the 1P-invariant PSDs of the current demodulated signals are noise in WTG fault detection. Therefore, the excitations at 3P frequency of the 1P-invariant PSD signals are firstly removed as a pretreatment. Furthermore, the 1P-invariant PSDs of the current demodulated signals usually have nonstationary amplitudes in the frequency domain. Therefore, the 1P-invariant PSDs need to be processed locally in terms of the frequency for impulse detection, which is described as follows.

Assume that $X_{PSD}(f)$ is the sampled 1P-invariant PSD of a current demodulation signal, where f = 1, 2, 3, … F; and F is the length of $X_{PSD}(f)$. Define the energy of the current demodulated signal at frequency f to be:

$$P_x(f) = X_{PSD}(f) \tag{5.1}$$

If a moving window of length $2W_w+1$ is applied to X_{PSD} (f), the energy in the window is defined as:

$$P_W(f) = X_{PSD}(f - W_w) + X_{PSD}(f - W_w+1) + \ldots + X_{PSD}(f+W_w) \tag{5.2}$$

A ratio $R(f)$ is defined to be the percentage of the energy of the current demodulated signal at the frequency f with respect to the total energy at all the frequencies contained in the moving window:

$$R(f) = P_x(f) / P_W(f) \tag{5.3}$$

The resulting $R(f)$ represents the locally normalized 1P-invariant PSD of the current demodulated signal. If $R(f)$ at a certain frequency point is greater than a threshold

T_i, it indicates that there is an impulse at that frequency. In practice, it is important to automatically generate the threshold T_i from the locally normalized 1P-invariant PSD signals. The median filter, which is a well-known nonlinear filter for impulse removal [135], is applied to determine the threshold T_i. Define $R_f(f)$ the result of $R(f)$ processed by a median filter. The threshold T_i is then set to be the maximum value of $R_f(f)$. Since the impulses that are not generated by WTG faults have been removed in the pretreatment of the 1P-invariant PSDs of the current demodulated signals, the impulses generated by WTG faults have the highest amplitudes in the locally normalized 1P-invariant PSDs of the current demodulated signals and can be detected effectively by the proposed method. In this work a 3rd-order median filter is chosen to calculate the threshold T_i. The $R_f(f)$ is calculated by:

$$R_f(f) = F_{Median}[R(f-1), R(f), R(f+1)] \tag{5.4}$$

where $f = 1, 2, 3, \ldots F$; $F_{Median}[\cdot]$ stands for selecting the median in the set. The threshold T_i is then determined to be:

$$T_i = F_{Max}[R_f(f)] \tag{5.5}$$

where $F_{Max}[\cdot]$ stands for choosing the maximum value in $R_f(f)$ for $f = 1, 2, 3, \ldots F$.

In the 1P-invariant PSDs, the amplitudes of the impulses at the characteristic frequencies of WTG faults are the signatures for WTG fault detection. Since there are no impulses at the characteristic frequencies of the WTG faults when the WTGs are in healthy conditions, if an impulse is detected at the characteristic frequency of a WTG fault, it indicates a faulted condition of the WTG. In this case an alert is generated.

5.1.2 Verification of the impulse detection method

To verify the proposed impulse detection method, an artificial PSD of a current demodulated signal is used. Since the dominant components of WTG current demodulated signals spread over the low-frequency region in the frequency domain, the amplitude of the low-frequency part of the artificial PSD signal is higher than that of the high-frequency part. To simulate an excitation generated by a WTG fault, an impulse is added at a particular frequency. The artificial PSD of the current demodulated signal $x_p(f)$ in WTG fault conditions is shown in Figure 5.1 and given by:

$$x_p(f) = x_{p,h}(f) + A_f \delta(f) \tag{5.6}$$

where $x_{p,h}(f)$ is the artificial PSD of the current demodulated signal obtained when the WTG is in the healthy condition, whose low-frequency part has high amplitude; $\delta(f)$ is the impulse related to the WTG fault added at 9 Hz; A_f is the amplitude of the impulse. $\delta(f)$ is given by:

$$\delta(f) = \begin{cases} 1, & f = 9 \\ 0, & f \neq 9 \end{cases} \tag{5.7}$$

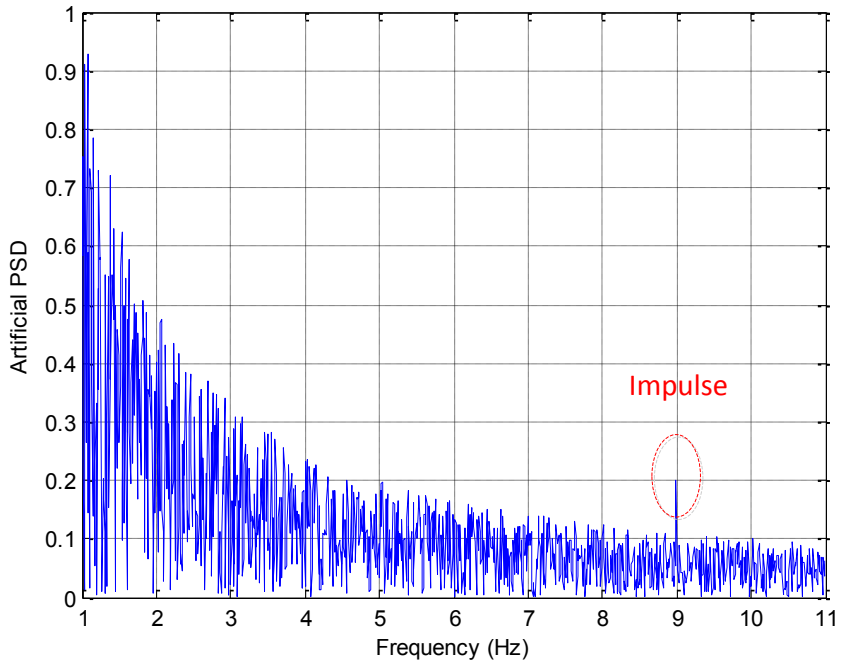

Figure 5.1: Artificial PSD of a current demodulated signal in WTG fault conditions.

When applying the proposed impulse detection method to the artificial PSD signal, the length of the window, W_w, is chosen to be 41. A third-order median filter is used for threshold calculation. The locally normalized artificial PSD [i.e., $R(f)$] is plotted in Figure 5.2. The threshold T_i is calculated to be 0.052. The impulse appears at 9 Hz, which is the excitation generated by the simulated WTG fault. In Figure 5.1, the excitation at 9 Hz is not the global maximum value. Therefore, it is difficult to detect the 9-Hz impulse directly in the artificial PSD signal without the locally normalization. By using the locally normalization process in the proposed method, the 9-Hz impulse becomes the maximum value in Figure 5.2. By using the third-order median filter to determine the threshold, the 9-Hz impulse is successfully detected by using the proposed method.

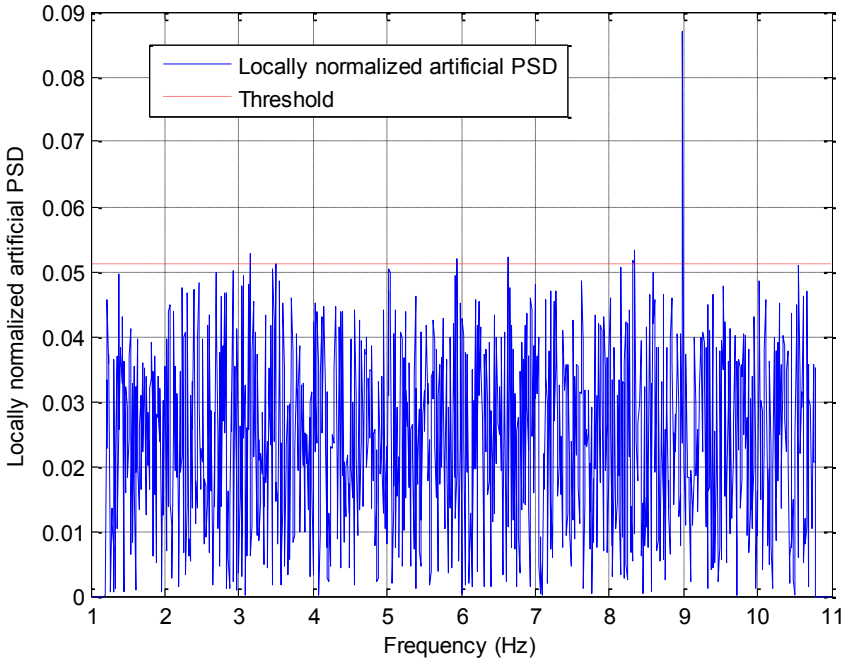

Figure 5.2: Locally normalized artificial PSD of a current demodulated signal in WTG fault condition.

5.2 Fault Index Evaluator for Type 2 WTG Fault

It was mentioned in Chapter 4 that the index of a Type 2 WTG fault, which is obtained by using the wavelet-based filter, increases when the WTG physical condition degrades. It is desired to evaluate the health condition of the corresponding WTG component solely based on the value of the fault index in real time. This function is achieved by a fault index evaluator, which establishes a threshold or limit on the fault index. When the fault index frequently exceeds the threshold, it indicates that the WTG is in a deteriorated condition and maintenance is required. In this section, a statistical control method [108] is used to design the fault index evaluator to determine the threshold for the WTG fault index.

5.2.1 Standard deviation

Standard deviation is a measure of extent of variation of the data processed. The standard deviation perhaps can be most easily explained in terms of normal distribution (μ, σ^2), where μ and σ are the mean (or center) and standard deviation, respectively. If the measurements from a stationary random process are normally distributed, then 68.3% of the measurements will fall within 1-σ distance from the central μ, 95.4% within 2-σ, and 99.7% within 3-σ. A normal distribution (0, σ^2) is shown in Figure 5.3. Therefore, one may be confident that almost all measurements will lie between the values of $\mu \pm 3\sigma$ if the process is stationary. In other words, if new measurements of the process frequently fall outside the 3-σ region, then the process is no longer stationary. If an individual measurement from the stationary random process is not normally distributed, according to the central limit theorem, the distribution of sample means will tend to have a normal distribution with a mean and a standard deviation. The larger the number of samples is, the greater this tendency will be. Therefore, for practical engineering problems, it can be assumed that the distribution of the sample means is normal even if the original samples are not normally distributed [137].

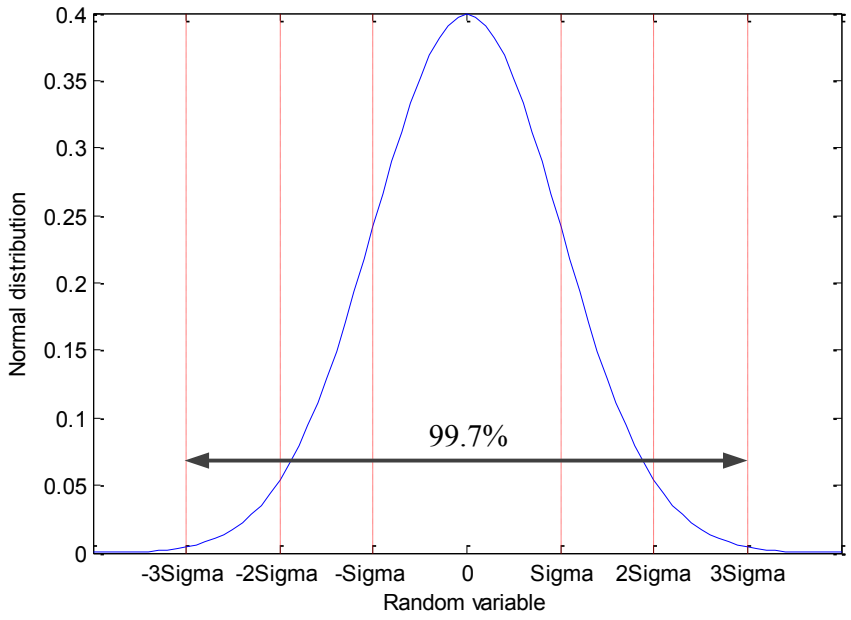

Figure 5.3: A normal distribution $(0, \sigma^2)$.

5.2.2 Threshold determination

For WTG fault detection, the calculated fault indexes can be treated as output measurements of the complex wind turbine process, which represents the physical condition of the WTG components. When the WTG components are in healthy condition, the fault indexes are stationary and smaller than the value of $\mu+3\sigma$, where μ and σ are the mean and standard deviation of the fault indexes obtained when the WTG is in healthy condition. In the case that fault indexes are smaller than the value of $\mu-3\sigma$, the WTG components are also assumed to be in healthy condition. Assume that the samples of a fault index are $I_w(n)$, n = 1, 2, 3, …N, where N is the length of the fault index samples obtained when the WTG is in healthy condition. The μ and σ are calculated by:

$$\mu = \sum_{n=1}^{N} I(n) / N \tag{5.8}$$

$$\sigma = \sqrt{\sum_{n=1}^{N} (I(n) - \mu)^2 / N} \tag{5.9}$$

The fault index increases when the physical condition of the corresponding WTG component degrades. In this case, the fault index samples will frequently exceed the value of $\mu+3\sigma$ calculated by (5.8) and (5.9). Therefore in this research, the value $\mu+3\sigma$ of the fault index obtained when the WTG is in healthy condition is chosen as the threshold to determine the physical condition of the corresponding WTG component. When the fault index frequently exceeds the threshold $\mu+3\sigma$, it indicates that the WTG is in a deteriorated condition and maintenance is required.

Base on the analysis in Chapter 2, the characteristic frequency of wind turbine imbalance fault is 1P, i.e., the shaft rotating frequency f_r. In ideal conditions, there is no any excitation at the 1P frequency in the 1P-invariant PSD spectra of the current demodulated signals. However, WTGs are inevitably subjected to a certain degree of imbalance due to manufacturing and construction errors, icing, deformation, etc. Therefore, small excitations may appear at the 1P frequency in the 1P-invariant PSD spectra of the current demodulated signals obtained from a healthy WTG. The proposed statistical control-based method can also be used for wind turbine imbalance fault evaluation by setting the amplitude of the excitation at the 1P frequency as the fault index.

Chapter 6 WTG Simulation and Experimental Setups

Simulations and experiments are performed in this research to verify the proposed online nonintrusive WTG condition monitoring and fault detection methods. The simulation study is based on a finite element WTG model. A commercial wind turbine is used in the experimental study. In this chapter, the simulation and experimental setups are described to facilitate other researchers to verify the methods proposed in this work.

6.1 Simulation Setup

FAST (Fatigue, Aerodynamics, Structures, and Turbulence) version 7.0 is chosen for simulation studies of this research. FAST, an aeroelastic code developed initially by Oregon State University, is one of the most advanced design codes for horizontal-axis wind turbine [138]. Much work has been done by using FAST in the area of wind energy. A DFIG wind turbine was simulated by using FAST and Simulink to study the interaction of all three factors affecting the operation of the WTG [139]. The impact of tower shadow, yaw error, and wind shears on wind turbines was studied by using FAST software in [136]. FAST was also applied to DFIG wind turbines to demonstrate the correctness of an individual pitch control strategy [140]. TurbSim, a program developed by the National Renewable Energy Laboratory (NREL), is a stochastic, full-field, turbulent wind simulator [141]. TurbSim is often used to provide three-dimensional wind speed data to FAST for wind turbine simulations [78], [136], [139].

This section describes the simulation platform used to validate the WTG condition monitoring and fault detection methods proposed in this research. The

dynamical model of a WTG is developed in a combined environment of TurbSim, FAST and Simulink, where TurbSim generates the wind speed data; FAST simulates the dynamics of the turbine and other mechanical components; and Simulink simulates the dynamics of the generator and other electrical components of the WTG system. Furthermore, the methods of generating WTG faults and the available measurements of the WTG model developed are also presented.

6.1.1 WTG model

The dynamical model of a 10-kW WTG system is built in a TurbSim, FAST and Simulink combined environment, as shown in Figure 6.1. In this simulation setup, FAST works as a subroutine in Simulink. The signals of the electric power, electric torque, and rotating speed are used to connect the FAST and Simulink models of the WTG system. The files used in FAST for wind turbine simulation are listed in Table 6.1.

Table 6.1: Files Used in FAST

Function	File name
Simulation input file	Test17.fst
Model of blades	SWRT_Blade.dat
Model of furl	SWRT_Furl.dat
Model of tower	SWRT_Tower.dat
Wind turbine rotor aerodynamic parameters	Test17_AD.ipt

The model wind turbine in FAST mainly includes tower, blades, shaft, furl and support platform. The hub height of the wind turbine is 34 m. The wind turbine has 3

blades with a rotor diameter of 2.9 m. The wind turbine has an upwind configuration, which means the blades are upwind of the tower. A 48 pole pair PMSG is simulated in Simulink to convert mechanical energy from the wind turbine into electric energy. The measured data includes stator current, output electric power, WTG shaft torque and shaft rotating speed.

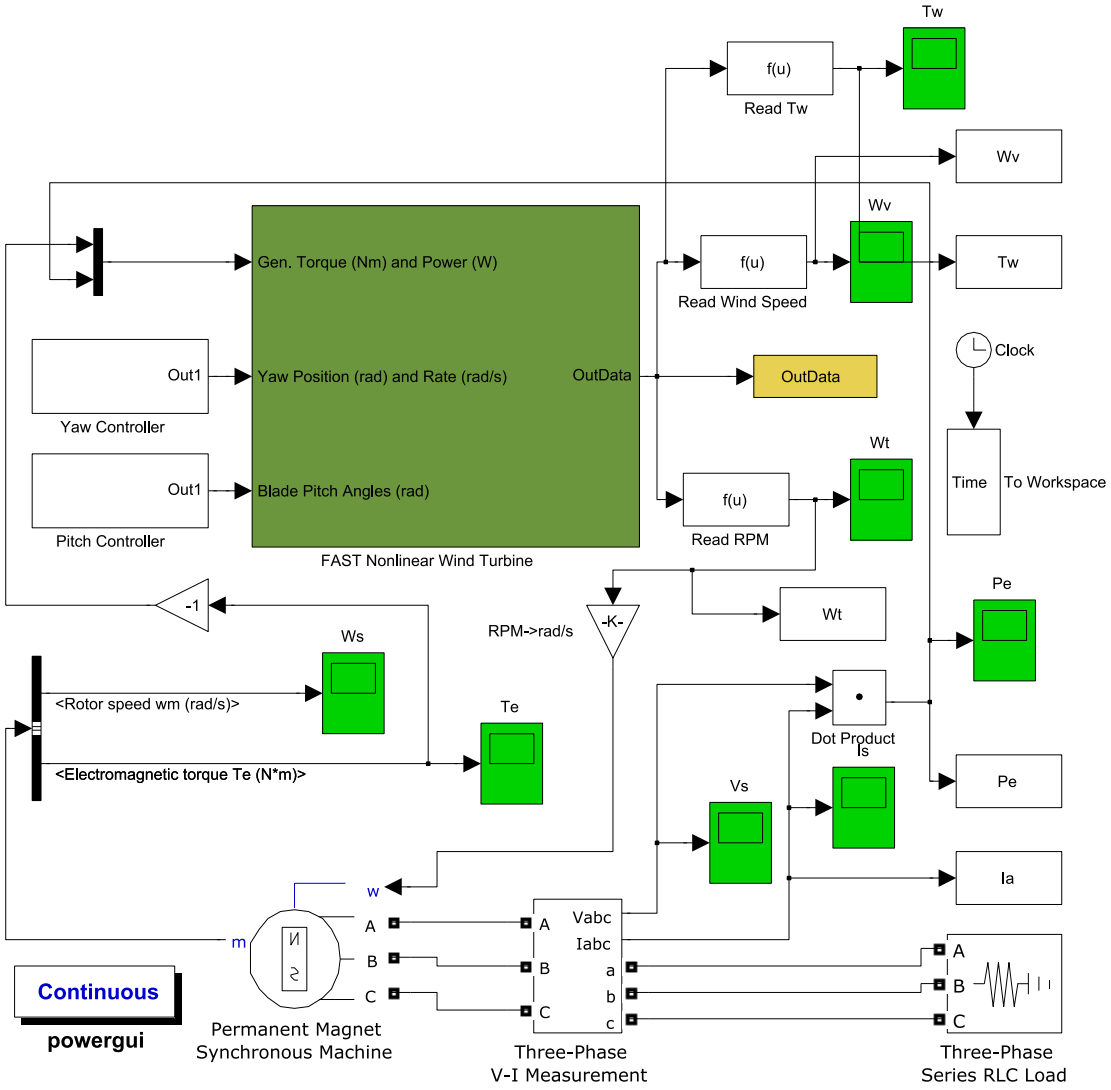

Figure 6.1: Model WTG in FAST/Simulink combined simulation platform.

6.1.2 Wind speed data

TurbSim is used in the simulation study to produce wind speed vectors in a time series across the entire rotating plane of the wind turbine's blades. The average wind speed is chosen to determine the strength of wind power. The International Electrotechnical Commission (IEC) Kaimal turbulence model is used to generate wind turbulence in all simulations [142]. The cross-section area (8m×8m) of the wind flow is divided into a 6×6 grid where the wind velocity and direction are calculated by TurbSim for each grid cell. The output of TurbSim contains a time series of wind speed, which is used for the aeroelastic simulation in FAST. The overall structure of the simulation platform is show in Fig. 6.2.

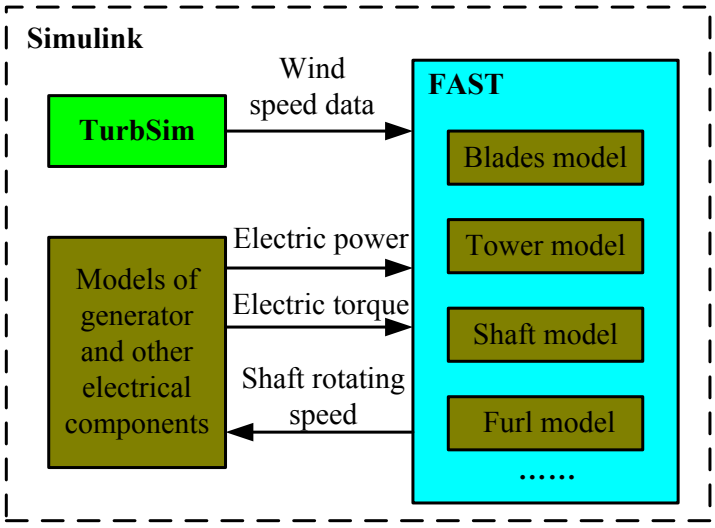

Figure 6.2: Structure of the WTG model with wind data in TurbSim/FAST/Simulink combined simulation platform.

6.1.3 Fault simulation

Some WTG faults, e.g., blade imbalance and aerodynamic asymmetry, can be emulated in model WTG for validating the proposed online nonintrusive condition monitoring and fault detection methods. The blade imbalance is simulated by changing the mass density of one blade, which creates an uneven distribution of mass of the blades with respect to the rotor. The aerodynamic asymmetry is simulated by adjusting the pitch angle of one blade, which creates an uneven torque across the rotor. Moreover, control errors of the yaw system can also be simulated in FAST. Files and parameters of FAST software used for simulating blade imbalance, aerodynamic asymmetry, and control errors of yaw system are listed in Table 6.2.

Table 6.2: Files and Parameters Used for WTG Fault Simulation

WTG fault	File name	Parameter
Blade imbalance	SWRT_Blade.dat	AdjBlMs
Aerodynamic asymmetry	Test17.fst	BlPitch
Control errors of yaw system	Test17.fst	NacYaw

6.1.4 Simulation results

A case study of the modeled WTG in the healthy condition is performed to test the PMSG wind turbine model. The information of wind speed, stator current of the PMSG, PMSG output power, turbine shaft torque, and shaft rotating speed are plotted below. The model WTG is operated in a variable-speed condition with an average wind speed of 16 m/s. In Figure 6.3, the wind speed varies from 12-21m/s. Figure 6.4 shows

that the amplitude of the current is 35 A in the maximum wind speed condition at 17 s of the simulation. As shown in Figure. 6.5, the output power of the PMSG is in the range of 7-14 kW, where the limitation of the maximum power generation of the PMSG is not modeled. The shaft rotating speed is in the range of 180-360 rpm.

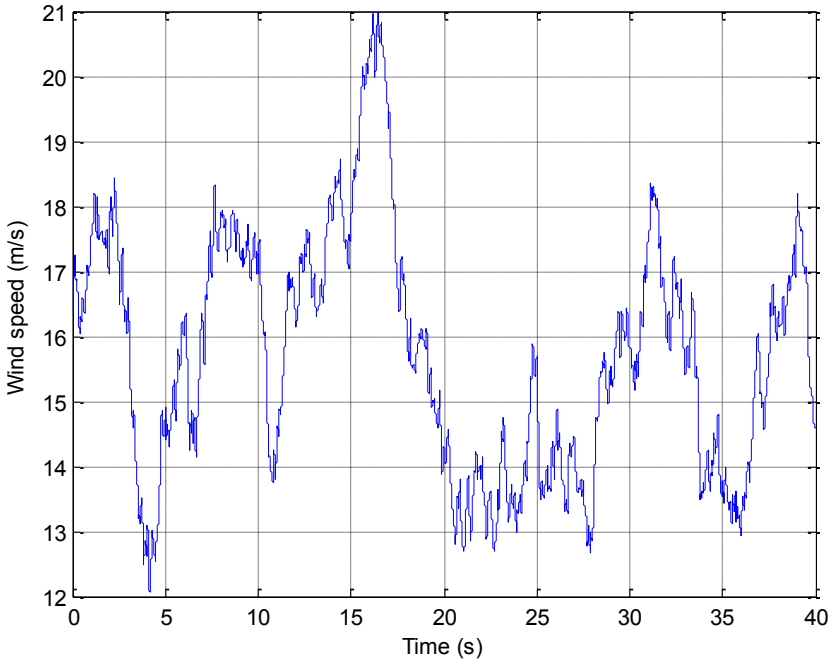

Figure 6.3: Wind speed in the simulation.

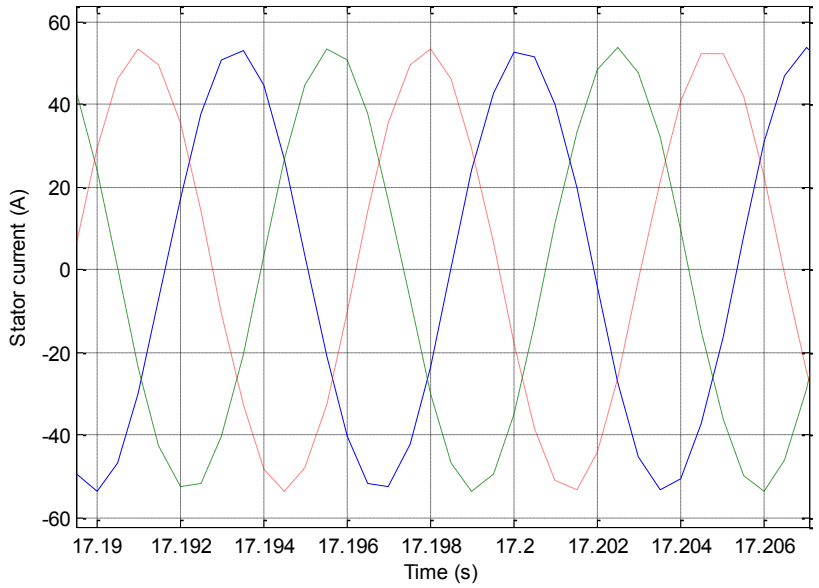

Figure 6.4: PMSG stator currents in the simulation.

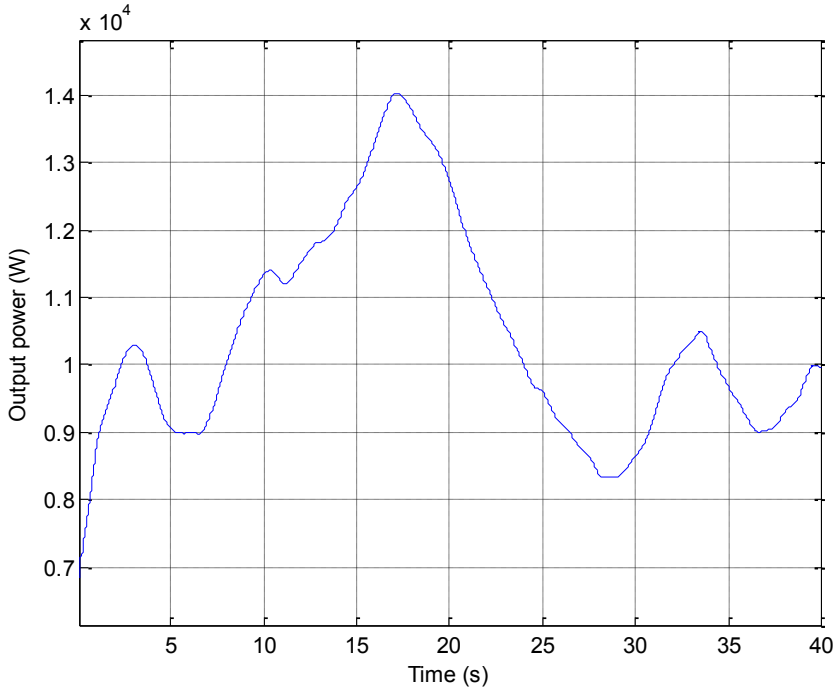

Figure 6.5: PMSG output power in the simulation.

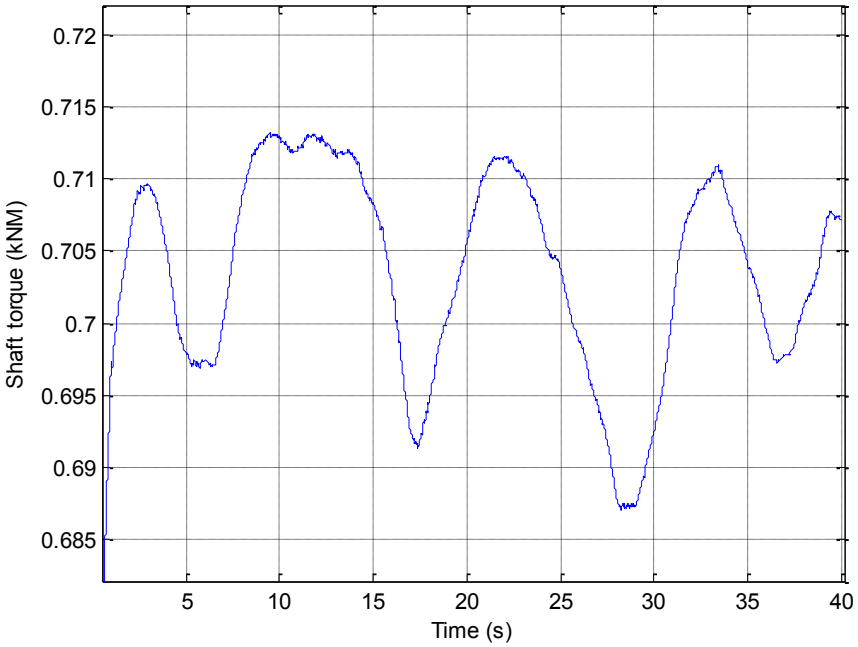

Figure 6.6: Shaft torque in the simulation.

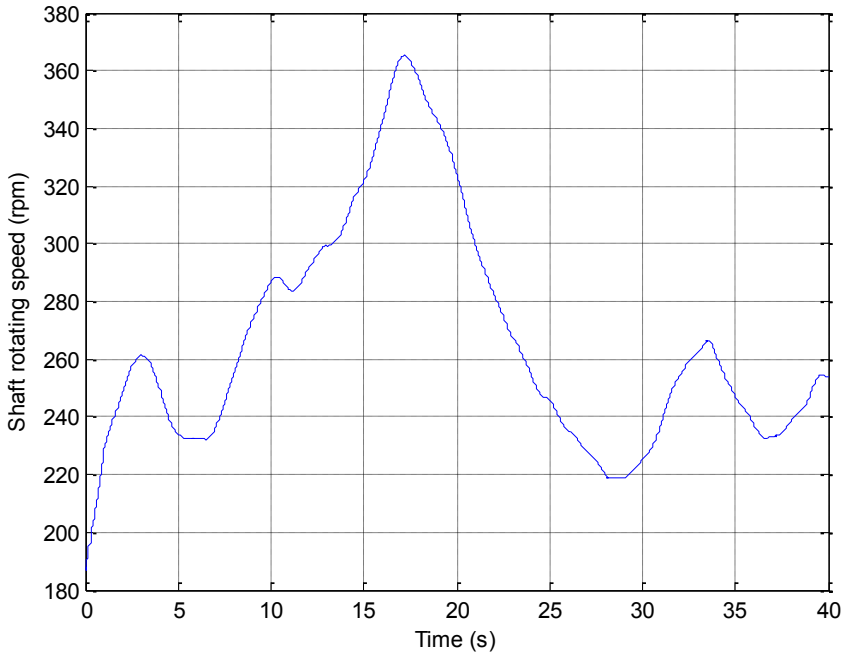

Figure 6.7: Shaft rotating speed in the simulation.

6.2 Experimental Setup

A wind tunnel was built for experimental verification of the proposed online nonintrusive WTG condition monitoring and fault detection methods using real WTGs. Wind tunnels are widely used in academia and industry [143], [144]. However, little work has been reported on using wind tunnels for research of wind turbine condition monitoring and fault detection. This section describes a wind tunnel-based experimental setup used in this research.

6.2.1 Wind tunnel and testing wind turbine

The six pole pairs, 160-W Southwest Windpower Air Breeze direct-drive PMSG wind turbines are used for experimental studies. The WTGs are operated in a wind tunnel with the dimensions of 2.5 meter × 2.5 meter × 6.5 meters in the UNL's Power & Energy systems Laboratory, as shown in Figure 6.8. The wind tunnel uses a 7-feet (diameter) variable-speed fan driven by a 60-hp adjustable-speed induction motor drive to generate controllable wind flows with the speed in the range from 0 to 10 m/s. Consequently, the testing WTGs can be operated in variable-speed conditions.

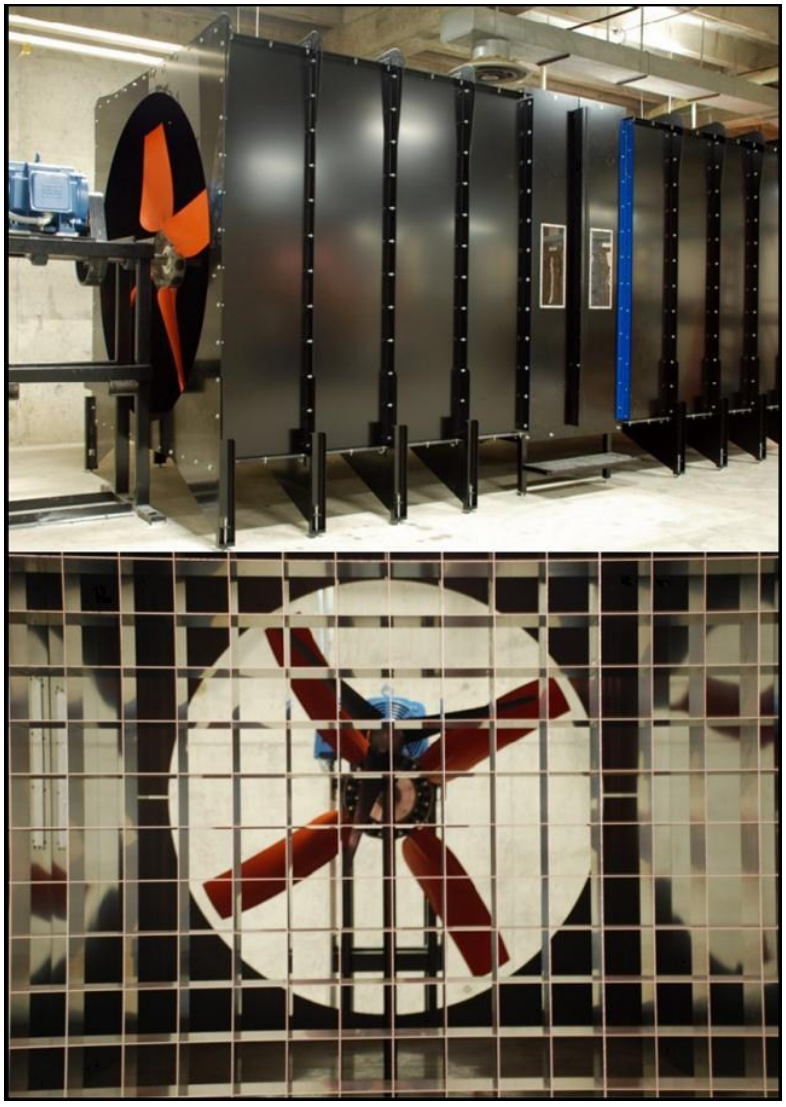

Figure 6.8: The wind tunnel with a testing WTG.

6.2.2 Sensing and data acquisition system

Figure 6.9 shows the sensing and data acquisition system used for the testing WTGs in the experiments. One phase stator current of the PMSG was recorded via a Fluke 80i-110s AC/DC current clamp. A general-purpose accelerometer (Wilcoxon-777B) was mounted on the testing WTG to measure its vibration. The amplitude of vibration in the horizontal direction of the nacelle of the testing WTG is much greater than that in the

vertical direction due to large stiffness in the vertical direction and small stiffness in the horizontal direction of the WTG nacelle [39]. Therefore, the accelerometer was mounted on the surface of the nacelle to detect the vibration in the horizontal direction of the wind turbine.

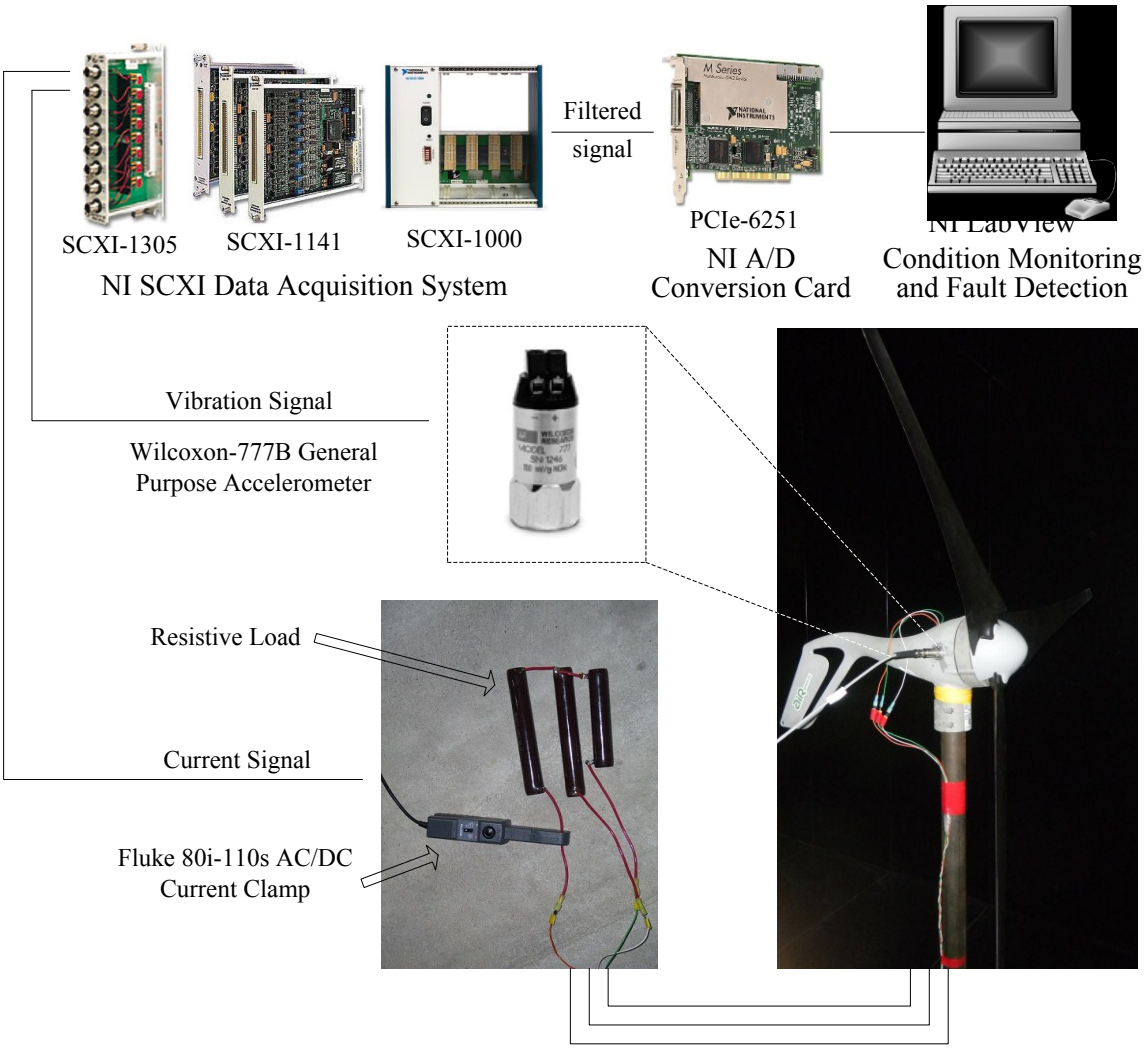

Figure 6.9: Sensing and data acquisition system for the testing WTG.

The measured vibration and current signals were digitalized by a National Instrument data acquisition system, where the SCXI-1141 card was used as an

antialiasing filter; the PCIe-6251 card is an A/D converter; the SCXI-1305 and SCXI-1000 are the interface and enclosure of the data acquisition system, respectively. The sampling rate of the vibration and current data was 10 kHz. The current and vibration samples were acquired by the LabView software operating in a lab computer. These samples were then used to verify the proposed online nonintrusive condition monitoring and fault detection methods.

6.2.3 Measured data

A case study of the testing WTG operating in variable-speed condition is performed. The acquired one phase stator current and vibration amplitude of the testing WTG are plotted in Figures 6.10 and 6.11, respectively. The figures show these quantities of the testing WTG in the healthy condition.

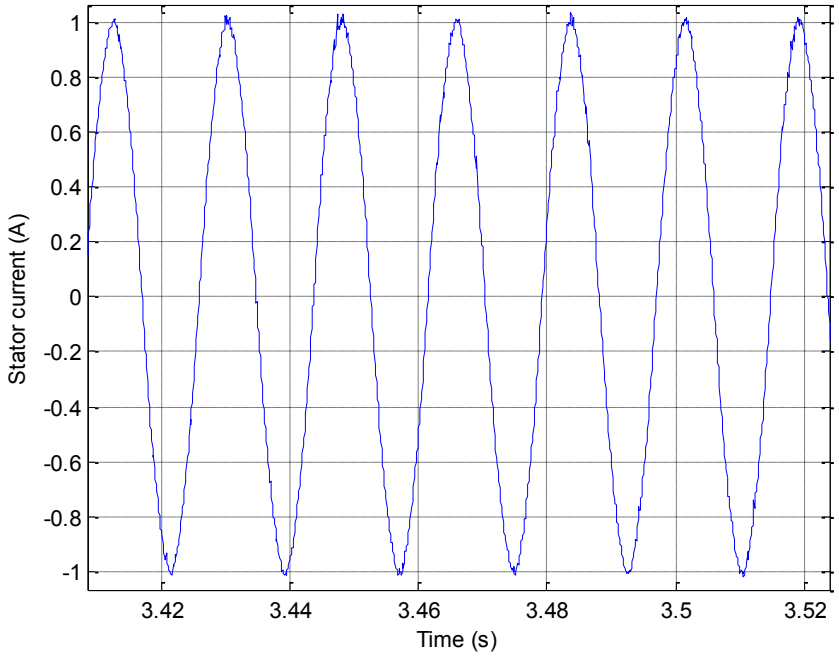

Figure 6.10: One phase stator current of the testing WTG.

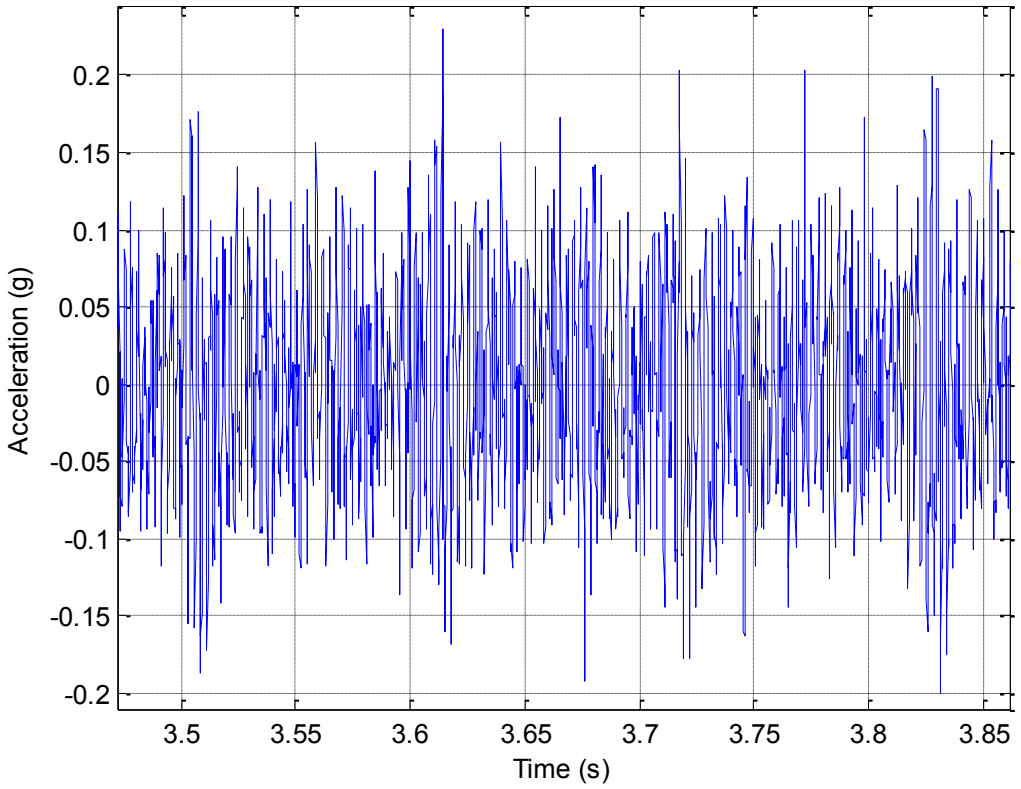

Figure 6.11: Vibration amplitude of the testing WTG.

Chapter 7 Simulation and Experimental Verification

Simulations and experiments have been performed to verify the proposed methods for online nonintrusive condition monitoring and fault detection of WTGs, which include the 1P-invariant PSD method, high-performance 1P-invariant PSD method, impulse detection method, wavelet-based filter method, and fault index evaluator.

7.1 Simulation Verification of 1P-Invariant PSD Method

The model WTG in Chapter 6 was used for simulation verification of the proposed 1P-invariant PSD method. Simulations were performed for the model WTG in the healthy condition (i.e., the baseline case) as well as in two WTG imbalance fault conditions: blade imbalance and aerodynamic asymmetry. One phase stator current of the WTG was recorded in the simulations. The proposed 1P-invariant PSD method was then applied to extract the signatures of the WTG faults by using the measured current signals in the frequency domain.

7.1.1 Blade imbalance fault

The mass density of one blade was scaled up and down in the simulations of blade imbalance. Four fault scenarios were simulated with the mass density of one blade adjusted by -1%, +2%, -3%, and +4%; while the mass densities of the other two blades were unchanged. Here the negative sign indicates a decrease of the mass density and the positive sign indicates an increase of the mass density. The sampling rate of the current measurements is 2 kHz. The proposed method was applied to calculate the 1P-invariant PSD of the stator current frequency demodulated signals for the baseline case and the

four blade imbalance scenarios. The base frequency was chosen to be 3 Hz (i.e., 180 rpm), the ratio M of up-sampling was 5, and the base value of the down-sampling step size L was 20. The variable characteristic frequency of 1P (from 2 to 4 Hz) of the blade imbalance faults in the current frequency demodulated signal was converted to the base frequency, which is a constant value of 3 Hz. The results are compared in Figures 7.1 and 7.2. The results clearly show that in the blade imbalance scenarios excitations are evident at 1P, which is fixed at 3 Hz by using the proposed 1P-invariant PSD method. The imbalance was caused by an eccentric mass rotating with a frequency of 1P. The stator current frequency demodulated signal was affected by the imbalance in blades and also vibrates with a frequency of 1P. Furthermore, Figures 7.2 shows that the magnitude of the excitation at the 1P frequency increases with the increase of the degree of blade imbalance. On the other hand, no excitation is observed at the 1P frequency in the PSD curve for the wind turbine with healthy blades.

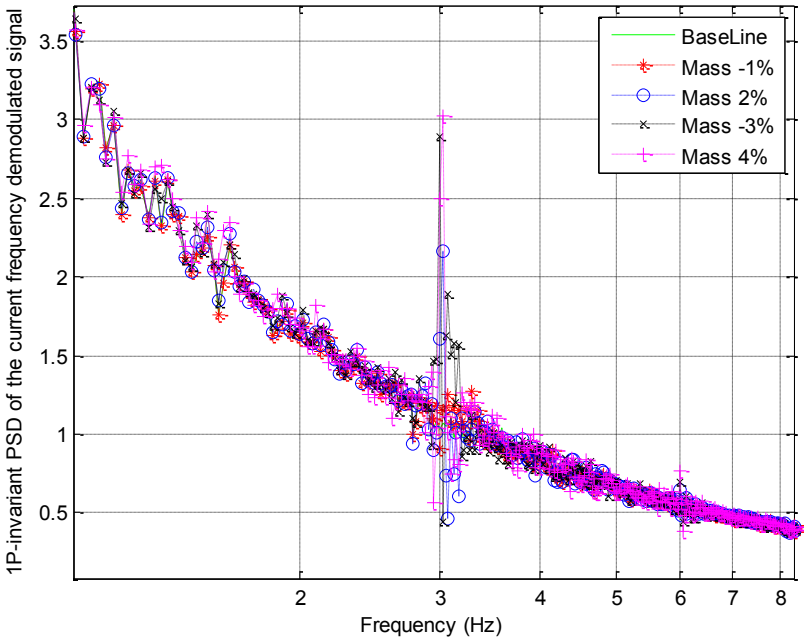

Figure 7.1: Comparison of the 1P-invariant PSD of the stator current frequency demodulated signals for the blade imbalance scenarios against the baseline case in a wide frequency range.

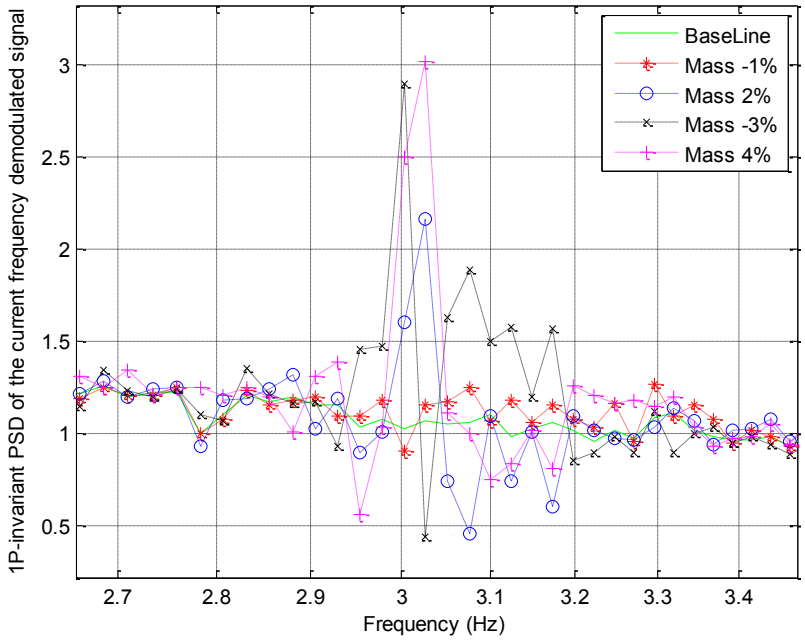

Figure 7.2: Comparison of the 1P-invariant PSD of the stator current frequency demodulated signals for the blade imbalance scenarios against the baseline case in a frequency range around 1P.

7.1.2 Aerodynamic asymmetry

In order to simulate aerodynamic asymmetry faults of the wind turbine, the pitch angle of one blade was adjusted by -2 degree, +4 degree, -6 degree, and +8 degree from the original pitch angle of 11.44 degree; while the pitch angles of the other two blades were unchanged at 11.44 degree. Figures 7.3, 7.4 and 7.5 compare the 1P-invariant PSD spectra of the stator current frequency demodulated signals generated by the proposed method for the wind turbine in the four aerodynamic asymmetry scenarios against the baseline case. Again, the variable 1P frequency of the WTG was converted to a constant value of 3 Hz by using the proposed method. Excitations appeared at both 1P and 2P frequencies in the four aerodynamic asymmetry scenarios, which agree with the theoretical analysis in Chapter 2. Moreover, the magnitudes of the excitations at the characteristic frequencies in the PSD plots become more significant when the degree of aerodynamic asymmetry becomes greater.

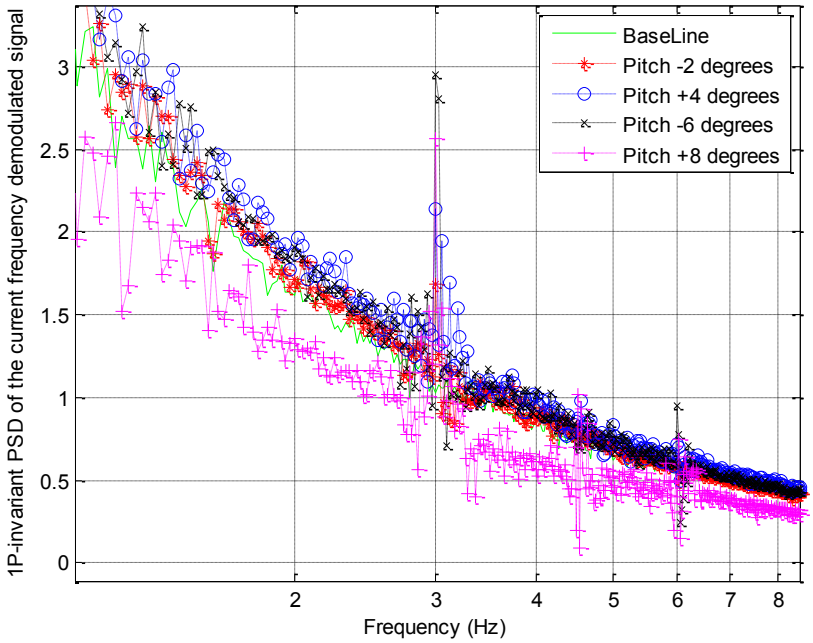

Figure 7.3: Comparison of the 1P-invariant PSD of the stator current frequency demodulated signals for the aerodynamic asymmetry scenarios against the baseline case in a wide frequency range.

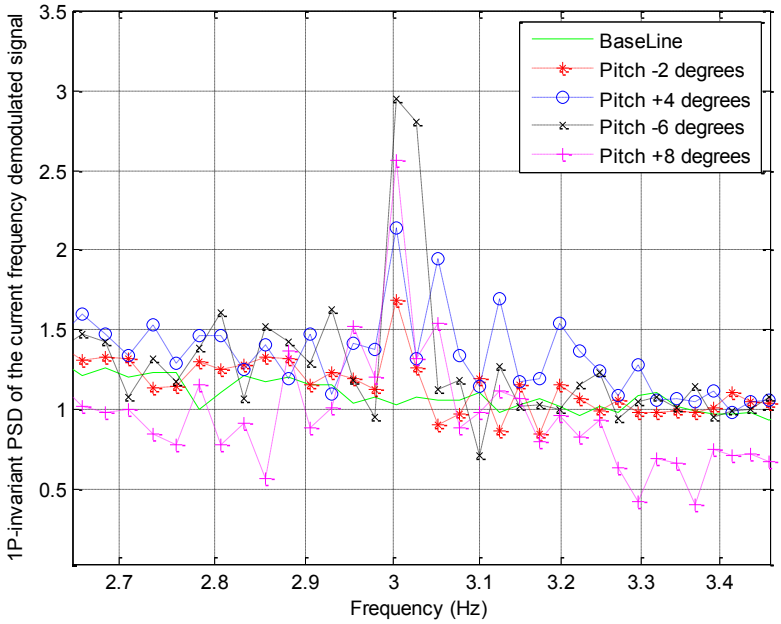

Figure 7.4: Comparison of the 1P-invariant PSD of the stator current frequency demodulated signals for the aerodynamic asymmetry scenarios against the baseline case in a frequency range around 1P.

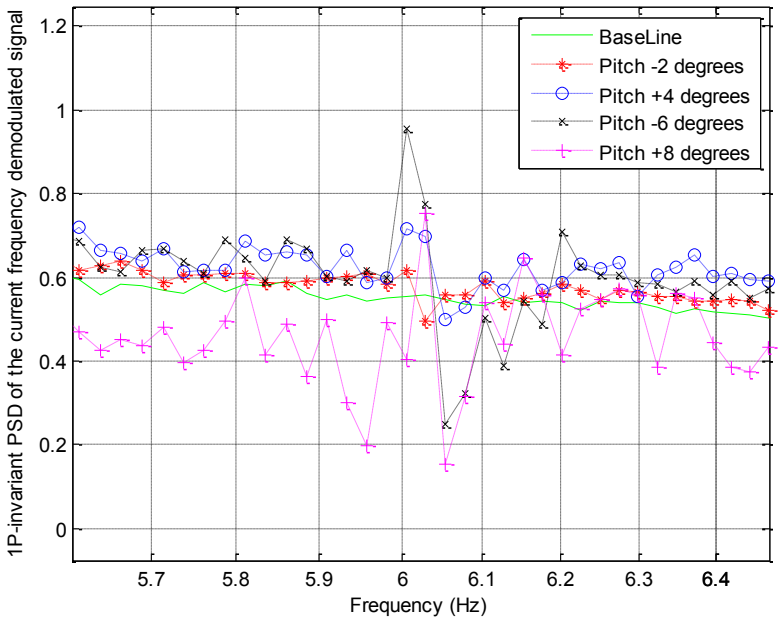

Figure 7.5: Comparison of the 1P-invariant PSD of the stator current frequency demodulated signals for the aerodynamic asymmetry scenarios against the baseline case in a frequency range around 2P.

7.2 Experimental Verification for 1P-Invariant PSD Method

The testing WTG, wind tunnel, and the data acquisition equipment presented in Chapter 6 were used for experimental verification of the proposed 1P-invariant PSD method. Experiments were performed for the testing WTG in the healthy condition (i.e., the baseline case) as well as in three WTG fault conditions: blade imbalance, blade damage and generator rotor fault. One phase stator current signal and acceleration (vibration) signal of the testing WTG were recorded in the experiments for fault detection. The proposed method was then applied to extract the signatures of the WTG faults in measured current and vibration data.

7.2.1 Blade imbalance fault

To create a blade imbalance, additional masses were added close to the tip of a blade of the testing WTG, as shown in Figure 7.6. The mass of a healthy blade was measured to be 181 g. Four blade imbalance scenarios were tested by adding a mass of 2 g, 4 g, 6 g, and 8 g, respectively, to a blade. Therefore, the weight of the blade was increased by approximately 1%, 2%, 3%, and 4%, respectively. During the experiments, the testing WTG was operated with a variable speed in the range of 6-13 Hz (360-780 rpm), which is the variable 1P frequency. The sampling rate of the current and vibration measurements is 10 kHz.

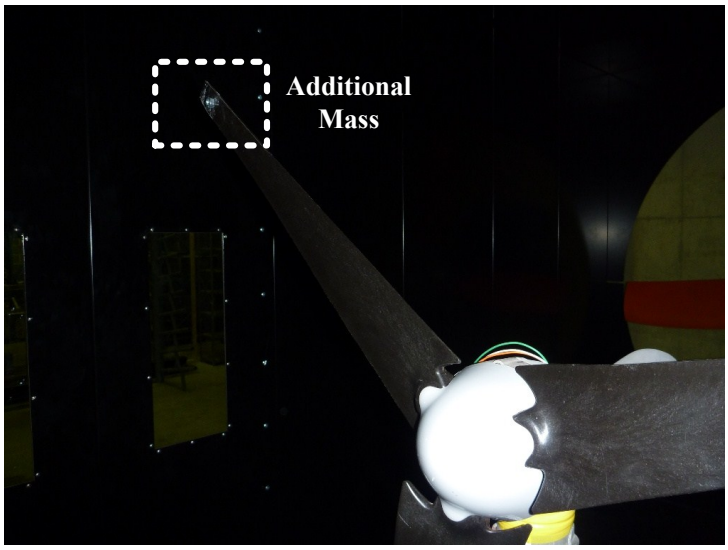

Figure 7.6: A blade with an additional mass to create a blade imbalance fault.

The proposed method was applied to obtain the 1P-invariant PSD spectra of the stator current frequency demodulated signals of the testing WTG for the four blade imbalance scenarios and the baseline case. In the proposed method, the base frequency f_b was chosen to be 10 Hz, the ratio M of up-sampling was 1 (i.e., no interpolation), and the

base value of the down-sampling step size L was 100. The results were compared in Figures 7.7 and 7.8, where excitations are clearly observed at the fixed 1P frequency of 10 Hz in the blade imbalance scenarios. Thus, the magnitude of this excitation provides an effective index for detecting blade imbalance faults. The greater the magnitude of the excitation appears at the 1P frequency, the higher degree the blade imbalance is. Therefore, the proposed method can not only identify but can also quantify the degree of blade imbalance of the WTG.

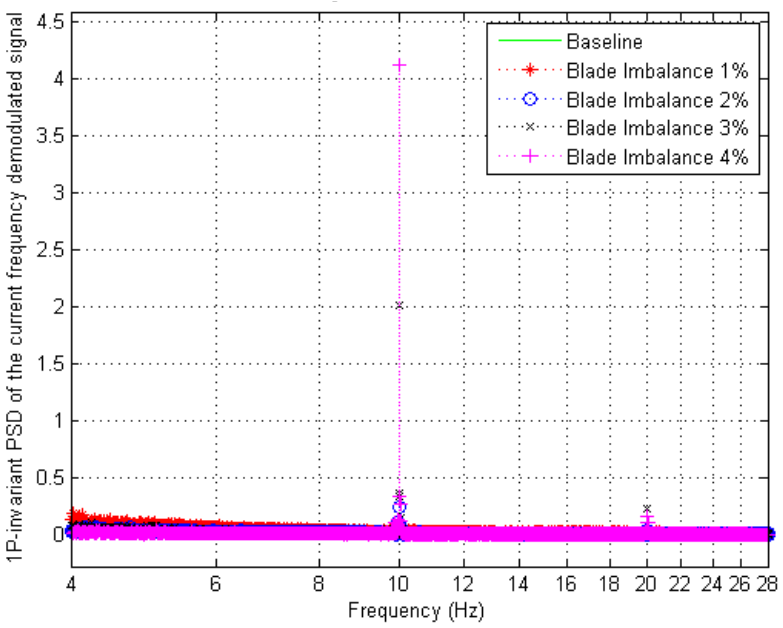

Figure 7.7: Comparison of the 1P-invariant PSD of the stator current frequency demodulated signals for the blade imbalance scenarios against the baseline case in a wide frequency range.

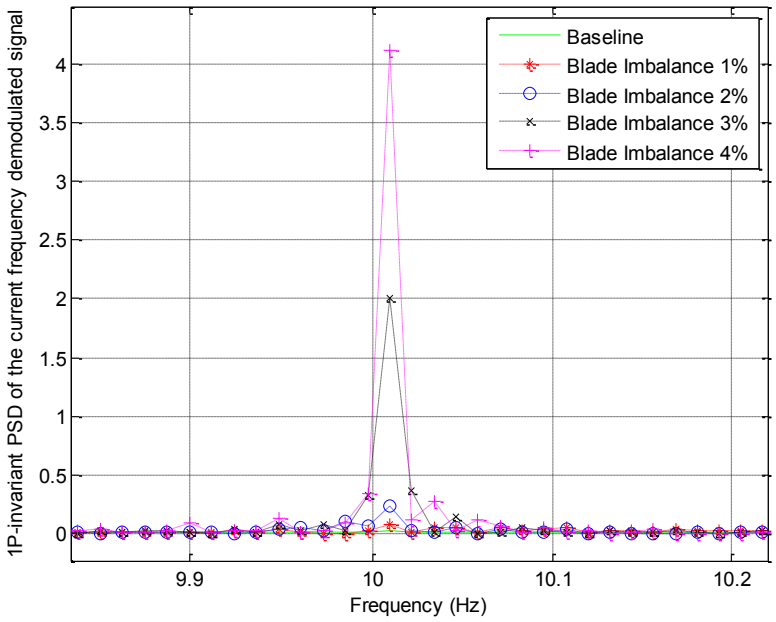

Figure 7.8: Comparison of the 1P-invariant PSD of the stator current frequency demodulated signals for the blade imbalance scenarios against the baseline case in a frequency range around 1P.

The PSD of the stator current frequency demodulated signals was also calculated by using the classical PSD analysis directly, i.e., without using the up-sampling and down-sampling algorithms in the proposed 1P-invariant PSD method. The results were compared in Figure 7.9 for the blade imbalance scenarios against the baseline case. The PSD of the stator current frequency demodulated signals excites at the 1P frequency in the range of 6-13 Hz in the blade imbalance scenarios. However, it is difficult to quantify and evaluate the blade imbalance faults by using these results due to the variations of the 1P frequency component. Furthermore, if interferences are present near the 1P frequency, it will be difficult to identify fault signatures from the interferences by using the classical PSD analysis.

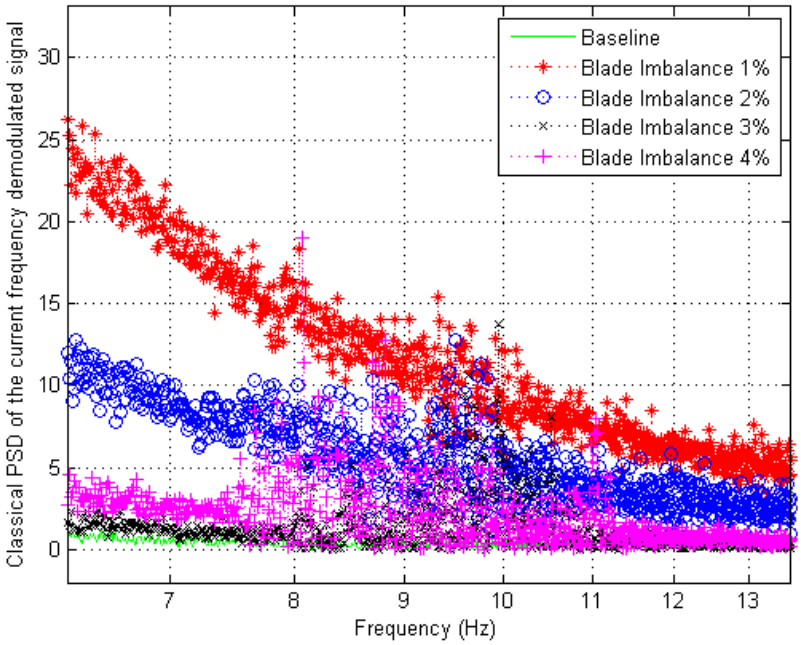

Figure 7.9: Comparison of the PSD of the stator current frequency demodulated signals obtained directly from the classical PSD analysis for the blade imbalance scenarios against the baseline case.

Since vibration signals are widely used for condition monitoring and fault detection of WTGs [23], the measured acceleration (vibration) data of the testing WTG were also used for the blade imbalance fault detection. Firstly, the root mean square (RMS) values of the vibration measurements were calculated for the four blade imbalance scenarios and the baseline case, as shown in Figure 7.10. The RMS values of the vibration measurements increase with the increasing degree of blade imbalance. Therefore, the WTG blade imbalance fault was successfully detected by using the vibration measurements. Moreover, the proposed method was applied to obtain the 1P-invariant PSD of the vibration measurements of the WTG in each scenario. The results were given in Figure 7.11 and 7.12. Excitations at the characteristic frequency of 10 Hz are found in the PSD plots of the WTG blade imbalance fault scenarios. Same as the 1P-

invariant PSD of the current frequency demodulation signals, the greater the magnitude of the excitation appears at the 1P frequency, the higher degree the blade imbalance fault is. Therefore, by using the proposed 1P-invariant PSD method, the current measurement-based WTG fault detection achieved similar results as the vibration measurement-based fault detection.

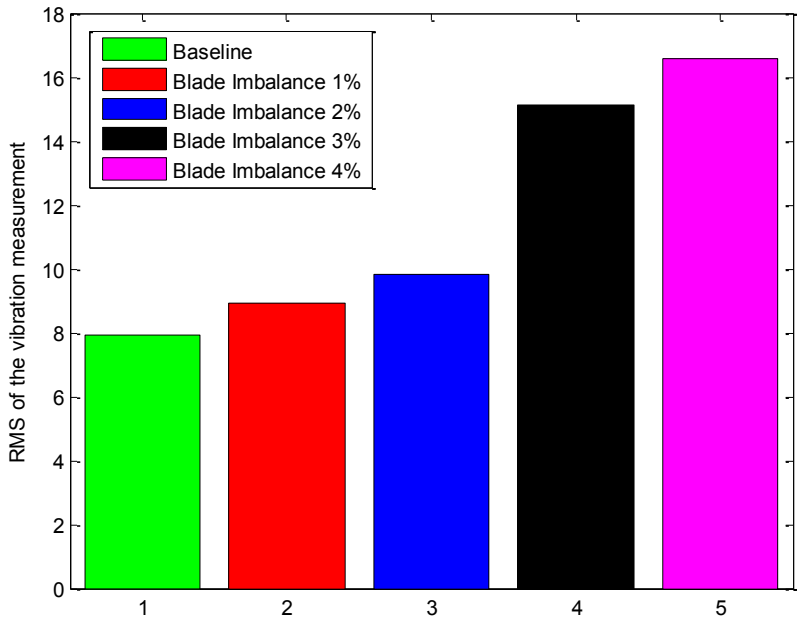

Figure 7.10: The RMS values of the WTG vibration measurements for the blade imbalance scenarios against the baseline case.

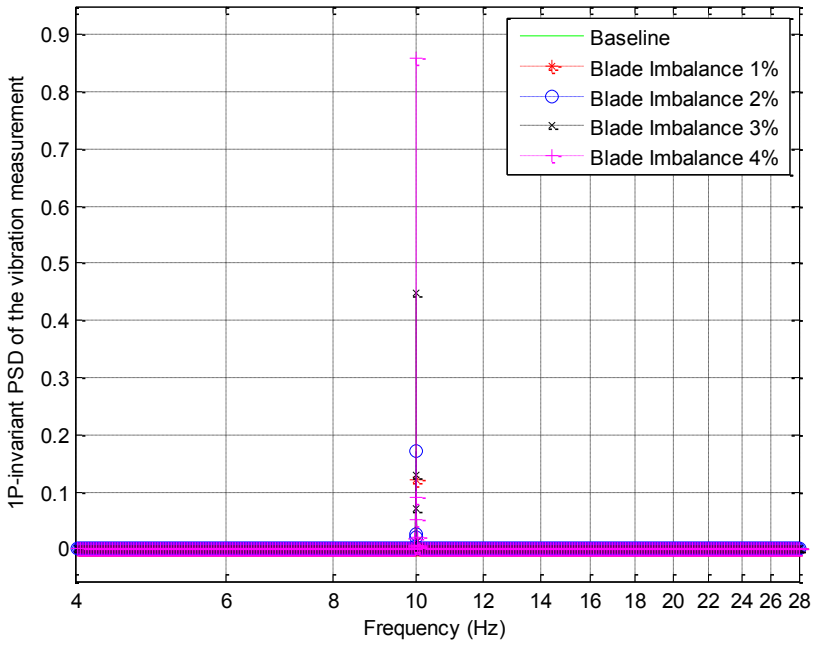

Figure 7.11: Comparison of the 1P-invariant PSD of the WTG vibration measurements for the blade imbalance scenarios against the baseline case in a wide frequency range.

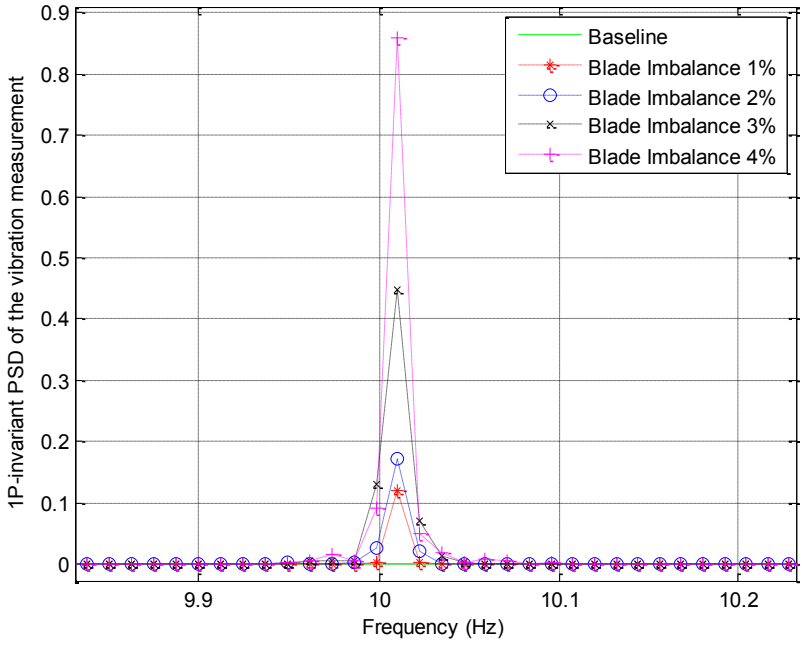

Figure 7.12: Comparison of the 1P-invariant PSD of the WTG vibration measurements for the blade imbalance scenarios against the baseline case in a frequency range around 1P.

7.2.2 Blade with defects

A blade with defects can generate an imbalance fault in the testing WTG. A blade with two-point defects and a blade with four-point defects were created, as shown in Figure 7.13. During the experiments, the WTG was operated with a variable speed in the range of 6-13 Hz. The sampling rate of the current measurements is 10 kHz.

Figure 7.13: Two defected blades used for experiments.

Figures 7.14 and 7.15 compare the 1P-invariant PSD of the stator current frequency demodulated signals of the WTG for the blade defect scenarios against the baseline case. The 1P-invariant PSD was obtained by using the proposed method with the same base frequency f_b and base value of the down-sampling step size L as in the blade imbalance study. As shown in Figures 7.14 and 7.15, an excitation appears at a fixed frequency of 1P (10 Hz) in the PSD plots of the blade defect cases. The magnitude of the 1P excitation provides an effective index for detecting and quantifying the defects on the blade. Similar to the WTG blade imbalance detection, the vibration measurements of the testing WTG were also used for detection of defects on the blade for comparison purpose,

as shown in Figures 7.16 and 7.17. The 10 Hz excitation appears in the PSD plots of the blade defect cases when using vibration measurements as well.

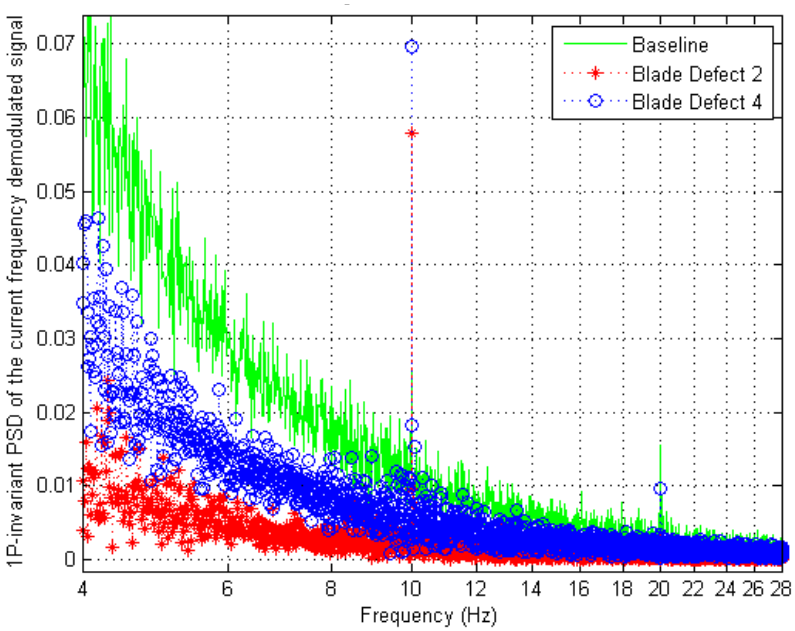

Figure 7.14: Comparison of the 1P-invariant PSD of the stator current frequency demodulated signals for the blade defect scenarios against the baseline case in a wide frequency range.

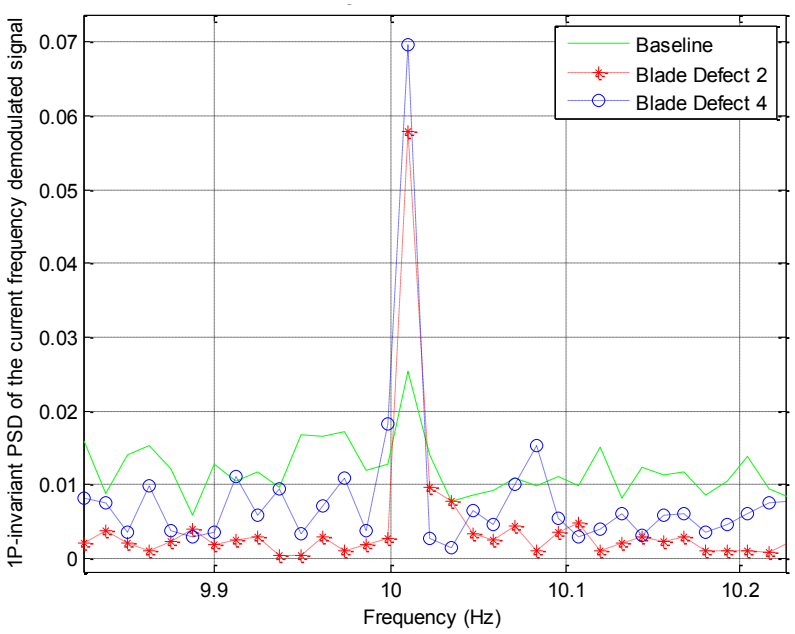

Figure 7.15: Comparison of the 1P-invariant PSD of the stator current frequency demodulated signals for the blade defect scenarios against the baseline case in a frequency range around 1P.

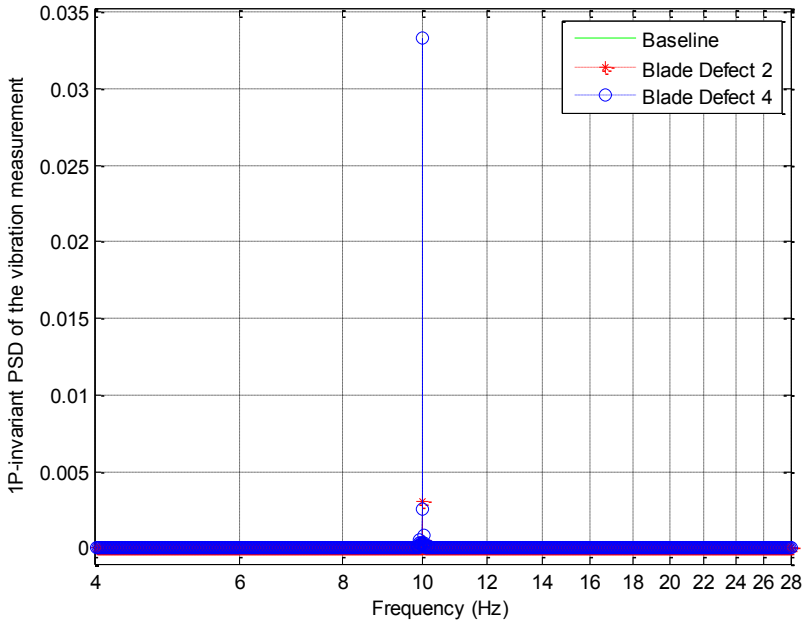

Figure 7.16: Comparison of the 1P-invariant PSD of the WTG vibration measurements for the blade defect scenarios against the baseline case in a wide frequency range.

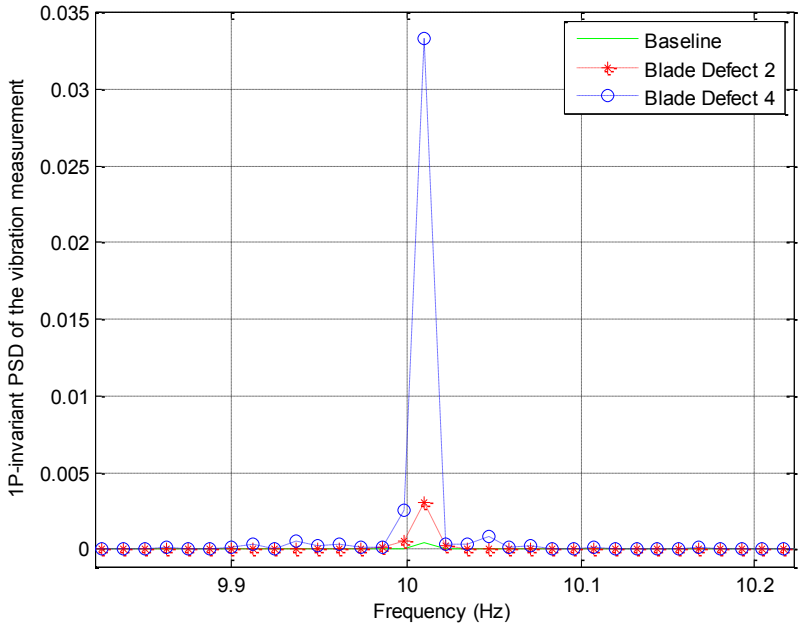

Figure 7.17: Comparison of the 1P-invariant PSD of the WTG vibration measurements for the blade defect scenarios against the baseline case in a frequency range around 1P.

7.2.3 Rotor fault

To emulate a rotor fault in the WTG, two magnets with different magnetic field intensities were added to the generator rotor of the Air Breeze wind turbine separately, as shown in Figure 7.18. The added magnets generated a WTG fault with uneven magnetic field around the generator rotor and decrease the efficiency of the WTG. The WTG was operated with a variable speed in the range of 6-13 Hz in this experiment. The sampling rate of the current measurements is 10 kHz.

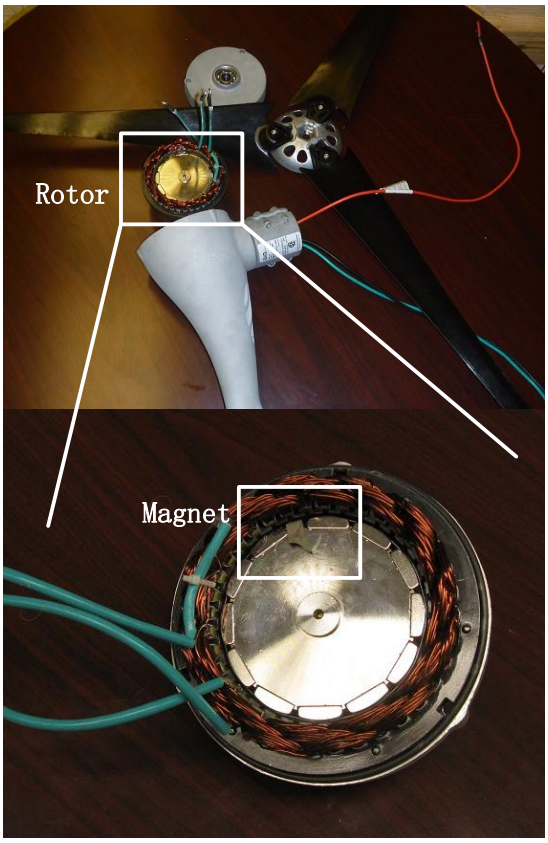

Figure 7.18: A generator rotor with an additional magnet in the testing WTG.

To detect the WTG rotor fault, the proposed method was applied to obtain the 1P-invariant PSD of the stator current frequency demodulated signals of the WTG for the two rotor fault scenarios and the baseline case. The results were plotted in Figures 7.19 and 7.20, where excitations at the fixed 1P frequency of 10 Hz are clearly observed in the rotor fault scenarios. Thus, the magnitude of this excitation provides an effective signature for detecting the rotor faults. As a comparison, the 1P-invariant PSD of the vibration signals are compared in Figures 7.21 and 7.22. Excitations at the fixed 1P frequency of 10 Hz are also clearly observed in Figures 7.21 and 7.22.

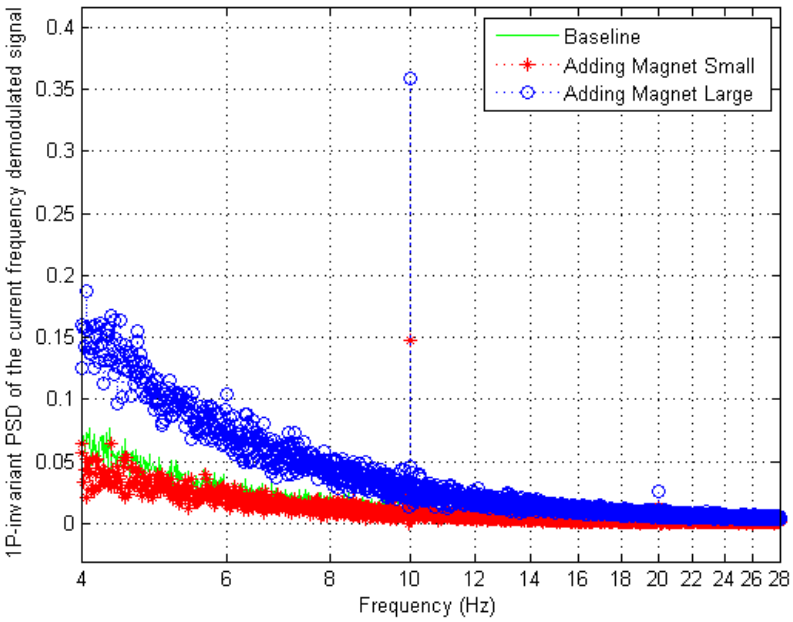

Figure 7.19: Comparison of the 1P-invariant PSD of the stator current frequency demodulated signals for the rotor fault scenarios against the baseline case in a wide frequency range.

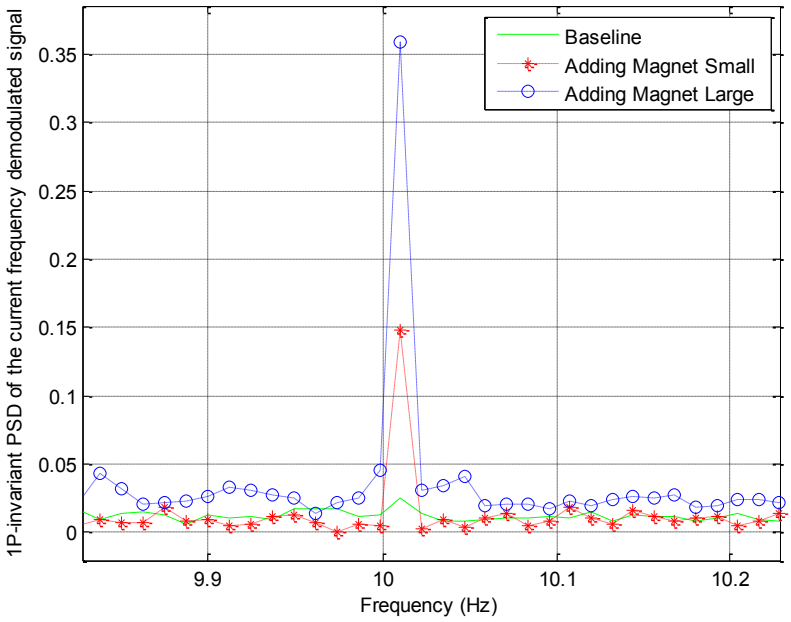

Figure 7.20: Comparison of the 1P-invariant PSD of the stator current frequency demodulated signals for the rotor fault scenarios against the baseline case in a frequency range around 1P.

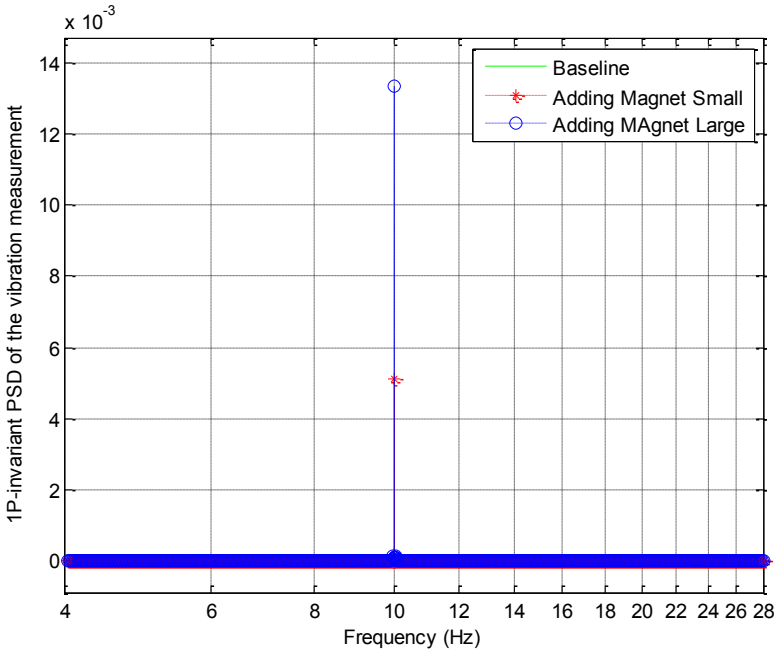

Figure 7.21: Comparison of the 1P-invariant PSD of the WTG vibration measurements for the rotor fault scenarios against the baseline case in a wide frequency range.

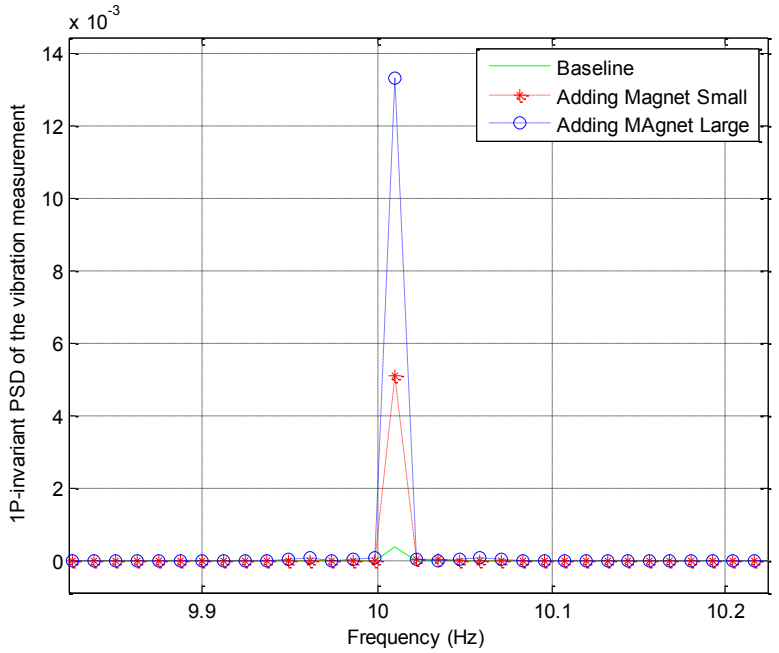

Figure 7.22: Comparison of the 1P-invariant PSD of the WTG vibration measurements for the rotor fault scenarios against the baseline case in a frequency range around 1P.

7.3 Experimental Verification for High-Performance 1P-Invariant PSD and Impulse Detection Method

The testing WTG, wind tunnel, and the data acquisition equipment in Chapter 6 were also used for experimental verification of the proposed high-performance 1P-invariant PSD method and impulse detection method. Experiments were performed for the testing WTG in the healthy condition (i.e., the baseline case) as well as in two WTG fault conditions: bearing outer-race fault and bearing cage fault. One phase stator current signal and acceleration (vibration) signal of the testing WTG were sampled in the experiments for faults detection. The proposed methods were then applied to detect the WTG faults by using the measured current data. The vibration data were processed by the proposed high-performance 1P-invariant PSD method for comparison purpose.

7.3.1 Bearing outer-race fault

A bearing outer-race fault was generated artificially in a testing bearing, as illustrated in Figure 7.23. The healthy bearing and the bearing with an outer-race fault were installed in the testing WTG, respectively. The length of the stator current record in each case was 50 seconds. The WTG was operated with a variable speed in the range of 6-13 Hz in this experiment. The sampling rate of the current measurements is 10 kHz.

Figure 7.23: Testing bearing with an outer-race fault.

Figure 7.24 compares the high-performance 1P-invariant PSD of the current amplitude demodulated signals for the testing WTG with an outer-race bearing fault against that with a healthy bearing, where in the high-performance 1P-invariant PSD the variable 1P frequency of 6-13 Hz was converted to a constant value of 10 Hz. As shown in Figure 7.24, an excitation appears at a fixed frequency of 30.8 Hz in the PSD plot of the bearing outer-race fault case. This fault characteristic frequency is the same as one calculated from (2.5) for the WTG operating with a fixed shaft rotating frequency of 10 Hz. Therefore, the excitation at 30.8 Hz in the high-performance 1P-invariant PSD spectrum of the current amplitude demodulated signal is an effective signature for the bearing outer-race fault diagnosis. The high-performance 1P-invariant PSD of the vibration signals are compared in Figure 7.25. An excitation is also observed at a fixed frequency of 30.8 Hz for the bearing outer-race fault case.

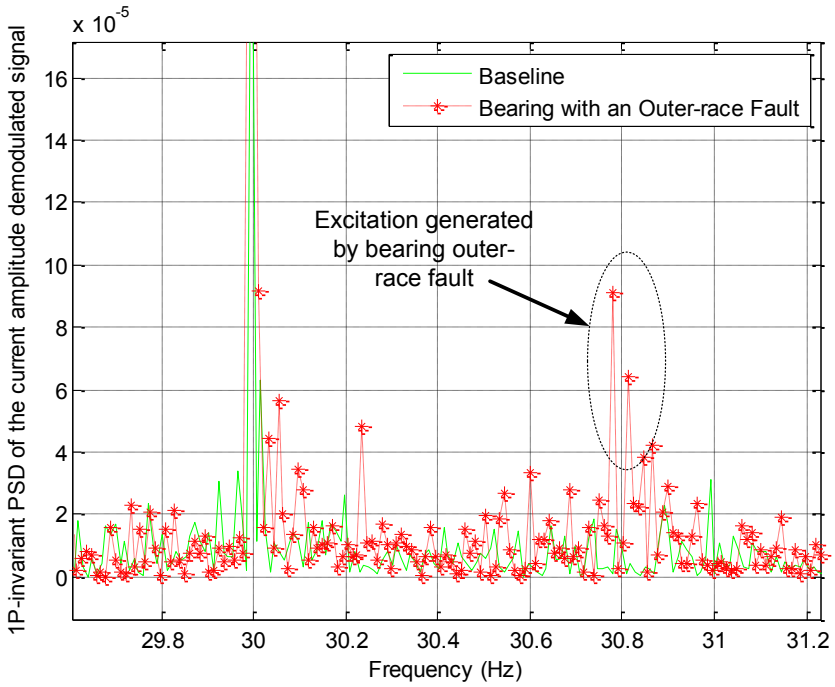

Figure 7.24: Comparison of the high-performance 1P-invariant PSDs of the current amplitude demodulated signals for the WTG with a bearing outer-race fault against that with a healthy bearing.

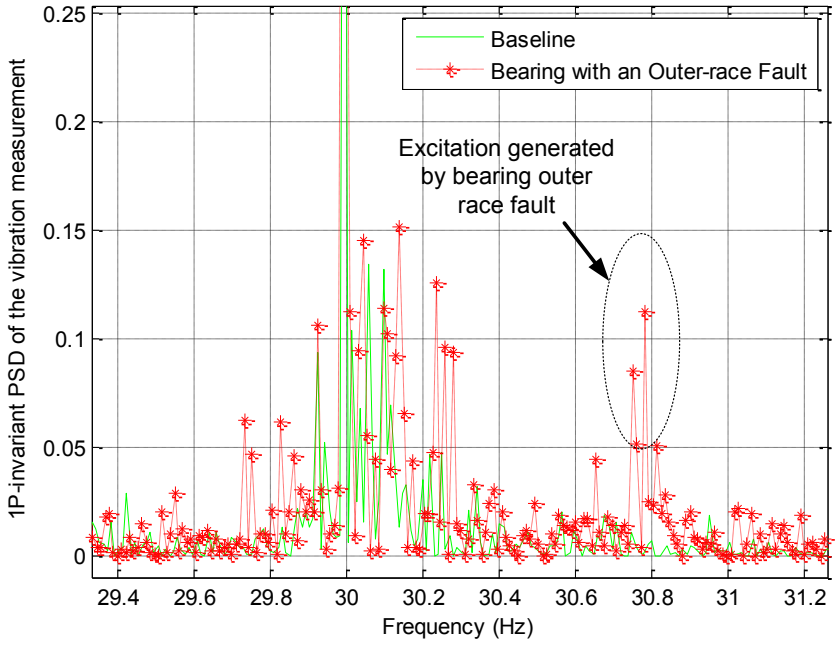

Figure 7.25: Comparison of the high-performance 1P-invariant PSDs of the vibration measurements for the WTG with a bearing outer-race fault against that with a healthy bearing.

The experimental result in Figure 7.24 for outer-race bearing fault detection was further analyzed by the proposed impulse detection method. As shown in Figure 7.26, the proposed impulse detection method was successfully applied to extract the excitations in the 1P-invariant PSD for bearing outer-race fault detection. The length of the window, W_w, was chosen to be 101. A third-order median filter was used to calculate the threshold. The locally normalized PSD [i.e., $R(f)$] of the bearing outer-race fault case is plotted in Figure 7.26, where the threshold was calculated to be 0.054. Figure 7.26 clearly shows that the proposed impulse detection method successfully found the excitation at 30.8 Hz corresponding to the bearing out-race fault.

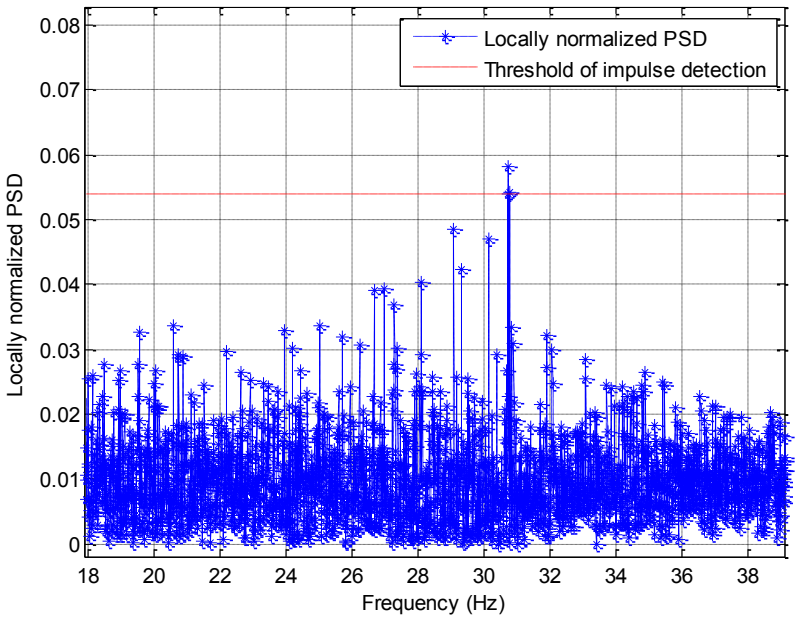

Figure 7.26: Locally normalized PSD and threshold generated by the impulse detection method for bearing outer-race fault detection.

7.3.2 Bearing cage fault

As illustrated in Figure 7.27, a bearing cage fault was generated artificially for a testing bearing. One clinch bolt of the bearing cage was broken. The healthy bearing and the bearing with the cage fault were installed in the testing WTG, respectively. The length of the stator current record in each case was 50 seconds. The WTG was operated with a variable speed in the range of 6-13 Hz in this experiment. The sampling rate of the current measurements is 10 kHz.

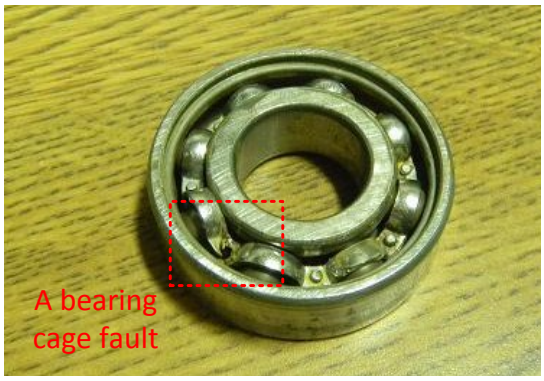

Figure 7.27: Testing bearing with a cage fault.

The high-performance 1P-invariant PSD of the current amplitude demodulated signals for the WTG with a healthy bearing and a cage faulted bearing are compared in Figure 7.28, where the variable 1P frequency in the range of 6 to 13 Hz was converted to a constant value of 10 Hz. As shown in Figure 7.28, an excitation appears in the PSD of the current amplitude demodulated signal at a fixed frequency of 3.85 Hz in the bearing cage fault case. This fault characteristic frequency is the same as one calculated from (2.6) for the WTG operating with a constant shaft rotating frequency of 10 Hz. Thus, the

excitation at 3.85 Hz in the high-performance 1P-invariant PSD of the current amplitude demodulated signal is an effective signature for bearing cage fault detection. Similar to the WTG bearing outer-race fault detection, the vibration measurements of the testing WTG were also used for detection of the bearing cage fault, as shown in Figure 7.29. The excitation at 3.85 Hz can be clearly identified in the high-performance 1P-invariant PSD of the vibration signal as well.

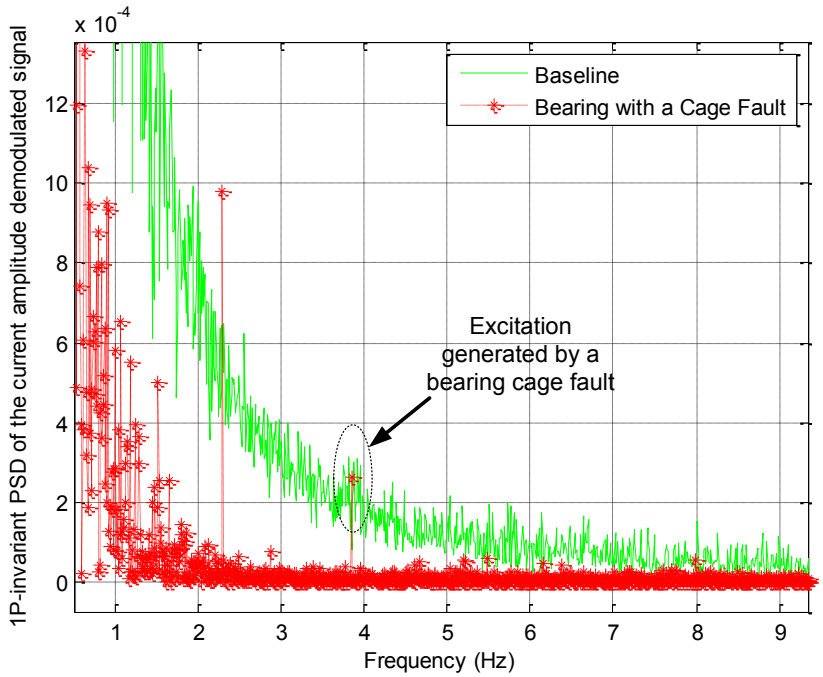

Figure 7.28: Comparison of the high-performance 1P-invariant PSDs of the current amplitude demodulated signals for the WTG with a bearing cage fault against that with a healthy bearing.

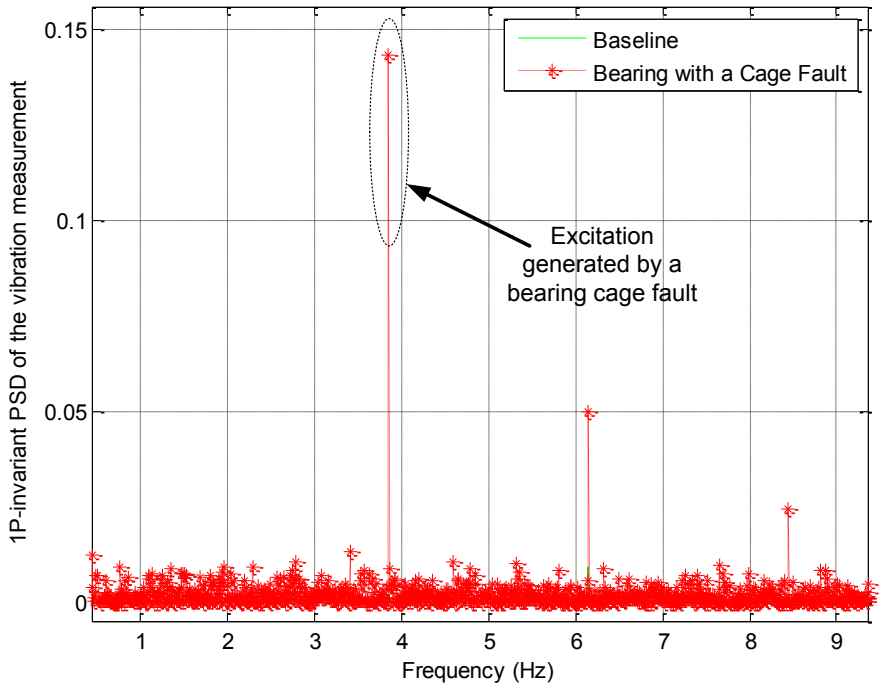

Figure 7.29: Comparison of the high-performance 1P-invariant PSDs of the vibration measurements for the WTG with a bearing cage fault against that with a healthy bearing.

Another bearing cage fault was generated in the testing bearing for experiment verification of the high-performance 1P-invariant PSD method and the impulse detection method. To accelerate the degradation of the testing bearing, it was pretreated by wiping off the lubrication oil. The WTG was operated continuously in the wind tunnel with a variable speed in the range of 10-13 Hz for approximately 25 hours. The WTG stator current signal was recorded every 20 minutes. The length of each record was 50 seconds. The sampling rate of the current measurements is 10 kHz. The wind turbine stopped rotating at the end of the experiment due to the damage of the bearing cage. Figure 7.30 illustrates the bearing before and after the experiment.

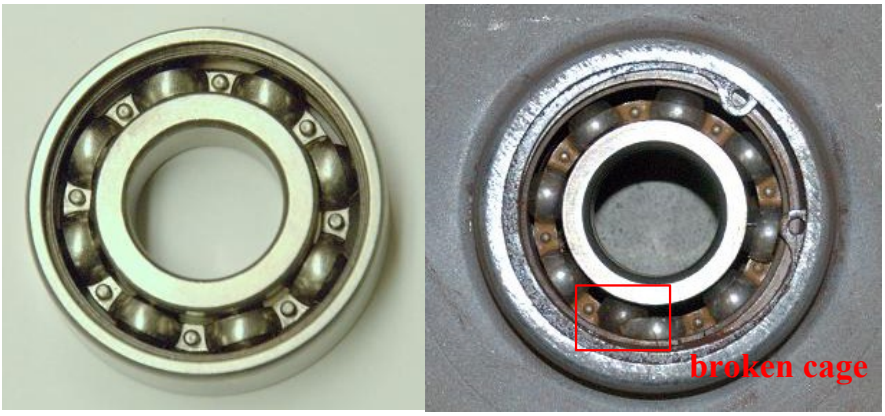

Figure 7.30: Testing bearing before and after the experiment.

By using the high-performance 1P-invariant PSD method, the PSD of the current frequency demodulated signals for the healthy bearing case and the bearing cage fault case are compared in Figure 7.31, where the variable 1P frequency in the range of 6-13 Hz was converted to a constant value of 10 Hz. As shown in Figure 7.31, an excitation appears in the 1P-invariant PSD of the current frequency demodulated signal at a fixed frequency of 4 Hz in the bearing cage fault case.

The proposed impulse detection method was applied to extract the excitations in the 1P-invariant PSD for bearing cage fault detection. The length of the window, W_w, was chosen to be 101. A third-order median filter was designed for threshold calculation. The locally normalized PSD [i.e., $R(f)$] of the last record (bearing with cage fault) is plotted in Figure 7.32. The threshold was calculated to be 0.11. The impulses appear at 4 Hz and 8 Hz, where the impulse at 4 Hz indicates the signature of a bearing cage fault; the impulse at 8 Hz is the second-order harmonic of the excitation generated by bearing cage fault.

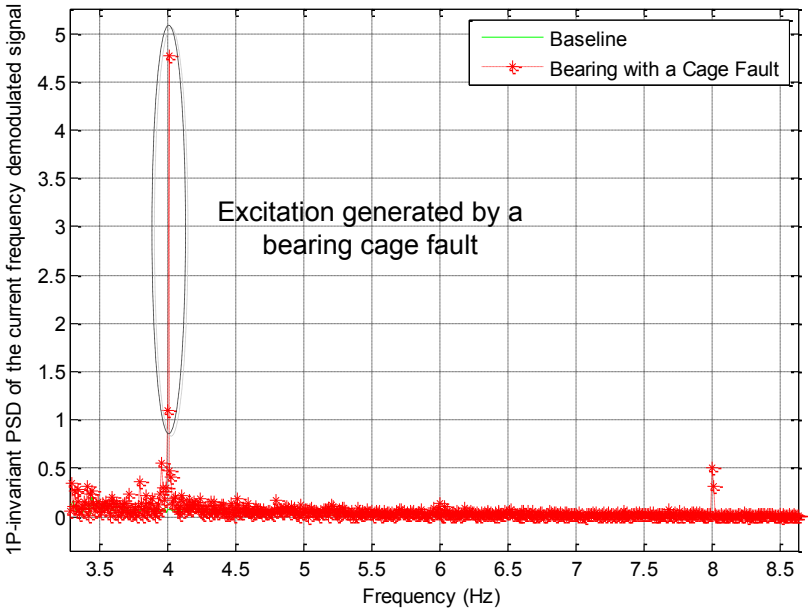

Figure 7.31: Comparison of the high-performance 1P-invariant PSDs of the current frequency demodulated signals for the WTG with a bearing cage fault against that with a healthy bearing.

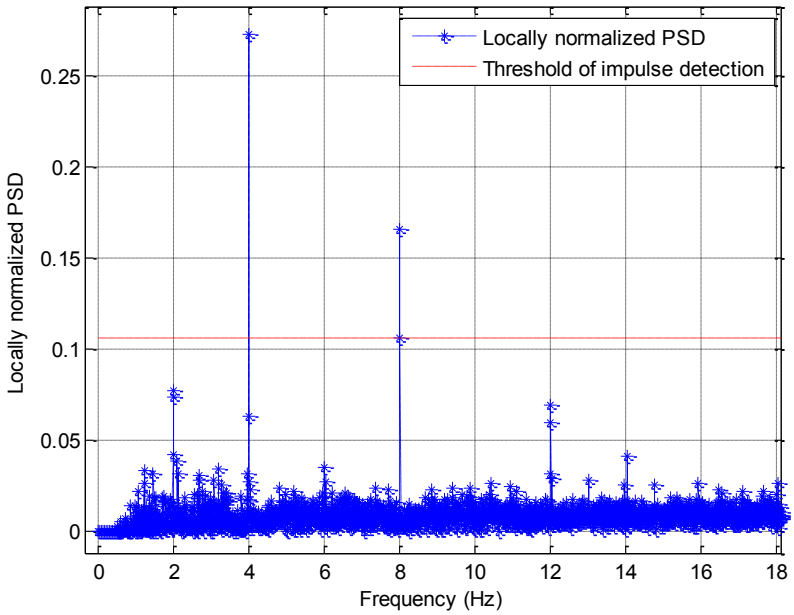

Figure 7.32: Locally normalized PSD and threshold generated by the impulse detection method for bearing cage fault case.

The proposed impulse detection method was also applied to determine whether there is a signature of the bearing cage fault in the 1P-invariant PSD of the current frequency demodulated signal during the entire 25-hour experiment. The result is given in Figure 7.33. It shows that the signature of the bearing cage fault appears from the 6th hour onwards of the experiment. The fault signature indicates a degradation of the bearing cage and maintenance should be taken immediately. Since there was no maintenance taken after the 6th hour of the experiment, the bearing was damaged and the testing WTG was stopped at the 25th hour of the experiment by the protection system.

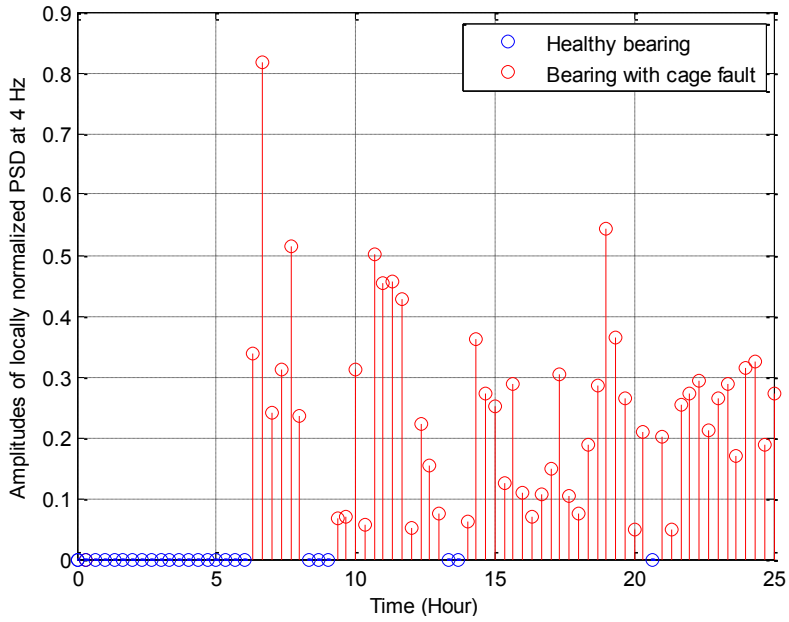

Figure 7.33: Amplitudes of the locally normalized PSDs at the bearing cage fault characteristic frequency of 4 Hz during the 25-hour experiment.

7.4 Benefits of Using Current Demodulated Signals

To illustrate the advantage of using the current demodulated signals for online nonintrusive condition monitoring and fault detection of WTGs, the 1P-invariant PSD of

the raw current measurement for the second bearing cage fault case in Section 7.3.2 is plotted in Figure 7.34. The variable WTG shaft rotating frequency was converted to a constant value of 10 Hz by using the 1P-invariant PSD method. Based on Table 4.1, (2.7), and the six pole pairs of the testing WTG, the excitations due to the bearing cage fault should appear at $60\pm4\cdot n$ Hz, where n = 1, 2, ···. However, these excitations were totally masked by the sidebands of the current fundamental-frequency component of 60 Hz due to its high magnitude. The 1P-invariant PSD method failed to detect the bearing cage fault for the testing WTG by using the current measurements directly.

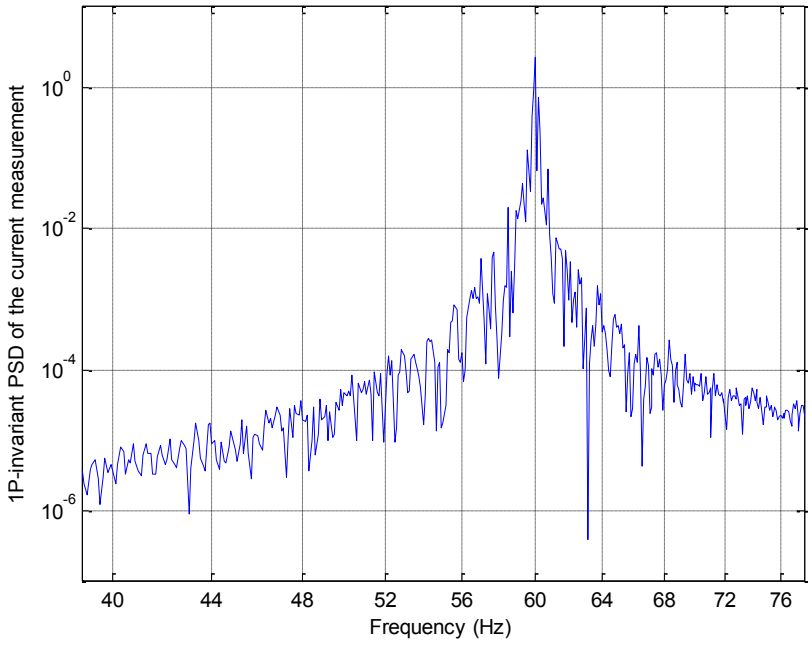

Figure 7.34: 1P-invariant PSD of the current measurement in the second bearing cage fault case in Section 7.3.2.

The proposed method was also applied to obtain the 1P-invariant PSD of the WTG current measurement for the four blade imbalance scenarios and the baseline case. By using the proposed method, the base frequency f_b was chosen to be 10 Hz. Due to

current frequency modulation with the 1P frequency, the fault characteristic frequencies should appear at 60Hz ±1P, which are 50 Hz and 70 Hz. The variable 1P frequency has been converted to a constant value of 10 Hz. The results are compared in Figures 7.35, 7.36 and 7.37, where excitations were observed at 50 Hz and 70 Hz only in the worst 4% blade imbalance scenario, but excitations cannot be clearly observed in other blade imbalance scenarios, because the fault characteristic frequencies in the current signal are too close to the 60 Hz fundamental-frequency component and, therefore, are masked by the sidebands of the fundamental-frequency component in the 1P-invariant PSD.

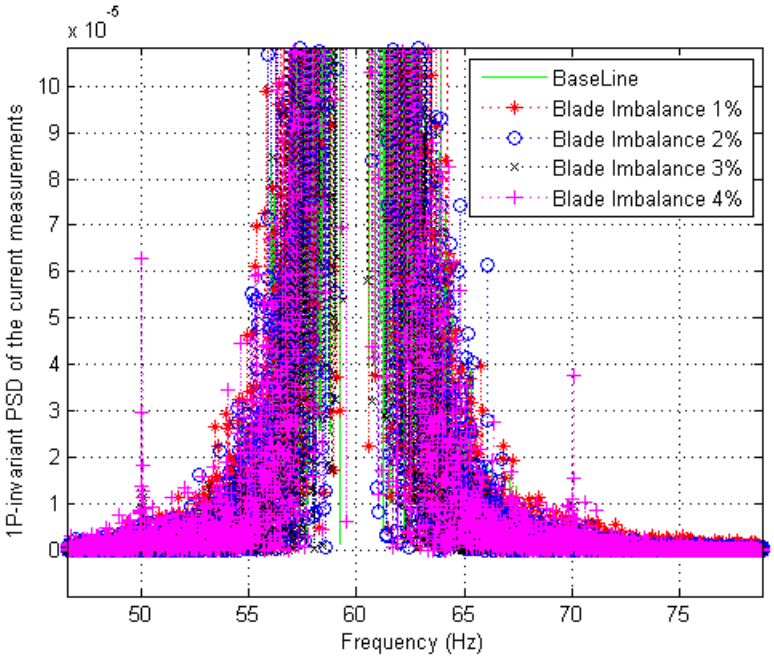

Figure 7.35: Comparison of the 1P-invariant PSD of the current measurements for the blade imbalance scenarios against the baseline case in a wide frequency range.

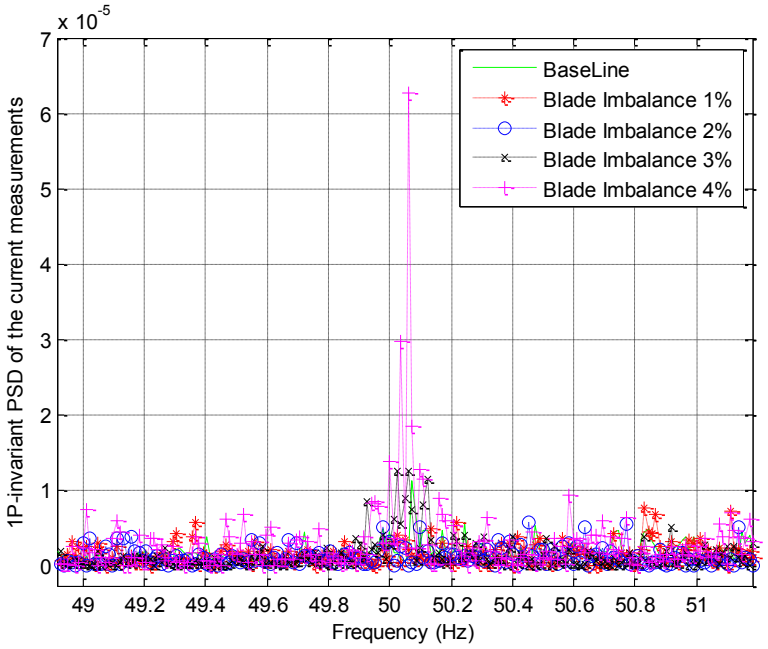

Figure 7.36: Comparison of the 1P-invariant PSD of the current measurements for the blade imbalance scenarios against the baseline case around 50 Hz.

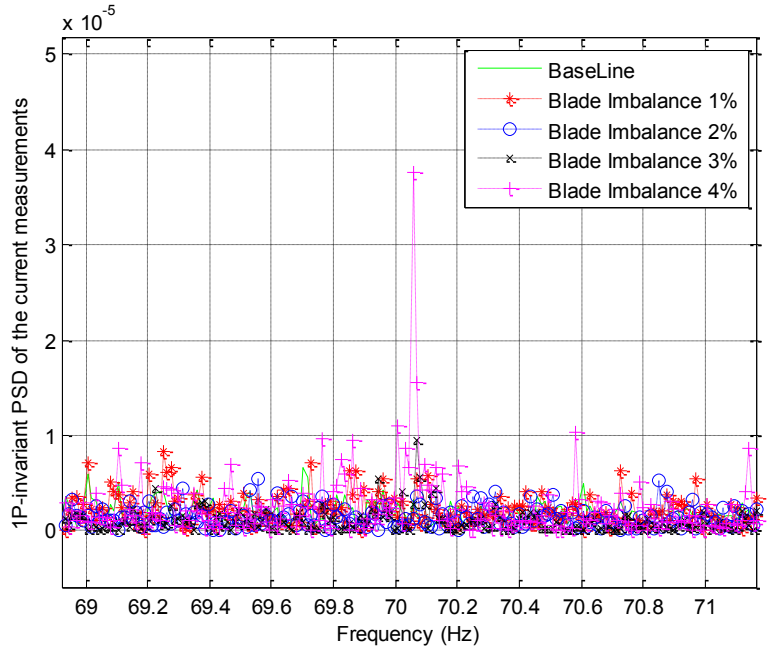

Figure 7.37: Comparison of the 1P-invariant PSD of the current measurements for the blade imbalance scenarios against the baseline case around 70 Hz.

7.5 Experimental Verification for Wavelet-Based Filter

The testing WTG with a pretreated bearing (no lubricant) was operated in the wind tunnel. During the experiment, the wind turbine was operated in variable-speed conditions with the shaft speed in the range of 360-700 rpm, which reached the maximum shaft speed of this testing WTG. Operating the wind turbine at high speeds can help accelerate the failure process of the bearing. In each 6-minute period the A/D converter records data for 120 seconds with a 10 kHz sampling frequency. The experiment took approximately 4.5 hours.

The proposed wavelet filter-based method was applied to the measured stator current signals for incipient bearing fault detection. The energy of the resulting wavelet-filtered signals represent the energy of the components in the current measurements related to the bearing fault and was used as the signature for incipient bearing fault detection. The results are shown in Figure 7.38. The fault index I_w of the wavelet-filtered stator currents kept increasing during the experiment, since the bearing condition was degrading quickly during this period due to the lack of lubricant. Therefore, the proposed wavelet-based filter can be used to extract the fault signature from the stator current measurements. The fault index I_w can be used to discover the physical condition of the wind turbine bearing effectively. The RMS value of the vibration measurement is compared in Figure 7.39, which confirms the health degradation of the testing bearing in the last one hour of the experiment.

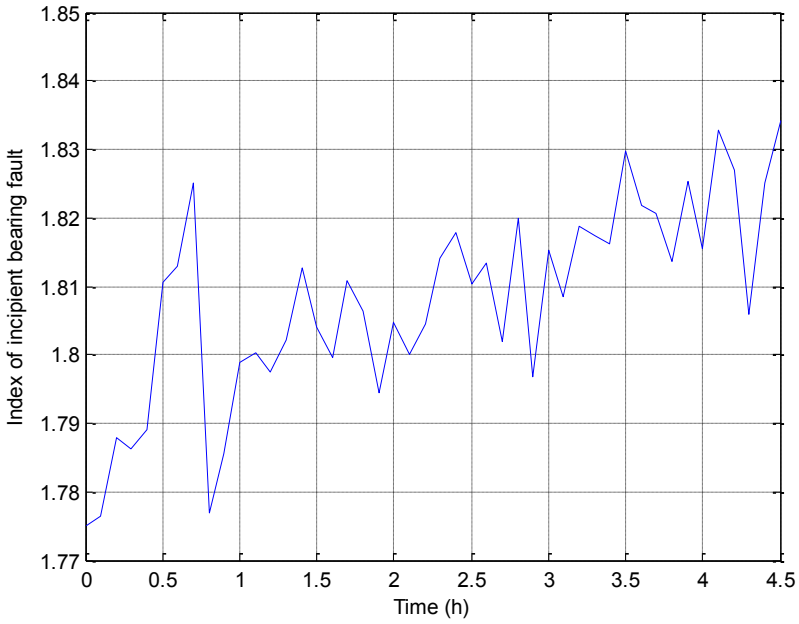

Figure 7.38: Fault index for current-based incipient bearing fault detection.

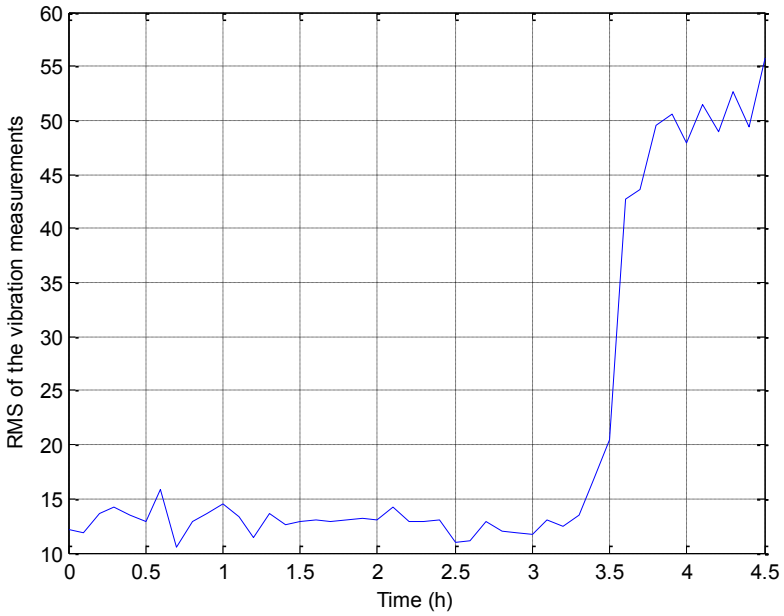

Figure 7.39: RMS value of the vibration measurement.

The experimental result of incipient bearing fault detection in Figure 7.38 was further analyzed by using the statistical control method-based fault index evaluator. The bearing was assumed to be in the healthy condition in the first hour of the experiment. Therefore, the bearing fault index I_w in the first hour were applied to calculate the threshold $\mu+3\sigma$, which was calculated to be 1.824. As shown in Figure 7.40, the energy of the WTG bearing fault index keeps increasing during the experiment due to the degrading bearing condition. From the beginning to the 3.5th hour of the experiment, all the bearing fault index samples are below the threshold. Form the 3.5th hour to the end of the experiment, 60% of bearing fault index samples exceeds the threshold. Therefore, the testing WTG bearing was in a deteriorated physical condition in the last hour of the experiment.

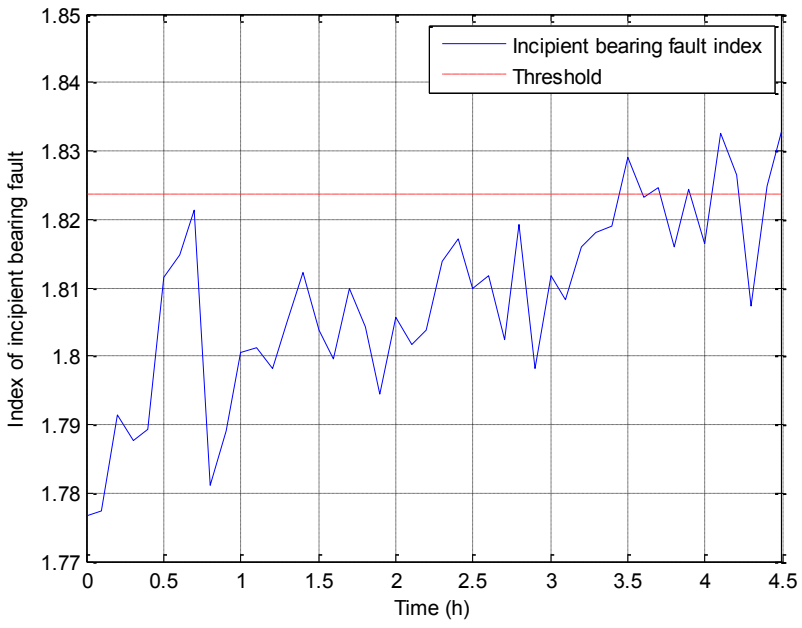

Figure 7.40: The bearing fault index with the threshold generated by the fault index evaluator.

Chapter 8 Conclusions, Contributions, and Recommendations for Future Research

The goal of this research is to develop novel generator current measurement-based online nonintrusive condition monitoring and fault detection methods for WTGs. The proposed methods do not require any additional sensors or data acquisition equipment, since generator current signals have already been used for wind turbine control. Most major faults in WTGs, including the faults in bearings, blades, and shaft/rotor systems, are able to be detected by using the proposed methods. Furthermore, the proposed methods can be easily integrated into existing wind turbine control, protection and monitoring systems and offer a means to achieve condition-based smart maintenance for WTGs.

Two types of WTG faults have been considered in this research: Type 1 faults, such as blade imbalance, aerodynamic asymmetric, and generator rotor faults, which have characteristic frequencies in the frequency spectra of current signals; and Type 2 faults, such as WTG incipient bearing faults, which are incipient faults in WTG components without any characteristic frequencies in the frequency spectra of current signals.

The vibrations of WTGs generated by the WTG shaft torque variations caused by WTG faults modulate the amplitude and the frequency of the WTG current signals. A model has been derived to analyze the effects of WTG faults on current signals for both direct-drive PMSG wind turbines and DFIG wind turbines. Based on this model, appropriate frequency and amplitude demodulation methods have been proposed to facilitate WTG condition monitoring and fault detection using only one phase generator

current measurement. Experimental results have validated the model and the proposed demodulation methods for WTG fault detection. The advantages of using current frequency or/and amplitude demodulated signals over directly using current measurements have also been demonstrated by experimental results.

Two 1P-invariant PSD methods have been proposed to extract the signatures of Type1 WTG faults. The methods process the WTG current demodulated signals in a way such that the variable characteristic frequencies of WTG faults become constant values in the 1P-invariant PSD spectra of current demodulated signals. Simulation studies have been carried out in a FAST, TurbSim and Simulink combined environment for a 10-kW direct-drive WTG with blade imbalance and aerodynamic asymmetry faults. Experimental studies have been performed in a wind tunnel facility for a 160-W direct-drive WTG with blade imbalance, blade defects, generator rotor fault, and bearing faults. Both simulation and experimental data have been processed by using the proposed methods and the results have confirmed that the proposed methods are effective to detect and quantify various WTG faults in variable-speed operating conditions by only using one phase current measurements. The proposed methods are able to clearly identify excitations at the characteristic frequencies of WTG faults. Therefore, it is sensitive to faults and is immune from interferences near fault characteristic frequencies. Compared to other signal analysis methods, such as wavelet analysis, Hilbert-Huang transform, etc., the proposed methods are less complex and have a lower computational cost and, therefore, are good for online fault detection. Furthermore, the traditional PSD analysis is a well-developed method for fault detection of rotating machines. Therefore, the

proposed 1P-invariant PSD methods can be easily integrated into existing condition monitoring and fault detection systems used in the wind industry.

Moreover, an impulse detection method has then been designed to evaluate the fault signatures of Type 1 WTG faults. If an impulse is detected at the characteristic frequency of a WTG fault, an alert will be generated and maintenance of the WTG is required. Experimental studies for the testing WTG have shown that the proposed impulse detection method can effectively detect impulses generated by various faults for the WTG operating in variable-speed conditions.

A novel wavelet filter-based algorithm has been developed for detecting generalized roughness of WTG bearings (Type 2 WTG faults) only using current measurements. The method decomposes the current measurements by using DWT. The fault-related components in current signals are located in the fluctuations of the wavelet filtered current signals due to the subtle and broad-band features of the fault components. The total energy of fluctuations in the wavelet filtered current signals are then calculated and used as the index of the incipient bearing faults. Experimental data have been obtained from the testing WTG with a developed bearing generalized roughness fault. These data have been used by the proposed method for incipient bearing fault detection. The results have shown that the proposed method is effective for incipient bearing fault detection of WTGs operating in variable-speed conditions. To evaluate the physical condition of WTGs having incipient bearing faults, a statistical control method has been designed to provide a threshold or limit for the fault index of the incipient bearing faults. The mean μ and standard deviation σ of the fault index when the bearing is in the healthy condition were calculated to determine the threshold $\mu+3\sigma$. When the fault index

frequently exceeds the threshold, it indicates that the WTG is in a deteriorated condition and maintenance is required. The incipient bearing fault in the experimental study was successfully identified by using the proposed statistical control method-based fault index evaluator.

The contributions of this dissertation are summarized as follows:

- The existing methods for WTG condition monitoring and fault detection and the signal processing methods used for current-based WTG fault detection have been reviewed in this dissertation research.
- A current-based framework has been proposed for online nonintrusive condition monitoring and fault detection for WTGs. WTG faults have been categorized into two classes. For Type 1 WTG faults, two 1P-invariant PSD methods and an impulse detection method have been developed to evaluate the physical condition of the wind turbine components. A wavelet-based filter and a stochastic control method-based fault index evaluator have been developed to extract the fault signatures to detect Type 2 WTG faults.
- The effects of WTG faults on generator current signals have been modeled and analyzed. Base on the model and analysis, current frequency and amplitude demodulation methods have been developed to facilitate the detection of Type 1 WTG faults.
- Two novel 1P-invariant PSD methods have been developed for fault signature extraction of Type 1 WTG faults using current demodulated signals. In the proposed

methods, the current demodulated signals are resampled based on the shaft rotating frequencies (i.e., 1P frequencies) of the WTGs. Consequently, the variable characteristic frequencies of Type 1 WTG faults are converted to constant values when the WTGs operate in variable-speed conditions. The classical PSD analysis is then used to extract the signatures of Type 1 WTG faults in the resampled current demodulated signals.

- An impulse detection method has been designed to detect the excitations in the 1P-invariant PSD spectra of current demodulated signals. The method firstly converts the 1P-invariant PSD spectra to locally normalized spectra. A median filter has then been designed to generate a threshold to identify impulses in locally normalized 1P-invariant PSD signals, from which the excitations corresponding to WTG faults can be identified.
- A wavelet-based filter has been developed to filter out the dominant noise components in current signals. The total energy of the filtered current signals is then used as the fault index for detection of Type 2 WTG faults.
- A 10 kW WTG equipped with a PMSG has been modeled in a FAST, TurSim and Simulink combined software platform. Simulation studies have been performed for verification of the 1P-invariant PSD method using the model WTG.
- Extensive experimental studies have been performed in a wind tunnel for small direct-drive PMSG wind turbines with blade imbalance fault, blade defects, generator rotor fault, and bearing faults. Results have been used to demonstrate the effectiveness of the proposed 1P-invariant PSD methods, impulse detection method,

wavelet filter-based method, and statistical control-based fault index evaluator for online nonintrusive condition monitoring and fault detection for WTGs.

Recommendations for future research are listed as follows:

- Future work could focus on identification the locations and root causes of WTG faults. Many Type 1 WTG faults mentioned in this dissertation share same characteristic frequencies in 1P-invariant PSD spectra of current demodulated signals. It is desired to identify the locations and root causes of WTG faults to facilitate the maintenance. To achieve this objective, further research on the effects of WTG faults on current signals is needed.
- It is desired that the physical condition of WTGs is prognosed by using the extracted fault features. Prognosis of WTG physical condition is important to improve the reliability of WTGs. If maintenance can be scheduled just before the live time of wind turbine components, the components can be fully used and the cost related to wind turbine faults can be reduced.
- To improve the performance of WTG condition monitoring and fault detection, multiple electrical measurements (voltages and currents) are recommended to be used, instead of only using one phase current measurement. Measurements of voltages and currents constitute a multi-sensor fusion, which may increase the accuracy of fault detection and then improve the reliability of the WTGs.
- Experiments on large-scale wind turbines are suggested in the future research to further validate the proposed WTG condition monitoring and fault detection methods.

Such extension is an important step before deploying the proposed methods in real-world applications.

Bibliography

[1] The American Wind Energy Association, "AWEA U.S. Wind Industry First Quarter 2012 Market Report," 2012, [Online]. Available: http://www.awea.org/learnabout/publications/reports.

[2] United States Department of Energy, "20% wind energy by 2030: increasing wind energy's contribution to U.S. electricity supply," Rep. DOE/GO-102008-2567, July 2008.

[3] The European Wind Energy Association, "Pure Power: Wind energy targets for 2020 and 2030," 2011, [Online]. Available: http://www.ewea.org.

[4] Energy Research Institute, National Development and Reform Commission (NDRC) of P. R. China, "China Wind Energy Development Roadmap 2050," 2011, [Online]. Available: http://www.iea.org/papers/roadmaps/china_wind.pdf.

[5] J. Ribrant and L. M. Bertling, "Survey of failures in wind power systems with focus on Swedish wind power plants during 1997-2005," *IEEE Trans. Energy Conversion*, vol. 22, no. 1, pp. 167–173, Mar. 2007.

[6] W. Musial and B. Ram, "Large-scale offshore wind power in the United States: Assessment of opportunities and barriers," Technical Report, National Renewable Energy Laboratory, Sept. 2010, [Online]. Available: http://www.nrel.gov/wind/pdfs/40745.pdf

[7] T. W. Verbruggen, "Wind turbine operation & maintenance based on condition monitoring," Final Report, Energy Research Center of the Netherlands (ECN), April 2003, [Online]. Available: www.ecn.nl/docs/library/report/2003/c03047.pdf

[8] C. A. Walford, "Wind turbine reliability: understanding and minimizing wind turbine operation and maintenance costs," Sandia National Laboratories, Rep. SAND2006-1100, Mar. 2006.

[9] M. A. Aziz, H. Noura, and A. Fardoun, "General review of fault diagnostic in wind turbines," in *Proc. 18th Mediterranean Conference on Control & Automation*, Jun. 2010, pp. 1302–1307.

[10] R. W. Hyers, J. G. McGowan, K. L. Sullivan, J. F. Manwell, and B. C. Syrett, "Condition monitoring and prognosis of utility scale wind turbines," *Energy Materials*, vol. 1, no. 3. pp. 187–203, Sept. 2006.

[11] Y. Amirat, M. E. H. Benbouzid, E. Ahmar, B. Bensaker, and S. Turri, "A brief status on condition monitoring and fault diagnosis in wind energy conversion systems," *Renewable and Sustainable Energy Review*, vol. 13, pp. 2629–2636, Dec. 2009.

[12] A. K. S. Jardine and A. H. Tsang, *Maintenance, Replacement, and Reliability Theory and Applications*, Taylor & Francis Group, 2006.

[13] J. Ribrant, "Reliability performance and maintenance - a survey of failure in wind power systems," M.Sc. dissertation, Dept. Elec. Eng., Univ., KTH, Sweden, 2006.

[14] T. Jin and M. Mechehoul, "Minimize production loss in device testing via condition based equipment maintenance," *IEEE Trans. Automation Science & Engineering*, vol. 7, no. 4, pp. 958–963, Oct. 2010.

[15] W. Q. Jeffries, J. A. Chambers, and D. G. Infield, "Experience with bicoherence of electrical power for condition monitoring of wind turbine blades," *IEE Proceedings: Vision, Image and Signal Processing*, vol. 145, no. 3, pp. 141–148, Jun. 1998.

[16] C. S. Tsai, C. T. Hsieh, and S. J. Huang, "Enhancement of damage detection of wind turbine blades via CWT-based approaches," *IEEE Trans. Energy Conversion*, vol. 21, no. 3, pp. 776–781, Sept. 2006.

[17] M. Zhao, D. Jiang, and S. Li, "Research on fault mechanism of icing of wind turbine blades," in *Proc. 2009 World Non-Grid-Connected Wind Power and Energy Conference*, Sept. 2009, pp. 1–4.

[18] R. Ramlau and J. Niebsch, “Imbalance estimation without test masses for wind turbines,” *Journal of Solar Energy Engineering*, vol. 131, no. 1, pp. 011010-1 – 011010-7, Feb. 2009.

[19] A. Kusiak and A. Verma, “A data-driven approach for monitoring blade pitch faults in wind turbines,” *IEEE Trans. Sustainable Energy*, vol. 2, no. 1, pp. 87–96, Jan. 2011.

[20] D D. J. Gardels, W. Qiao, and X. Gong, “Simulation studies on imbalance faults of wind turbines,” in *Proc. IEEE Power & Energy Society General Meeting 2010*, July 2010, pp. 1–5.

[21] X. Wei and L. Liu, “Fault detection of large scale wind turbine systems,” in *Proc. 5th International Conference on Computer Science and Education*, Aug. 2010, pp.1299–1304.

[22] X. Zhang, S. He, P. Zho, and W. Wang, “Summarization and study of fault diagnosis technology of the main components of wind turbine generator system,” in *Proc. IEEE International Conference on Sustainable Energy Technologies*, Nov. 2008, pp. 1223–1226.

[23] B. Lu, Y. Li, X. Wu, and Z. Yang, “A review of recent advances in wind turbine condition monitoring and fault diagnosis,” in *Proc. 2009 IEEE Symposium on Power Electronics and Machines in Wind Applications*, Jun. 2009, pp. 1–7.

[24] A. R. Mohanty and C. Kar, “Fault detection in a multistage gearbox by demodulation of motor current waveform,” *IEEE Trans. Industrial Electronics*, vol. 53, no. 4, pp. 1285–1297, Jun. 2006.

[25] Z. Zhang, A. Verma, and A. Kusiak, “Fault analysis and condition monitoring of the wind turbine gearbox,” *IEEE Trans. Energy Conversion*, vol. 27, no. 2, pp. 526–535, Jun. 2012.

[26] J, Huang, H. Pan, and S. Bi, “Bispectrum entropy feature extraction and its application for fault diagnosis of gearbox,” in *Proc. IEEE International Conference on Fuzzy Systems*, Jul. 2010, pp. 1–6.

[27] P. J. Tavner, J. Xiang, and F. Spinato, “Reliability analysis for wind turbines,” *Wind Energy*, vol. 10, pp. 1–18, 2007.

[28] Y. Amirat, M. E. H. Benbouzid, B. Bensaker, and R. Wamkeue, “Condition monitoring and fault diagnosis in wind energy conversion systems: A review”, in *Proc. IEEE International Electric Machines and Drives Conference*, May 2007, vol. 2, pp. 1434–1439.

[29] F. Spinato, P. J. Tavner, G. J. W. van Bussel, and E. Koutoulakos, “Reliability of wind turbine subassemblies,” *IET Renew. Power Generation*, vol. 3, no. 4, pp. 1–15, 2009.

[30] M. E. H. Benbouzid, “Bibliography on induction motors faults detection and diagnosis,” *IEEE Trans. Energy Conversion*, vol. 14, pp. 1065–1074, Dec. 1999.

[31] M. E. H. Benbouzid, “A review of induction motors signature analysis as a medium for faults detection,” *IEEE Trans. Industrial Electronics*, vol. 47, no. 5, pp. 984–993, Oct. 2000.

[32] A. Siddique, G. S. Yadava, and B. Singh, “A review of stator fault monitoring techniques of induction motors,” *IEEE Trans. Energy Conversion*, vol. 20, no. 1, pp. 106–114, Mar. 2005.

[33] K. A. Loparo, M. L. Adams, W. Lin, M. F. A. Magied, and N. Afshari, “Fault detection and diagnosis of rotating machinery,” *IEEE Trans. Industrial Electronics*, vol. 47, no. 5, pp. 1005–1014, Oct. 2000.

[34] S. Nandi, H. A. Toliyat, and X. Li, “Condition monitoring and fault diagnosis of electrical motors—A review,” *IEEE Trans. Energy Conversion*, vol. 20, no. 4, pp. 719–729, Dec. 2005.

[35] J. R. Stack, T. G. Habetler, and R. G. Harley, “Fault classification and fault signature production for rolling element bearings in electric machines,” *IEEE Trans. Industry Applications*, vol. 40, no. 3, pp. 735–739, May/Jun. 2004.

[36] Z. Daneshi-Far, G. A. Capolino, and H. Henao, “Review of failures and condition monitoring in wind turbine generators”, in *Proc. XIX International Conference on Electrical Machines*, Sept. 2010, pp. 1–6.

[37] F. Zhou, “Research on online monitoring and diagnosis of bearing fault of wind turbine gearbox based on undecimated wavelet transformation,” in *Proc. IEEE Youth Conference on Information Computing and Telecommunications*, Nov. 2010, pp. 251–254.

[38] L. M. Popa, B. B. Jensen, E. Ritchie, and I. Boldea, “Condition monitoring of wind generators,” in *Proc. IEEE IAS Annual Meeting*, Oct. 2003, vol. 3, pp. 1839–1846.

[39] D. Jiang, Q. Huang, and L. Hong, “Theoretical and experimental study on wind wheel unbalance for a wind turbine,” in *Proc. World Non-Grid-Connected Wind Power and Energy Conference,* Sept. 24–26, 2009.

[40] X. An, D. Jiang, and S. Li, “Application of back propagation neural network to fault diagnosis of direct-drive wind turbine,” in *Proc. World Non-Grid-Connected Wind Power and Energy Conference*, Nov. 2010, pp. 1–5.

[41] J. Yan and Y. Xu, “Operational fault feature extraction of blade based on vibration of wind turbine,” in *Proc. International Conference on Control, Automation and Systems Engineering*, Jul. 2011, pp. 1–3.

[42] S. Li, D. Jiang, and M. Zhao, “Experimental investigation and analysis for gearbox fault,” in *Proc. World Non-Grid-Connected Wind Power and Energy Conference*, Nov. 2010, pp. 1–6.

[43] R. R. Schoen, T. G. Habetler, F. Kamran, and R. Bartheld, “Motor bearing damage detection using stator current monitoring,” *IEEE Trans. Industry Applications*, vol. 31, no. 6, pp. 1274–1279, Nov./Dec. 1995.

[44] M. Blodt, P. Granjon, B. Raison, and G. Rostaing, “Models for bearing damage detection in induction motors using stator current monitoring,” *IEEE Trans. Industrial Electronics*, vol. 55, no. 4, pp. 1813–1822, Apr. 2008.

[45] S. J. Watson, B. J. Xiang, W. Yang, P. J. Tavner, and C. Crabtree, “Condition monitoring of the power output of wind turbine generators using wavelets,” *IEEE Trans. Energy Conversion*, vol. 25, no. 3, pp. 715–721, Sept. 2010.

[46] X. Gong and Wei Qiao, “Bearing fault detection for direct-drive wind turbines via stator current spectrum analysis,” in *Proc. Energy Conversion Congress and Exposition*, Sept. 2011, pp. 313–318.

[47] X. Zhang, S. Yang, and X. Li, “Wind turbine bearing condition monitoring based on high frequency resonance method,” in *Proc. International Conference on Electronics, Communications and Control*, Sept. 2011, pp. 1792–1795.

[48] W. Yang, P. J. Tavner, C. J. Crabtree, and M. Wilkinson, “Cost-effective condition monitoring for wind turbines,” *IEEE Trans. Industrial Electronics*, vol. 57, no. 1, pp. 263–271, Jan. 2010.

[49] *Mechanical Vibration–Evaluation of Machine Vibration by Measurements on Non-rotating Parts–Part 1*: General Guidelines, ISO 10816-1:1995(E), 1995.

[50] *Mechanical Vibration–Evaluation of Machine Vibration by Measurements on Non-rotating Parts–Part 3*: General Guidelines, ISO 10816-3:1998(E), 1998.

[51] J. R. Stack, “Fault signature detection for rolling element bearings in electric machines,” PhD Dissertation, Georgia Institute of Technology, Nov. 2002.

[52] M. R. Wilkinson, F. Spinato, and P. J. Tavner, “Condition monitoring of generators and other subassemblies in wind turbine drive trains”, in *Proc. IEEE International Symposium on Diagnostics for Electric Machines, Power Electronics and Drives*, Sep. 2007, pp. 388–392.

[53] M. Wilkinson and P. Tavner, “Extracting condition monitoring information from a wind turbine drive train,” in *Proc. 39th International Universities Power Engineering Conference*, pp. 591–594, 2004.

[54] M. Wilkinson, and P. Tavner, "Extracting condition monitoring information from a wind turbine drive train," in Proc. *39th International Universities Power Engineering Conference*, pp. 591–594, 2004.

[55] W. Yang, P. Tavner, and M. Wilkinson, "Wind turbine condition monitoring and fault diagnosis using both mechanical and electrical signatures," in *Proc. IEEE International Conference on Advanced Intelligent Mechatronics*, pp. 1296–1301, Jul. 2008.

[56] *IEEE Standard for Petroleum and Chemical Industry - Severe Duty Totally Enclosed Fan-Cooled (TEFC) Squirrel Cage Induction Motors - Up to and Including 370 kW (500 hp)*, IEEE Std 841-2001, 2001.

[57] P. Papadopoulos and L. Cipcigan, "Wind turbines' condition monitoring: an ontology model," in *Proc. International Conference on Sustainable Power Generation and Supply*, Apr. 2009, pp. 1–4.

[58] B. Maru and P. A. Zotos, "Anti-friction bearing temperature rise for NEMA frame motors," *IEEE Trans. Industry Applications*, vol. 25, no. 5, pp. 883–888, Sep./Oct. 1989.

[59] Q. Wang, Z. Zhu, J. Duanmu, and X. Ge, "Oil filter debris analysis of aero-engine," in *Proc. 9th International Conference on Reliability, Maintainability and Safety*, Jun. 2011, pp. 276–278.

[60] A. Amayri, Z. Tian, and T. Jin, "Condition based maintenance of wind turbine systems considering different turbine types," in *Proc. International Conference on Quality, Reliability, Risk, Maintenance, and Safety Engineering*, Jun. 2011, pp. 596–600.

[61] W. Zhou, T. G. Habetler, and R. G. Harley, "Bearing condition monitoring methods for electric machines: A general review," in *Proc. IEEE International Symposium on Diagnostics for Electric Machines, Power Electronics and Drives*, Sept. 2007, pp. 3–6.

[62] M. W. Hawman, and W. S. Galinaitis, "Acoustic emission monitoring of rolling element bearings," *IEEE Proceedings of Ultrasonics Symposium*, vol. 2, pp. 885–889, Oct. 1988.

[63] W. Lu and F. Chu, “Condition monitoring and fault diagnostics of wind turbines,” in *Proc. Prognostics and Health Management Conference*, Jan. 2010, pp. 1–11.

[64] C. Chen, C. Sun, Y. Zhang, and N. Wang, “Fault diagnosis for large-scale wind turbine rolling bearing using stress wave and wavelet analysis,” in *Proc. 8th Int. Conf. on Electrical Machines and Systems*, vol. 3, Sept. 2005, pp. 2239–2244.

[65] L. Chen, Y. Zhang, and X. Xia, “Contact stress and deformation of blade bearing in wind turbine,” in *Proc. International Conference on Measuring Technology and Mechatronics Automation*, Mar. 2010, pp. 833–836.

[66] L. Li, W. Lu, and F. Chu, “Application of AE techniques for the detection of wind turbine using Hilbert-Huang transform,” in *Proc. Prognostics and Health Management Conference*, Jan. 2010, pp. 1–7.

[67] F. Zhang, Y. Li, Z. Yang, and L. Zhang, “Investigation of wind turbine blade monitoring based on optical fiber Brillouin sensor,” in *Proc. International Conference on Sustainable Power Generation and Supply*, Apr. 2009, pp. 1–4.

[68] S. G. M. Kramer, F. P. Leon, Y. N. M. Hernandez, B. Lewke, “Integration of a distributed fiber optic current sensor setup for lightning detection in wind turbines,” in *Proc. Instrumentation and Measurement Technology Conference Proceedings*, May 2007, pp. 1–5.

[69] E. Ahmar, V. Choqueuse, M. E. H. Benbouzid, Y. Amirat, J. Assad, R. Karam, and S. Farah, “Advanced signal processing techniques for fault detection and diagnosis of a wind turbine induction generator drive train: A comparative study,” in *Proc. IEEE Energy Conversion Congress & Exposition*, Sept. 2010, pp. 3576–3581.

[70] Y. Amirat, V. Choqueuse, M. E. H. Benbouzid, and J. F. Charpentier, “Bearing fault detection in DFIG-based wind turbines using the first intrinsic mode function,” in *Proc. XIX International Conference on Electrical Machines*, Sept. 2010, pp. 1–6.

[71] Y. Amirat, V. Choqueuse, and M. E. H. Benbouzid, “Condition monitoring of wind turbines based on amplitude demodulation,” in *Proc. IEEE Energy Conversion Congress & Exposition*, Sept. 2010, pp. 2417–2421.

[72] S. Watson, B. Xiang, W. Yang, P. Tavner, and C. Crabtree, “Condition monitoring of the power output of wind turbine generators usingwavelets,” *IEEE Trans. Energy Conversion*, vol. 25, no. 3, pp. 715–721, Sept. 2010.

[73] S. A. Saleh and C. R. Moloney, “Development and testing of wavelet packet transform-based detector for ice accretion on wind turbines,” in *Proc. IEEE Digital Signal Processing Workshop and IEEE Signal Processing Education Workshop*, Jan. 2011, pp. 72–77.

[74] X. Gong and W. Qiao, “Imbalance fault detection of direct-drive wind turbines using generator current signals,” *IEEE Trans. Energy Conversion*, vol. 27, no. 2, pp. 468–476, Jun. 2012.

[75] A. Zaher, S. D. J. McArther, D. G. Infield, and Y. Patel, “Online wind turbine fault detection through automated SCADA data analysis,” *Wind Energy*, vol. 12, no. 6, pp. 574–593, Sept. 2009.

[76] X. Gong, X. Yang, W. Qiao, "Wind speed and rotor position sensorless control for direct-drive PMG wind turbine", in *Proc. IEEE Industry Appl. Society Annual Meeting*, Oct. 2010, pp. 1–8.

[77] R. Zavadil, N. Miller, A. Ellis, and E. Muljadi, “Making connections: Wind generation challenges and progress,” *IEEE Power Energy Magazine*, vol. 3, no. 6, pp. 26–37, Nov. 2005.

[78] X. Gong and W. Qiao, “Simulation investigation of wind turbine imbalance faults,” in *Proc. International Conference on Power System Technology*, Oct. 2010, pp. 1–7.

[79] S. A. McInerny and Y. Dai, “Basic vibration signal processing for bearing fault detection,” *IEEE Trans. Education*, vol. 46, no. 1, pp. 149–156, Feb. 2003.

[80] J. R. Stack, T. G. Habetler, and R. G. Harley, “Effects of machine speed on the development and detection of rolling element bearing faults,” *IEEE Power Electronics Letters*, vol. 1, no. 1, pp. 19–21, Mar. 2003.

[81] S. Yang, X. Li, and M. Liang, “Bearing fault diagnosis of a wind turbine using maximum likelihood detection,” in *Proc. International Conference on Electronic and Mechanical Engineering and Information Technology*, vol.6, Aug. 2011, pp. 3039–3042.

[82] S. Yang, X. Li, and M. Liang, “Bearing fault detection and diagnosis of a wind turbine,” in *Proc. International Conference on Consumer Electronics, Communications and Networks*, Apr. 2011, pp. 123–126.

[83] J. S. Walker, *A Primer on Wavelets and their Scientific Applications*, Chapman & Hall, 1999.

[84] Y. Gritli, A. Stefani, F. Filippetti, and A. Chatti, “Stator fault analysis based on wavelet technique for wind turbines equipped with DFIG”, in *Proc. International Conference on Clean Electrical Power*, Jun. 2009, pp. 485–491.

[85] M. R. Guasp, J. A. Daviu, M. P. Sanchez, R. P. Panadero, and J. P. Cruz, “A general approach for the transient detection of slip-dependent faulty components based on the discrete wavelet transform,” *IEEE Trans. Industrial Electronics*, vol. 55, no. 12, pp. 4167–4180, Dec. 2008.

[86] H. Qiu, J. Lee, J. Lin, and G. Yu, “Wavelet filter-based weak signature detection method and its application on rolling element bearing prognosis,” *Journal of Sound and Vibration*, vol.289, no. 4–5, pp.1066–1090, 2006.

[87] X. Sheng, S. Wan, and F. Tian; , “Gear fault diagnosis of wind turbine generator system based on lifting wavelet- zooming envelope analysis,” in *Proc.* 2^{nd} *International Conference on Mechanic Automation and Control Engineering*, Jul. 2011, pp. 1332–1335.

[88] Y. Guo, W. Yan, and Z. Bao, "Gear fault diagnosis of wind turbine based on discrete wavelet transform," in *Proc. 8th World Congress on Intelligent Control and Automation*, Jul. 2010, pp. 5804–5808.

[89] X. Yao, C. Guo. M. Zhong, Y. Li, G. Shan, and Y. Zhang, "Wind turbine gearbox fault diagnosis using adaptive morlet wavelet spectrum," in *Proc.* 2nd *International Conference on Intelligent Computation Technology and Automation*, vol. 2, Oct. 2009, pp. 580–583.

[90] F. Zhou, "Fault diagnosis method of gear of wind turbine gearbox based on un-decimated wavelet transformation," in *Proc. International Conference on Computer Design and Applications*, vol. 4, Jun. 2010, pp. 606–609.

[91] W. Yang, P. Tavner, and M. Wilkinson, "Condition monitoring and fault diagnosis of a wind turbine with a synchronous generator using wavelet transforms," in *Proc. 4th IET Conference on Power Electronics, Machines and Drives*, Apr. 2008, pp. 6–10.

[92] Y. Amirat, V. Choqueuse, and M. E. H. Benbouzid, "Wind turbines condition monitoring and fault diagnosis using generator current amplitude demodulation," in *Proc. IEEE International Energy Conference and Exhibition*, Dec. 2010, pp. 310–315.

[93] H. Zoubek, S. Villwock, and M. Pacas, "Frequency response analysis for rolling-bearing damage diagnosis," *IEEE Trans. Industrial Electronics*, vol. 55, no. 12, pp. 4270–4276, Dec. 2008.

[94] B. Trajin, J. Regnier, and J. Faucher, "Comparison between stator current and estimated mechanical speed for the detection of bearing wear in asynchronous drives," *IEEE Trans. Industrial Electronics*, vol. 56, no. 11, pp. 4700–4709, Nov. 2009.

[95] W. Teng, Q. Gao, X. Wu, and Y. Liu, "Defect detection of wind turbine gearbox using demodulation analysis," in *Proc.* 2nd *International Conference on Mechanic Automation and Control*, Jul. 2011, pp. 4838–4841.

[96] R. Yan and R. X. Gao, “A tour of the Hilbert–Huang transform: An empirical tool for signal analysis,” *IEEE Instrumentation & Measurement Magazine*, vol. 10, no. 5, pp. 40–45, Oct. 2007.

[97] E. H. Bouchikhi, V. Choqueuse, M. E. H. Benbouzid, J. F. Charpentier, and G. Barakat, “A comparative study of time-frequency representations for fault detection in wind turbine,” in *Proc. 37th Annual Conference on IEEE Industrial Electronics Society*, Nov. 2011, pp. 3584–3589.

[98] C. Kuo, P. Chen, A. Liu, and L. Chen, “Defect type recognition system for wind turbine by subtractive clustering,” in *Proc. 2nd International Conference on Intelligent System Design and Engineering Application*, Jan. 2012, pp. 1404–1408.

[99] A. Espinosa, J. Rosero, J. Cusido, L. Romeral, and J. Ortega, “Fault detection by means of Hilbert–Huang transform of the stator current in a PMSM with demagnetization,” *IEEE Trans. Energy Conversion*, vol. 25, no. 2, pp. 312–318, Jun. 2010.

[100] S. Muller, M. Deicke, and R. W. De Doncker, “Doubly fed induction generator systems for wind turbines,” *IEEE Industry Applications Magazine*, vol. 8, no. 3, pp. 26–33, May/Jun. 2002.

[101] S. Li, T. A. Haskew, K. A. Williams, and R. P. Swatloski, “Control of DFIG wind turbine with direct-current vector control configuration,” *IEEE Trans. Sustainable Energy*, vol. 3, no. 1, pp. 1–11, Jan. 2012.

[102] A. Abedini and A. Nasiri, “PMSG wind turbine performance analysis during short circuit faults,” in *Proc. IEEE Electrical Power Conference*, Oct. 2007, pp. 160–165.

[103] H. Ahuja, G. Bhuvaneswari, R. Balasubramanian, “Performance comparison of DFIG and PMSG based WECS,” in *Proc. IET Conference on Renewable Power Generation*, Sept. 2011, pp. 1–6.

[104] H. Henao, H. Razik, and G. Capolino, "Analytical approach of the stator current frequency harmonics computation for detection of induction machines rotor faults," *IEEE Trans. Industry Applications*, vol. 41, no. 3, pp. 801–807, May/Jun. 2005.

[105] M. Seera, L. P. Chee, D. Ishak, and H. Singh, "Fault detection and diagnosis of induction motors using motor current signature analysis and a hybrid FMM–CART model," *IEEE Trans. Neural Networks and Learning Systems*, vol.23, no.1, pp.97–108, Jan. 2012

[106] J. Stack, T. G. Habetler, and R. G. Harley, "Bearing fault detection via autoregressive stator current modeling," *IEEE Trans. Industry Applications*, vol. 40, no. 3, pp. 740–747, May/Jun. 2004.

[107] W. Zhou, T. G. Habetler, and R. G. Harley, "Incipient bearing fault detection via motor stator current noise cancellation using Wiener filter," *IEEE Trans. Industry Applications*, vol. 45, no. 4, pp. 1309–1317, Jul./Aug. 2009.

[108] W. Zhou, T. G. Habetler, and R. G. Harley, "Bearing fault detection via stator current noise cancellation and statistical control," *IEEE Trans. Industrial Electronics*, vol. 55, no. 12, pp. 4260–4269, Dec. 2008.

[109] X. Gong, W. Qiao, and W. Zhou, "Incipient bearing fault detection via wind generator stator current and wavelet filter," in *Proc. 36th Annual Conference on IEEE Industrial Electronics Society*, Nov. 2010, pp. 2615–2620.

[110] F. Immovilli, A. Bellini, R. Rubini, and C. Tassoni, "Diagnosis of bearing faults in induction machines by vibration or current signals - a critical comparison" *IEEE Trans. Industry Applications*, vol. 46, no. 4, pp. 1350–1359, Jul./Aug. 2010.

[111] M. E. H. Benbouzid, M. Vieira, and C. Theys, "Induction motors' faults detection and localization using stator current advanced signal processing techniques," *IEEE Trans. Industrial Electronics*, vol. 14, no. 1, pp. 14–22, Jan. 1999.

[112] A. M. Knight and S. P. Bertani, “Mechanical fault detection in a medium-sized induction motor using stator current monitoring,” *IEEE Trans. Energy Conversion*, vol. 20, no. 4, pp. 753–760, Dec. 2005.

[113] M. Blodt, D. Bonacci, J. Regnier, M. Chabert, and J. Faucher, “On-line monitoring of mechanical faults in variable-speed induction motor drives using Wigner distribution,” *IEEE Trans. Industrial Electronics*, vol. 55, no. 2, pp. 522–533, Feb. 2008.

[114] J. F. Manwell, J. G. McGowan, and A. L. Rogers, *Wind Energy Explained,* West Sussex, England: John Wiley & Sons Ltd, 2002.

[115] B. Li, M. Y. Chow, Y. Tipsuwan, and J. C. Hung, “Neural-network-based motor rolling bearing fault diagnosis,” *IEEE Trans. Industrial Electronics*, vol. 47, no. 5, pp. 1060–1069, Oct. 2000.

[116] L. Frosini and E. Bassi, “Stator current and motor efficiency as indicators for different types of bearing faults in induction motors,” *IEEE Trans. Industrial Electronics*, vol. 57, no. 1, pp. 244–251, Jan. 2010.

[117] W. Qiao, X. Yang, and X. Gong, “Wind speed and rotor position sensorless control for direct-drive PMG wind turbines,” *IEEE Trans. Industry Applications*, vol. 48, no. 1, pp. 3–11, Jan./Feb. 2012.

[118] S. J. Chapman, *Electrical Machinery Fundamentals*, 4th edition, New York: McGraw-Hill, 2005.

[119] S. Oshita, N. Morinaga, and T. Namekawa, “Output signal-to-noise ratios for an amplitude-modulated noise carrier in a square-law detector,” *IEEE Trans. Communications*, vol. 21, no. 9, pp. 1054–1056, Sept. 1973.

[120] A. Oppenheim, R. Schafer, and W. Padgett, *Discrete-Time Signal Processing*, 3rd ed. Prentice Hall, 2009.

[121] X. Wang, B. Li, Z. Liu, H. T. Roman, O. L. Russo, K. K. Chin, and K. R. Farmer, “Analysis of partial discharge signal using the Hilbert-Huang Transform,” *IEEE Trans. Power Delivery*, vol. 21, pp. 1063–1067, 2006.

[122] M. Kumm, H. Klingbeil, and P. Zipf, “An FPGA-based linear all digital phase-locked loop,” *IEEE Trans. Circuits and Systems*, vol. 57, no. 9, pp. 2487–2497, Sept. 2010.

[123] T. Thacker, D. Boroyevich, R. Burgos, and F. Wang, “Phase-locked loop noise reduction via phase detector implementation for single-phase systems*,” IEEE Trans. Industrial Electronics*, vol. 58, pp. 2482–2490, Jun. 2011.

[124] D. Reynolds, “A 320 MHz CMOS triple 8 bit DAC with on-chip PLL and hardware cursor,” *IEEE J. Solid-state Circuits*, vol. 29, no. 12, pp. 1545–1551, Dec. 1994.

[125] W. Qiao, W. Zhou, J. M. Aller, and R. G. Harley, “Wind speed estimation based sensorless output maximization control for a wind turbine driving a DFIG,” *IEEE Trans. Power Electronics*, vol. 23, no. 3, pp. 1156–1169, May 2008.

[126] C. R. de Boor, *A Practical Guide to Splines*, Springer-Verlag, 1978.

[127] B. Akin, U. Orguner, H. A. Toliyat, and M. Rayner, “Low order PWM inverter harmonics contributions to the inverter-fed induction machine fault diagnosis,” *IEEE Trans. Industrial Electronics*, vol. 55, no. 2, pp. 610–619, Feb. 2008.

[128] D. L. Donoho, I. M. Johnstone, “Adapting to unknown smoothness via wavelet shrinkage,” *Journal of American Statistical Association* 90*,* pp. 1200–1224, 1995.

[129] S. J. Yang, *Low-Noise Electrical Motors*, New York: Oxford University Press, 1981, pp. 15–21.

[130] I. Daubechies, “Ten lectures on wavelets,” *Philadelphia: SIAM,* 1992.

[131] S.G.Mallat, “A theory for multiresolution signal decomposition: the wavelet representation,” *IEEE Transactions on Pattern Analysis and Machine Intelligence*, vol.11, pp.674–693, Jul. 1989.

[132] C. S. Burrus and J. E. Odegard, “Coiflet systems and zero moments,” *IEEE Trans. Signal Processing*, vol. 46, no. 3, pp. 761-766, Mar. 1998.

[133] D. Umehara, M. Morikura, T. Hisada, S. Ishiko, and S. Horihata, "Statistical impulse detection of in-vehicle power line noise using hidden Markov model," *in Proc. IEEE ISPLC 2010*, Mar. 2010, pp 1–6.

[134] S. Schulte, M. Nachtegael, V. D. Witte, D. V. der Weken, and E. E. Kerre, "A fuzzy impulse noise detection and reduction method," *IEEE Trans. Image Process.*, vol. 15, no. 5, pp. 1153–1162, May 2006.

[135] I. Pitas and A. N. Venetsanopoulos, *Nonlinear Digital Filters: Principles and Applications*, Kluwer Academic Publishers, 1990.

[136] R. Fadaeinedjad, G. Moschopoulos, and M. Moallem, "The impact of tower shadow, yaw error, and wind shears on power quality in a wind diesel system," *IEEE Trans. Energy Conversion*, vol. 24, no. 1, pp. 102–111, March 2009.

[137] J. S. Oakland, *Statistical Process Control*, 4th edition, Butterworth-Heinemann, 1999.

[138] J. M. Jonkman and M. L. Buhl, *FAST User's Guide*, National Renewable Energy Laboratory, Jul. 2005.

[139] R. Fadaeinedjad, M. Moallem, and G. Moschopoulos, "Simulation of a wind turbine with doubly fed induction generator by FAST and simulink," *IEEE Trans. Energy Convers.*, vol. 23, no. 2, pp. 690–700, Jun. 2008.

[140] Y. Zhang, Z. Chen, M. Cheng, and J. Zhang, "Mitigation of fatigue loads using individual pitch control of wind turbines based on FAST," in *Proc. 46th International Universities' Power Engineering Conference*, Sept. 2011, pp. 1-6.

[141] B. J. Jonkman, *TurbSim User's Guide.* National Renewable Energy Laboratory, 2009.

[142] IEC 61400-1 "Wind turbine generator systems-Part 1: Safety requirements." 2nd edition. Geneva, Switzerland: International Electrotechnical Commission, 1999.

[143] W. Gawronski, J. Mellstrom, and B. Bienkiewicz, “Antenna mean wind torques: A comparison of field and wind tunnel data,” *IEEE Antennas and Propagation Magazine*, vol. 47, no. 5, pp. 55–59, Oct. 2005.

[144] S. D. Kulkarni, M. A. Minor, M. W. Deaver, E. R. Pardyjak, and J. M. Hollerbach, “Design, sensing, and control of a scaled wind tunnel for atmospheric display,” *IEEE/ASME Transactions on Mechatronics*, vol. 17, no. 4, pp. 635–645, Aug. 2012.